A Study of W Boson Properties with Four-Jet W^+W^- events at LEP

Thesis by
Alexander Shvorob

In Partial Fulfillment of the Requirements
for the Degree of

Doctor of Philosophy

California Institute of Technology
Pasadena, California

2001

(Defended September 8, 2000)

Acknowledgments

First of all, I would like to express my gratitude for the support that my adviser, Harvey Newman, has given me throughout my stay at Caltech and CERN. My work would have been so much harder without his patient guidance and trust in me.

This thesis wouldn't be possible without help from many people in L3. It was indeed a pleasure to work with Alan Button, Chris Tully, Magda Pedace, Marat Gataullin, Sergey Shevchenko and many other talented and interesting people.

I owe special thanks to Martin Grünewald, who never turned down any questions of mine and was always there for me whenever I had a problem.

My interest in high energy physics was in large part due to the example that outstanding physicists like Vladimir Obraztsov and Giorgio Gratta set for me. I am indebted to them for my very enjoyable and engaging introduction to the field.

My sincerest thanks go to my friends, near and far away, who gave me the strength to persevere in my work. Daniël van Dierendonck did really a lot to keep my spirits up and make my life in Geneva fun. Kaia and Rego Ostonen never let me forget that there is life outside CERN and acquainted me with so many new, exciting things. Ildar Mukhametzhanov and Dima Pavlushko made me remember good old days and always kept me full of hope. Olga and Vasiliy Nomokonovy have been such a wonderful company and a great source of support when I needed it. I am grateful for all the help and advice I got from Wenwen Lu, Jayant Shukla and Alexander Zvyagin. Thanks also to Edik, Denis, Joana, Lisbet, Myfanwy, Sandra, Tony, Reg and Winston for all the great times I had with them. I am indeed lucky to have friends like these.

My parents and brother never left me to feel alone and lost. I am sorry I am so far away and don't see them nearly often enough.

Last but not least at all, my warmest thanks to Oksana, who made it all worthwhile.

Abstract

In this thesis I present a study of W pair production in e^+e^- annihilation using fully hadronic W^+W^- events. Data collected by the L3 detector at LEP in 1996–1998, at collision center-of-mass energies between 161 and 189 GeV, was used in my analysis.

Analysis of the total and differential W^+W^- cross sections with the resulting sample of 1,932 $W^+W^- \to q\bar{q}q\bar{q}$ event candidates allowed me to make precision measurements of a number of properties of the W boson. I combined my measurements with those using other W^+W^- final states to obtain stringent constraints on the W boson's couplings to fermions, other gauge bosons, and scalar Higgs field by measuring the total $e^+e^- \to W^+W^-$ cross section and its energy dependence

$$\sigma(e^+e^- \to W^+W^-) = \begin{cases} 2.68^{+0.98}_{-0.67}(stat.) \pm 0.14(syst.) \text{ pb}, & \sqrt{s} = 161.34 \text{ GeV} \\ 12.04^{+1.38}_{-1.29}(stat.) \pm 0.23(syst.) \text{ pb}, & \sqrt{s} = 172.13 \text{ GeV} \\ 16.45 \pm 0.67(stat.) \pm 0.26(syst.) \text{ pb}, & \sqrt{s} = 182.68 \text{ GeV} \\ 16.28 \pm 0.38(stat.) \pm 0.26(syst.) \text{ pb}, & \sqrt{s} = 188.64 \text{ GeV} \end{cases},$$

the fraction of W bosons decaying into hadrons

$$\text{BR}(W \to q\bar{q}') \;=\; 68.72 \pm 0.69(stat.) \pm 0.38(syst.)\ \%,$$

invisible non-SM width of the W boson

$$\Gamma_W^{invisible} \;<\; 17 \text{ MeV} \quad \text{at } 95\% \text{ C.L.},$$

the mass of the W boson

$$M_W = 80.44 \pm 0.08(stat.) \pm 0.06(syst.) \text{ GeV},$$

the total width of the W boson

$$\Gamma_W = 2.18 \pm 0.20(stat.) \pm 0.11(syst.) \text{ GeV},$$

the anomalous triple gauge boson couplings of the W

$$\begin{aligned} \Delta g_1^Z &= 0.16^{+0.13}_{-0.20}(stat.) \pm 0.11(syst.) \\ \Delta\kappa_\gamma &= 0.26^{+0.24}_{-0.33}(stat.) \pm 0.16(syst.) \\ \lambda_\gamma &= 0.18^{+0.13}_{-0.20}(stat.) \pm 0.11(syst.). \end{aligned}$$

No significant deviations from Standard Model predictions were found in any of the measurements.

Contents

List of Tables

List of Figures

Chapter 1

Introduction and Overview

In this thesis I present my study of the pair production of W bosons in the electron-positron annihilation process $e^+e^- \to W^+W^-$. The purpose of the measurements I performed is to determine important properties of the W boson, such as its mass, width, decay branching ratios, and couplings to the photon and the Z^0 boson. Abundant production of reconstructible W^+W^- events in a clean environment allows one to measure these quantities with a precision unattainable with other techniques. The measurements are compared with precise theoretical calculations to test the standard electroweak theory and search for possible deviations from it. In the absence of significant disagreements with SM predictions, the measurements can be used to constrain yet-unknown parameters of the Standard Model, such as the Higgs boson mass.

My analysis deals specifically with events in which both W bosons decay hadronically $W \to q\bar{q}'$, resulting in four-jet $W^+W^- \to q\bar{q}q\bar{q}$ events. Such events represent about 46% of the total W pair production cross section. Reconstruction of the differential $e^+e^- \to W^+W^-$ cross sections with these events allows the most precise measurement of a number of parameters of the W boson. I combine my measurements based on four-jet events with those using other types of W^+W^- events to arrive at the best experimental estimates, to be compared with theoretical predictions.

My analysis was based on the data collected by the L3 detector at LEP in 1996–1998 in runs with center-of-mass energies from 161 to 189 GeV. Approximately 2,000 multijet W^+W^- candidate events found in these data were used in my measurements.

Below I give a brief description of the following chapters of my thesis.

Chapter 2 discusses the status of the W boson in the Standard Model, the properties of the W production as predicted by the SM, and observable effects which could

be introduced by new electroweak theories being proposed to replace it.

Chapter 3 gives an overview of LEP and L3, the experimental facilities used to obtain the data I used, with an emphasis on characteristics especially important for my study.

Chapter 4 describes the methods I developed for discriminating $W^+W^- \to q\bar{q}q\bar{q}$ events from physics background processes and for measuring the $W^+W^- \to q\bar{q}q\bar{q}$ production cross section. The methods are applied to the L3 data sets to select events for analysis of the W mass and width and triple gauge boson couplings. The results of the cross section measurements are combined with those of semileptonic and leptonic W^+W^- events to measure the total W^+W^- cross section and W branching ratios. Comparison of those with the SM allowed me to put limits on Cabibbo-Kobayashi-Maskawa matrix elements and possible non-standard invisible W decays.

Chapter 5 is devoted to my measurements of the W mass, using the dependence of the total W^+W^- cross section on the W mass in the threshold region, as well as the reconstructed dijet invariant mass distributions. The latter are also used for a direct measurement of the W width. I combine my measurements with those obtained with semileptonic events to arrive at a more accurate estimate of the W mass, used to check the consistency of the Standard Model and infer the mass of the Higgs boson.

Chapter 6 describes reconstruction of angular distributions in $W^+W^- \to q\bar{q}q\bar{q}$ events which are used, together with the total W^+W^- cross section, to study triple gauge couplings involving W bosons. Limits on possible deviations of the $W^+W^-\gamma/Z^0$ couplings from their SM values are obtained.

Chapter 7 summarizes the results obtained in my study.

Chapter 2

Tests of Electroweak Physics with $e^+e^- \to W^+W^-$ Events

2.1 Physics of the W Boson before LEP 2

The first experiments whose understanding required the W boson were made, and the study of the weak interactions began, when spontaneous radioactivity of uranium was discovered by Henri Becquerel in 1896 [1]. It was soon realized that several quite different decay processes contributed to it [2] and the one which was accompanied by production of electrons was called the β-decay. Creation of the theory which explained this phenomenon, among many others discovered later, was one of the major achievements of physics in the twentieth century.

The neutrino [3] was postulated to explain apparent non-conservation of energy in β-decays, and the discovery of two different kinds of nucleons [4] laid the foundation for the theory of the weak interactions by Enrico Fermi [5]. The theory tried to describe β-decay in terms of point couplings of charged vector currents created by weak isospin doublets. Later the conjecture of parity violation by the weak interactions was put forward [6] and confirmed experimentally [7]. This led to replacement of the original vector currents with the currently accepted V–A structure [8].

Several attempts were made to improve on the contact interaction nature of the Fermi theory, which limits it to be a mere low-energy, non-renormalizable approximation. Introducing a vector boson mediating the interaction, in analogy with the photon in electromagnetism, would solve this problem. The analogy cannot be complete though, because a massless intermediate boson would be inconsistent with the

observed very short range of charged current weak interactions ($\sim 10^{-17}$ m). Eventually it was realized that short-range forces can be mediated by massive particles [9] and a heavy intermediate vector boson, denoted W, was proposed as a carrier of the weak charged current interaction by Oskar Klein in 1938 [10].

This chain of outstanding theoretical and experimental insights culminated in the development by A. Salam, S. Weinberg, and S. Glashow, among others, in the early 1970s of the modern electroweak theory [11], commonly referred to as the Standard Model. The underlying principle of the theory is the invariance of Nature with respect to local transformations of fermion fields, given by the SU(2) group in weak isospin space and the U(1) group in the hypercharge space (non-Abelian gauge theories were first considered by C.N. Yang and R.L. Mills [12]). To reproduce the low-energy phenomenology of the weak interactions, the symmetries have to be spontaneously broken by interactions with an additional scalar field whose ground state is not invariant under the gauge group transformations (the Higgs mechanism [13]). The structure and the mathematical apparatus of the theory are explained in great detail in the literature, e.g., see [14]. The theory was proven to be renormalizable [15] and subsequently was shown to possess great predictive power over a wide energy range. It explained all the data available at the time it was proposed, and has passed numerous new experimental checks since its inception [16], invariably with great success. Properties of the intermediate $W^{\pm}$ and Z^0 vector bosons, carriers of the weak interaction, were among most crucial predictions of the Salam-Weinberg theory.

The origin of the W boson in the Standard model is local SU(2) gauge symmetry in weak isospin space, postulated for doublets of left-handed fermions, listed in Table 2.1. Isospin raising and lowering operators, associated with SU(2) gauge fields, change the electric charge of the fermion they act on and therefore can be associated with particles of charge 1 and -1 respectively. The third SU(2) generator mixes with the generator of the U(1) hypercharge symmetry group upon breaking of the symmetries, giving the photon and the Z^0 boson.

The couplings of the W boson to fermions are determined by the fermionic kinetic

$T_3 = +1/2$	$\begin{pmatrix} \nu_e \\ e \end{pmatrix}_L$	$\begin{pmatrix} \nu_\mu \\ \mu \end{pmatrix}_L$	$\begin{pmatrix} \nu_\tau \\ \tau \end{pmatrix}_L$	$\begin{pmatrix} u \\ d \end{pmatrix}_L$	$\begin{pmatrix} c \\ s \end{pmatrix}_L$	$\begin{pmatrix} t \\ b \end{pmatrix}_L$
$T_3 = -1/2$						
$T_3 = 0$	e_R	μ_R	τ_R	u_R d_R	c_R s_R	t_R b_R

Table 2.1: Fermions in the Standard Model and their weak isospin eigenvalues. Left-handed fermions belong to SU(2) doublets, while right-handed ones are SU(2) singlets. Quark weak eigenstates are mixtures of quark mass eigenstates.

term of the SM Lagrangian, after introducing the covariant derivative

$$\mathcal{D}_\mu = \partial_\mu + ig_1 Y B_\mu + \frac{i}{2} g_2 \tau_j W^j_\mu, \tag{2.1}$$

where Y and B_μ are hypercharge and the corresponding gauge field, τ_j are SU(2) generators (commonly represented by Pauli matrices), g_1 and g_2 are U(1) and SU(2) couplings respectively, and the vector fields W^j are related to $W^\pm$ bosons as $W^\pm = \frac{1}{\sqrt{2}}(W^1 \mp iW^2)$. The gauge terms of the covariant derivatives are responsible for the terms in the Lagrangian

$$\mathcal{L}_{fermionic} = \sum_\psi \bar{\psi} i\gamma^\mu \mathcal{D}_\mu \psi = \ ... - \frac{g_2}{\sqrt{2}}(W^+_\mu J^\mu_+ + W^-_\mu J^\mu_-)... \tag{2.2}$$

which give rise to couplings of W boson fields to the charged currents

$$J^\mu_\pm = \sum_\psi \bar{\psi}\gamma^\mu \frac{1-\gamma_5}{2} \tau^\pm \psi. \tag{2.3}$$

Couplings to all left-handed fermions have the same strength $\frac{g_2}{\sqrt{2}}$.

Self-couplings of W bosons are also fully determined by the gauge structure of the covariant derivatives, through its effect on the W field strength tensors $W_{\mu\nu} = \frac{i}{g_2}[\mathcal{D}_\mu, \mathcal{D}_\nu]$ which enter the bosonic kinetic term

$$\mathcal{L}_{bosonic} = -\frac{1}{4} W^{\mu\nu}_i W^i_{\mu\nu}. \tag{2.4}$$

Quadratic terms in the field strength tensors introduce triple gauge γW^+W^- and $Z^0W^+W^-$ couplings, discussed in Chapter 6, as well as quadruple vertices $\gamma\ \gamma\ W^+W^-$, $\gamma\ Z^0\ W^+W^-$, $Z^0Z^0\ W^+W^-$, $W^+W^-\ W^+W^-$.

While the gauge symmetry idea allows one to predict many properties of the W boson, the picture is incomplete without the concept of spontaneous symmetry breaking. Mass terms for the W bosons (of the form $m^2W_\mu^+W_-^\mu$) are not gauge-invariant, still a (large) W mass is necessary to account for the very short range of weak charged current interactions. The Higgs mechanism provides a solution of this problem by postulating the existence of an additional (Lorentz) scalar field which is an SU(2) doublet (this is the minimal case; additional doublets and larger multiplets can be easily incorporated into an extended Higgs model; such a complication is not warranted by any experimental data yet). For some choices of the parameters μ^2, λ of the Higgs Lagrangian

$$\mathcal{L}_{Higgs} = (\mathcal{D}^\mu\Phi)^\dagger(\mathcal{D}_\mu\Phi) - \mu^2\Phi^\dagger\Phi - \lambda(\Phi^\dagger\Phi)^2 \tag{2.5}$$

the ground state of the scalar field has a non-trivial expectation value and is not SU(2)-invariant. Without loss of generality (after a gauge rotation) perturbations of such a ground state can be written as a doublet of the form

$$\Psi(x) = \frac{1}{\sqrt{2}}\begin{pmatrix} 0 \\ v + H(x) \end{pmatrix}, \tag{2.6}$$

where v is the vacuum expectation value, and $H(x)$ is the scalar field of the Higgs boson - a new particle predicted by this mechanism of electroweak symmetry breaking. After choosing a particular scalar field ground state the Higgs term becomes

$$\begin{aligned}\mathcal{L}_{Higgs} = {} & \frac{g_2^2}{4}W_-^\mu W_\mu^+(v+H)^2 + \frac{1}{8}(g_2W_3^\mu - g_1B^\mu)(g_2W_\mu^3 - g_1B_\mu)(v+H)^2 + \\ & \frac{1}{2}(\partial^\mu H)(\partial_\mu H) - \frac{\mu^2}{2}(v+H)^2 - \frac{\lambda}{4}(v+H)^4.\end{aligned} \tag{2.7}$$

The terms containing v^2 factors and gauge fields can be interpreted as mass terms for

two charged W bosons with mass

$$\mathrm{M_W} = \frac{1}{2} v g_2 \tag{2.8}$$

and a neutral Z^0 boson, given by the $Z_\mu = g_2 W_\mu^3 - g_1 B_\mu$ combination, with mass

$$\mathrm{M_Z} = \frac{1}{2} v \sqrt{g_1^2 + g_2^2}. \tag{2.9}$$

The orthogonal W_μ^3, B_μ combination $A_\mu = g_1 W_\mu^3 + g_2 B_\mu$ does not acquire a mass term and is associated with the photon. The other terms in the Higgs Lagrangian describe interactions of the Higgs and gauge fields (H $\mathrm{Z}^0\mathrm{Z}^0$, H $\mathrm{W}^+\mathrm{W}^-$, H H $\mathrm{Z}^0\mathrm{Z}^0$, and H H $\mathrm{W}^+\mathrm{W}^-$ vertices) and Higgs boson self-interactions.

The angle θ_W by which the (A_μ, Z_μ) and (W_μ^3, B_μ) bases are rotated, called the electroweak mixing angle, is completely determined (to leading order) by the strengths of the hypercharge U(1) and isospin SU(2) interactions:

$$\sin\theta_\mathrm{W} = \frac{g_1}{\sqrt{g_1^2 + g_2^2}}; \qquad \cos\theta_\mathrm{W} = \frac{g_2}{\sqrt{g_1^2 + g_2^2}}. \tag{2.10}$$

This single angle, in turn, determines the ratio of the vector boson masses

$$\frac{\mathrm{M_W}}{\mathrm{M_Z}} = \cos\theta_\mathrm{W}, \tag{2.11}$$

the ratio of electromagnetic fermion charges $e = \sqrt{4\pi\alpha_{em}}$ and weak charged current couplings

$$e = \frac{g_1 g_2}{\sqrt{g_1^2 + g_2^2}} = g_1 \cos\theta_\mathrm{W} = g_2 \sin\theta_\mathrm{W}, \tag{2.12}$$

and the structure of the neutral current couplings $\gamma\mathrm{f}\bar{\mathrm{f}}$ and $\mathrm{Z}^0\mathrm{f}\bar{\mathrm{f}}$.

By 1980, studies of deep inelastic neutrino scattering produced an accurate measurement of the mixing angle θ_W. Combined with the precise knowledge of α_{em}, this led to predictions for the intermediate vector boson masses [17].

These predictions were confirmed in 1983 by the discovery by the UA1 experiment at CERN's SPS collider of both the W [18] and Z^0 [19] bosons, with masses in agreement with the Standard Model.

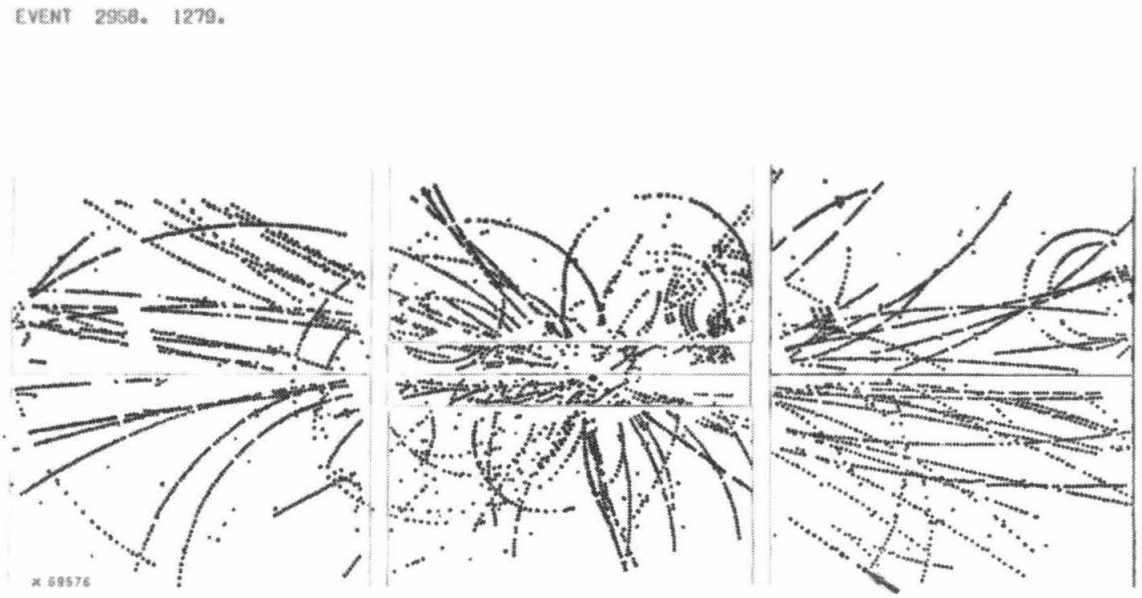

Figure 2.1: A $W \rightarrow e\nu$ event recorded by the UA1 detector. An energetic electron amidst hadronic background can be seen in the lower right quadrant. Five events of this type constituted the discovery of the W boson by the UA1 experiment.

Since the discovery of the W boson, precision studies of its properties were performed by the CDF and DØ experiments at the Tevatron collider at Fermilab [20]. Also information on the triple gauge boson couplings and limits on possible deviations from the SM were obtained by analysis of LEP 1 electroweak measurements [21]. Still LEP 2 measurements have been able to make an important contribution to and opened a new window on the physics of the W boson.

2.2 $e^+e^- \rightarrow W^+W^-$ Production in the Standard Model

Production of W pairs is possible in e^+e^- collisions at center-of-mass energies above $\sim 2M_W$. It proceeds through the four diagrams shown in Figure 2.2. The contribution

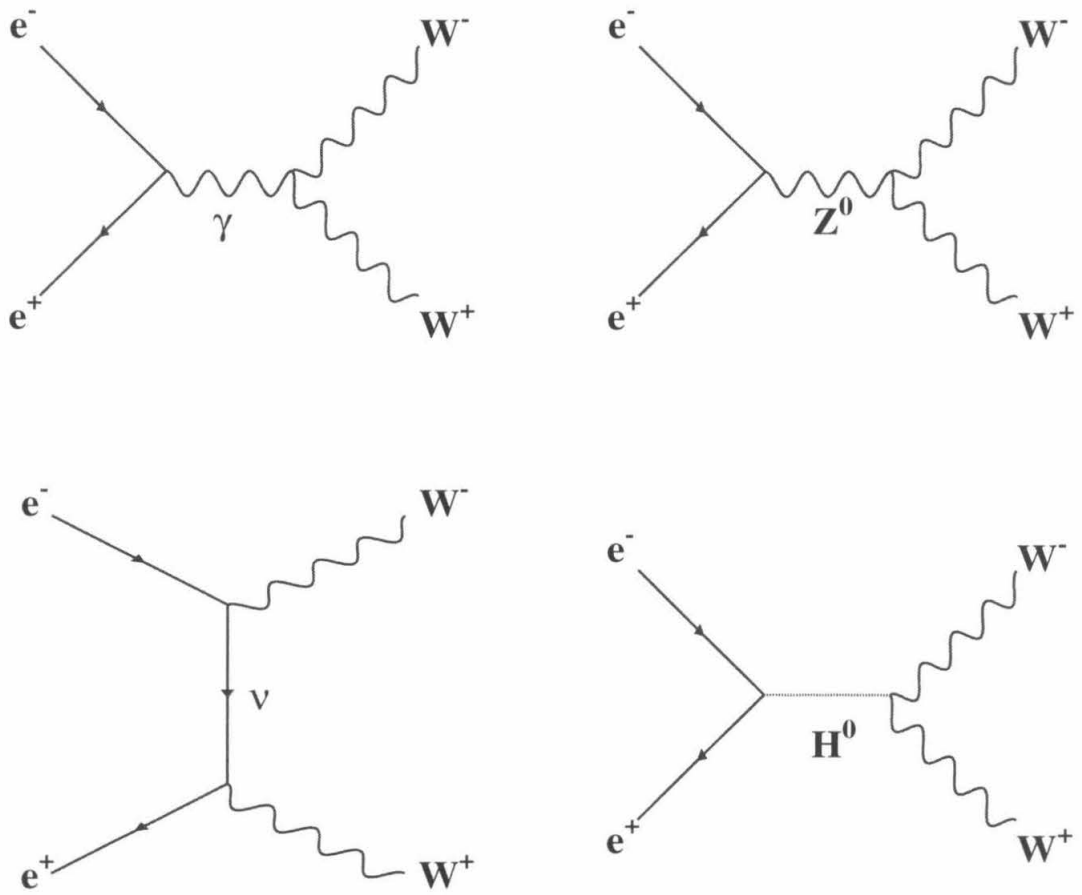

Figure 2.2: Lowest order $e^+e^- \rightarrow W^+W^-$ Feynman diagrams.

of the s-channel Higgs exchange diagram is very small because of the weakness of the He^+e^- coupling and is suppressed by a factor $M_e/\sqrt{s}$ relative to the other diagrams. This diagram is usually ignored in theoretical calculations. The remaining three diagrams are commonly referred to as the CC03 set.

The s-channel photon and Z^0 boson exchange diagrams involve γW^+W^- and

$Z^0W^+W^-$ vertices due to the non-Abelian nature of the SU(2) gauge group and are therefore especially interesting. Close to threshold the s-channel P-wave amplitudes are suppressed compared to the t-channel neutrino exchange, as shown in Figure 2.3. But already several GeV above the threshold, i.e., at the higher energy points data from which were used in my analysis, all diagrams' contributions as well as their interferences become important (see Figure 2.4). The complete formulae for the CC03 $e^+e^- \to W^+W^-$ matrix element and its helicity amplitudes composition can be found in [22].

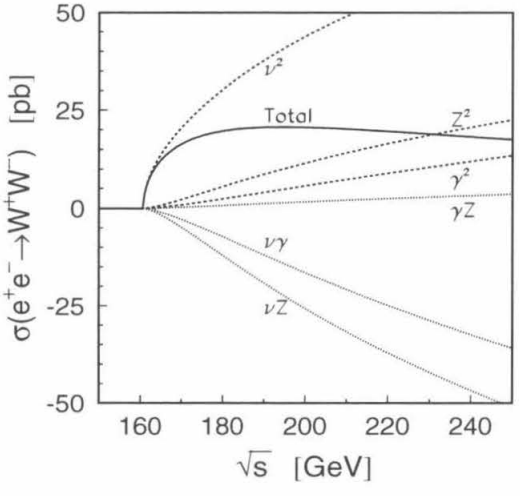

Figure 2.3: Total cross section of the reaction $e^+e^- \to W^+W^-$ and contributions of the CC03 diagrams as a function of $\sqrt{s}$.

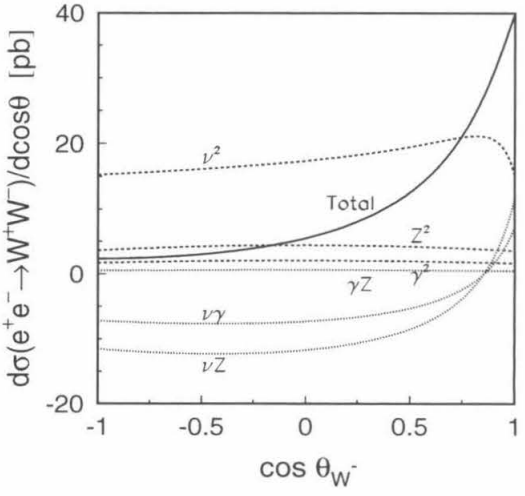

Figure 2.4: Polar angle distribution of the W^- boson and contributions of the CC03 diagrams for $e^+e^- \to W^+W^-$ production at $\sqrt{s} = 189$ GeV.

Once produced, the W bosons decay into all kinematically allowed SU(2) doublets with the partial width given by

$$\Gamma(W \to f\bar{f}') = \frac{G_F M_W^3}{6\pi\sqrt{2}} |V_{f\bar{f}'}|^2 R_M(M_W, m_f, m_{f'}) R_{QCD}, \qquad (2.13)$$

where the V matrix, relating mass and SU(2) eigenstates, is assumed to be diagonal for lepton families and is given by the Cabibbo-Kobayashi-Maskawa matrix for quark

doublets. The QCD correction factor is again trivial for leptons and takes into account color SU(3) degrees of freedom and QCD radiative corrections for quarks:

$$R_{QCD} = 3(1+\frac{\alpha_S(M_W^2)}{\pi}). \tag{2.14}$$

The kinematic factor accounting for non-zero fermion masses,

$$R_M(M_W, m_f, m_{f'}) = \sqrt{1-\frac{(m_f+m_{f'})^2}{M_W^2}}\sqrt{1-\frac{(m_f-m_{f'})^2}{M_W^2}} \times \left[1-\frac{m_f^2+m_{f'}^2}{2M_W^2}-\frac{(m_f^2-m_{f'}^2)^2}{2M_W^4}\right], \tag{2.15}$$

can be considered to be one with good accuracy (better than 0.5%) for all kinematically allowed fermion pairs.

Given the structure of the CKM matrix (see Table 2.2), the two dominant hadronic decay modes of the W are $W^+\to u\bar{d}$ and $W^+\to c\bar{s}$ (and their charge conjugates), each having branching ratio about three times that of $W\to \ell\nu$ for a given lepton family. The branching ratios of the W boson and the resulting composition of W^+W^- events are given in Table 2.3. The Standard Model predicts about 10% of W^+W^- events to be of the $\ell\nu\ell\nu$ type, with the rest shared roughly evenly between $q\bar{q}\ell\nu$ and $q\bar{q}q\bar{q}$ events.

$$\begin{pmatrix} 0.9742-0.9757 & 0.219-0.226 & 0.002-0.005 \\ 0.219-0.225 & 0.9734-0.9749 & 0.037-0.043 \\ 0.004-0.014 & 0.035-0.043 & 0.9990-0.9993 \end{pmatrix}$$

Table 2.2: 90% confidence limits on Cabibbo-Kobayashi-Maskawa matrix elements [23]. Columns in the table correspond to quark mass eigenstates d, s, and b, rows to respective weak isospin eigenstates. Unitarity of the matrix within the three quark generations is assumed.

The total width of the W boson in the SM,

$$\Gamma_W = \Gamma_{e\nu}+\Gamma_{\mu\nu}+\Gamma_{\tau\nu}+\sum_{q\neq t}\Gamma(W\to q\bar{q}') = \frac{3G_F M_W^3}{2\pi\sqrt{2}}(1+\frac{2\alpha_S(M_W^2)}{3\pi}), \tag{2.16}$$

W Decay	BR [%]
$W \rightarrow \ell\nu$	32.49
$W \rightarrow$ hadrons	67.51

W^+W^- Final State	Relative Frequency [%]
$\ell\nu\ell\nu$	10.56
$q\bar{q}\ell\nu$	43.86
$q\bar{q}q\bar{q}$	45.58

Table 2.3: The W boson decay and W^+W^- final state branching ratios predicted by the Standard Model.

amounts to 2.067 $\pm$ 0.021 GeV using the current knowledge of M_W and cannot be ignored in calculations of the $e^+e^- \rightarrow W^+W^-$ total and differential cross sections.

The finite W width leads to large corrections to the zero-width-approximation total W^+W^- cross section at all LEP 2 energies [24], as shown in Figure 2.5. The effect is particularly strong at the threshold, resulting in a much less sharp rise of the cross section with energy and the possibility of W^+W^- production below the $\sqrt{s} = 2M_W$ threshold. The finite W width also introduces a spread of the masses of the produced W bosons, which, ignoring phase space factors, is given by the Breit-Wigner density

$$\rho(m^2) = \frac{1}{\pi} \frac{M_W \Gamma_W}{(m^2 - M_W^2)^2 + M_W^2 \Gamma_W^2}. \quad (2.17)$$

This spread has important consequences for the precision of the W mass measurement described in Chapter 5.

Higher-order EW processes are another significant source of corrections to $e^+e^- \rightarrow W^+W^-$ cross section. Initial state radiation decreases the W^+W^- cross section by $\mathcal{O}(10\%)$ at LEP 2 energies [25]. It also leads to an $\mathcal{O}(1$ GeV) downward shift of the distribution of the produced W boson masses. This shift has to be corrected for in the measurement of the W mass. The Coulomb singularity [26, 27] is another QED process especially important at the threshold. It is due to the electromagnetic attraction between slowly moving charged W bosons. The correction is proportional to α_{em}/β_W and diverges at the threshold in the limit of zero W width. With finite Γ_W the correction amounts to about 5% right at the threshold and smaller values at

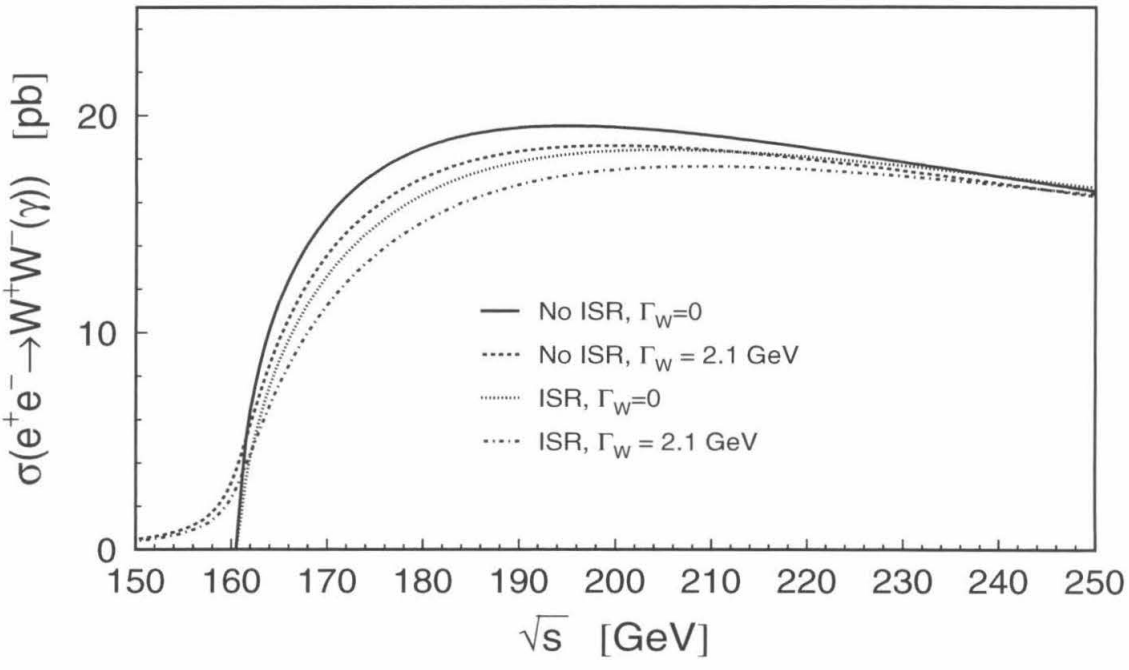

Figure 2.5: Total $e^+e^- \rightarrow W^+W^-$ cross section as a function of $\sqrt{s}$. Effects of finite W width and QED radiative corrections are shown.

higher energies. The total effect of QED radiative corrections on the $e^+e^- \rightarrow W^+W^-$ cross section is shown in Figure 2.5. QED corrections are explicitly taken into account in the analytical programs and Monte Carlo event generators I used in my analysis. The bulk of other electroweak radiative corrections is incorporated in the calculations by using energy-scale-dependent (running) values of EW parameters.

Considering W bosons as resonances with finite width, rather than zero-width (stable) particles, leads to another complication. To preserve gauge invariance of the $e^+e^- \rightarrow W^+W^- \rightarrow f_1\bar{f}_2f_3\bar{f}_4$ amplitude one has to consider all Feynman diagrams leading to the $f_1\bar{f}_2f_3\bar{f}_4$ final state, as opposed to the CC03 set. For W^+W^--like four-fermion final states, the number of contributing diagrams ranges from 9 to 56 depending on the final state, e.g., 11 for $u\bar{d}s\bar{c}$ and 43 for $u\bar{d}d\bar{u}$ four-quark final states, with both charged and neutral current graphs present as a general rule [28]. Figure 2.6 shows all the

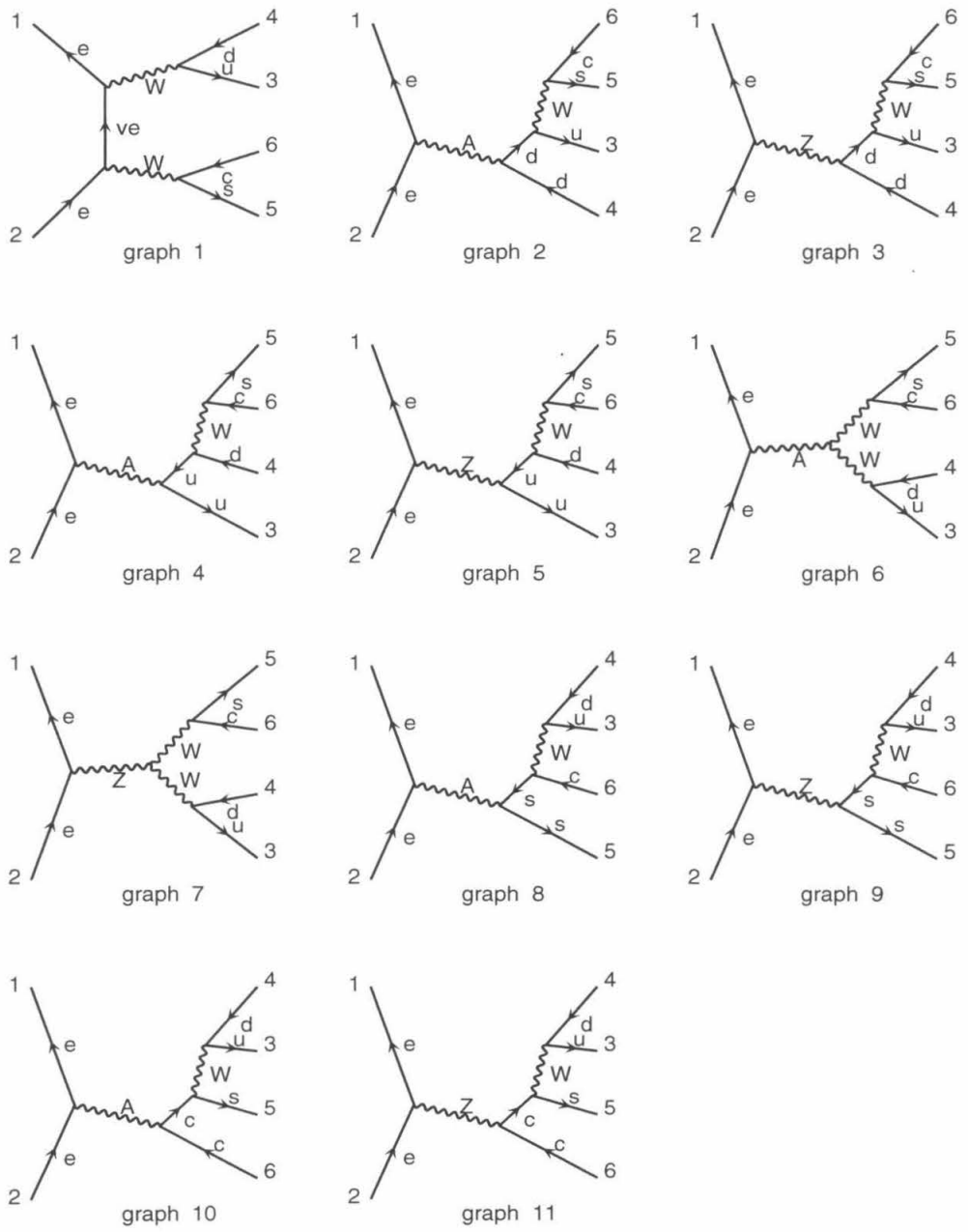

Figure 2.6: The complete set of $e^+e^- \to u\bar{d}s\bar{c}$ Feynman diagrams. Graphs 1, 6, and 7 are CC03 double-resonant diagrams. The rest of the diagrams contain one W boson each and are single-resonant.

diagrams contributing to $e^+e^- \to u\bar{d}s\bar{c}$. Fortunately, in the commonly used gauges the single-resonant and non-resonant graphs are suppressed relative to double-resonant CC03 ones by powers of $\Gamma_W/M_W \approx 2.5 \times 10^{-2}$. They are ignored in the Monte Carlo programs I use and I have to evaluate the effect of their neglect on my measurements.

After taking into account all the corrections mentioned above, SM calculations predict values of the $e^+e^- \to W^+W^-$ cross section of approximately 3 pb at the threshold, rising fast to ~16 pb at $\sqrt{s} = 189$ GeV (see Figure 2.5).

By and large, the precision of the available theoretical calculations is adequate for the measurements I am interested in. The current understanding of the W^+W^- cross section is accurate to 2% at the threshold and about 1% at higher energies, while the average ISR energy loss, bearing on the W mass measurement, is known to about 15 MeV [29]. Those uncertainties are small compared to actual experimental errors.

2.3 $e^+e^- \to W^+W^-$ Production as a Probe of Electroweak Physics

The sizeable cross section and good theoretical understanding of the reaction $e^+e^- \to W^+W^-$ makes it a promising tool for precision studies of the physics of the W boson.

It was recognized already in 1961 that "electron-positron collisions would in fact constitute a good experimental means for [intermediate charged vector mesons'] detection." [30] The first naive methods of measuring the mass and electromagnetic properties of the W with $e^+e^- \to W^+W^-$ events were proposed as early as in 1965 [31].

Experimentally, e^+e^- colliders offers significant advantages over pioneering $p\bar{p}$ machines. As the backgrounds for $e^+e^- \to W^+W^-$ event selections are mostly due to other electroweak processes, they do not dominate and this allows one to study all decay modes of the W. An e^+e^- collision has a well-defined initial state which enables one to reconstruct the full event kinematics, in contrast to hadron colliders, where only transverse momenta can be used for measurements. Also the importance of triple gauge boson vertices in W pair production makes their study easier in e^+e^-

collisions.

Soon after the Standard Model was developed, $e^+e^- \rightarrow W^+W^-$ annihilation was proposed as a means to test the SM and contrast it with other electroweak models [32], and to measure its triple gauge boson couplings [33]. The reaction is particularly interesting because an intricate interplay (gauge cancellations) between all four diagrams in Figure 2.2 is required to make the total $e^+e^- \rightarrow W^+W^-$ cross section and its partial waves preserve unitarity at high energies (see, for example [14]). It was found [34] that the requirement of "good" high-energy behavior of $e^+e^- \rightarrow W^+W^-$ amplitudes limits the structure of a prospective electroweak theory to the spontaneously broken Yangs-Mills gauge one of the Standard Model, and also puts severe constraints on the mechanism of the symmetry breaking. Thus also from the theoretical point of view, $e^+e^- \rightarrow W^+W^-$ production is a sensitive probe of the gauge structure of the SM and its possible extensions.

2.3.1 Constraints on Higgs Boson Mass

The mass of the Higgs boson M_H is not predicted by the Standard Model and is an object of enormous interest. Finding the Higgs boson and determining its mass are some of the main goals of current experimental programs at LEP and FNAL and of the LHC project.

M_H-dependent radiative corrections to well-measured processes involving the W boson provide a means of estimating M_H, using the available precision electroweak measurements.

The width of the muon decay $\mu^- \rightarrow e^- \bar{\nu}_e \nu_\mu$ (see Figure 2.7) can be measured very accurately and allows a very precise determination of the Fermi constant G_F [35] which is the strength of weak charged current interactions at zero momentum transfer. This coupling is given by

$$G_F = \frac{g_2^2}{4\sqrt{2}M_W^2} = \frac{\pi \alpha_{em}}{\sqrt{2}M_W^2 \sin^2\theta_W}. \quad (2.18)$$

After expressing $\sin\theta_W$ in terms of M_W and the well-measured M_Z the relation be-

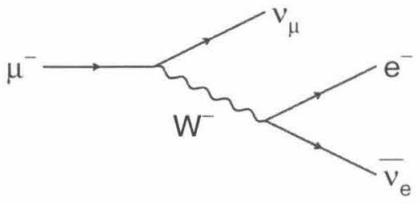

Figure 2.7: The diagram of the muon decay $\mu^- \rightarrow e^- \bar{\nu}_e \nu_\mu$.

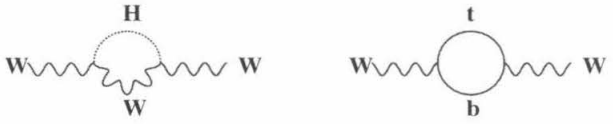

Figure 2.8: Radiative corrections to the W boson propagator involving the top quark and the Higgs boson.

comes

$$M_W^2\left(1 - \frac{M_W^2}{M_Z^2}\right) = \frac{\pi \alpha_{em}}{\sqrt{2} G_F}. \tag{2.19}$$

Radiative corrections modify the above tree-level expression. The QED part of the corrections is taken into account by using the running value of electromagnetic coupling α_{em} at M_Z instead of the one at low energies, which is very precisely measured. Electroweak corrections due to loop insertions in the W boson propagators, shown in Figure 2.8, are taken into account explicitly,

$$M_W^2\left(1 - \frac{M_W^2}{M_Z^2}\right) = \frac{\pi \alpha_{em}(M_Z^2)}{\sqrt{2} G_F (1 - \Delta r_w)}. \tag{2.20}$$

The weak radiative correction [36] is dominated by the term which depends on the top quark mass M_t, but has a non-negligible M_H dependence as well,

$$\begin{aligned} \Delta r_w = -\tfrac{G_F M_W^2}{8\sqrt{2}\pi^2} \Big[& 3\cot^2\theta_W \frac{M_t^2}{M_W^2} + 2(\cot^2\theta_W - \frac{1}{3}) \ln \frac{M_t^2}{M_W^2} - \\ & \frac{11}{3} \ln \frac{M_H^2}{M_W^2} + \\ & \frac{4}{3} \ln \cos^2\theta_W + \cot^2\theta_W + \frac{41}{18} \Big]. \end{aligned} \tag{2.21}$$

Thus, given measurements of G_F and vector boson and top quark masses and a

calculation of α_{em} (M_Z^2), the G_F definition (2.20) can be interpreted to give an estimate of M_H. The results of this analysis, done with the currently measured value of M_W, are reported in Chapter 7.

2.3.2 Constraints on Extensions of the Standard Model

Various new theories proposed to replace the SM predict properties of the W boson and W^+W^- production that differ from those expected in the Standard Model. $e^+e^- \rightarrow W^+W^-$ production can be used to put them to an experimental test.

Supersymmetry is currently the leading "new physics" candidate. It predicts a large number of new particles, which introduce additional large radiative corrections to electroweak processes. Equation (2.20), reinterpreted as a calculation of the W mass, predicts directly measurable $\mathcal{O}(100$ MeV) shifts of M_W in the Minimal Supersymmetric Standard Model [37], depending on the internal parameters of the model. Supersymmetric SM extensions also predict difficult to observe $\mathcal{O}(10^{-2})$ anomalous triple gauge boson couplings [38].

New particles predicted by technicolor models or obtained by adding more generations to the three currently included in the Standard Model, also enter W observables through loops in W propagators, and lead to similar deviations [39].

Other more exotic theories predict deviations from the SM in $e^+e^- \rightarrow W^+W^-$ already at the tree level. For example, expanding the gauge groups of the SM can lead to additional neutral intermediate vector bosons. The existence of such a boson would modify, by its mixing with Z^0, the $e^+e^- \rightarrow Z^0 \rightarrow W^+W^-$ process with large, model-parameter-dependent effects on the W^+W^- total and differential cross sections [40].

Another extension of the SM attempts to solve the hierarchy problem [41] (naturalness of gravitational radiative corrections to the Higgs boson mass) by postulating the existence of a few additional dimensions and an electroweak-gravitation "unification scale" M_S of the order of a few hundred GeV [42]. Being compact with sizes of the order of 1 mm, these extra dimensions do not affect macroscopic Newton's law, yet the low effective gravity scale M_S makes graviton exchange between Standard

Model particles non-negligible. The $e^+e^- \rightarrow W^+W^-$ cross section receives large, up to a few %, corrections from additional graviton diagrams and can be used to put bounds on parameters of such models [43].

In addition, in some models, including supersymmetric ones, non-standard W decays are allowed. Such models may possess regions of the parameter space which do not predict observable effects in lower energy data but significantly affect the W branching ratios, width, or visible $e^+e^- \rightarrow W^+W^-$ cross sections, if the non-standard W decays make the W^+W^- events escape detection [44, 45].

Chapter 3

The L3 Detector at LEP 2

My analysis was based on data collected by the L3 detector at the LEP accelerator. This chapter gives an overview of these experimental facilities, with an emphasis on the elements important for the measurements described in this thesis.

3.1 The LEP Accelerator

The Large Electron–Positron storage ring (LEP) is an accelerator operated by the European Laboratory for Particle Physics (CERN) located near Geneva, Switzerland (see Figure 3.1). It is designed to accelerate and collide electron and positron beams with energies up to approximately 100 GeV and is currently the world's most powerful e^+e^- collider.

The electron and positron beams are provided by the LEP injector chain [46], shown in Figure 3.2, using the previously built Proton Synchrotron (PS) and Super Proton Synchrotron (SPS) accelerators. Positrons are created in a tungsten converter target hit by a 200 MeV e^- beam from LIL (LEP Injecteur Linéare), a high-intensity linac. A second linac accelerates the electrons and positrons up to 600 MeV to be accumulated and cooled in the Electron–Positron Accumulation Ring (EPA). PS and SPS subsequently accelerate the beams up to 3.5 GeV and 20 GeV respectively, after which they can be injected into LEP [47].

The LEP tunnel, 27.6 km long, consists of eight straight and eight curved sections. The latter house about 3,300 dipole bending magnets which keep the beams in orbit, and about 800 quadrupole and 500 sextupole magnets used for beam focusing. The energy needed to accelerate the beams and compensate for synchrotron

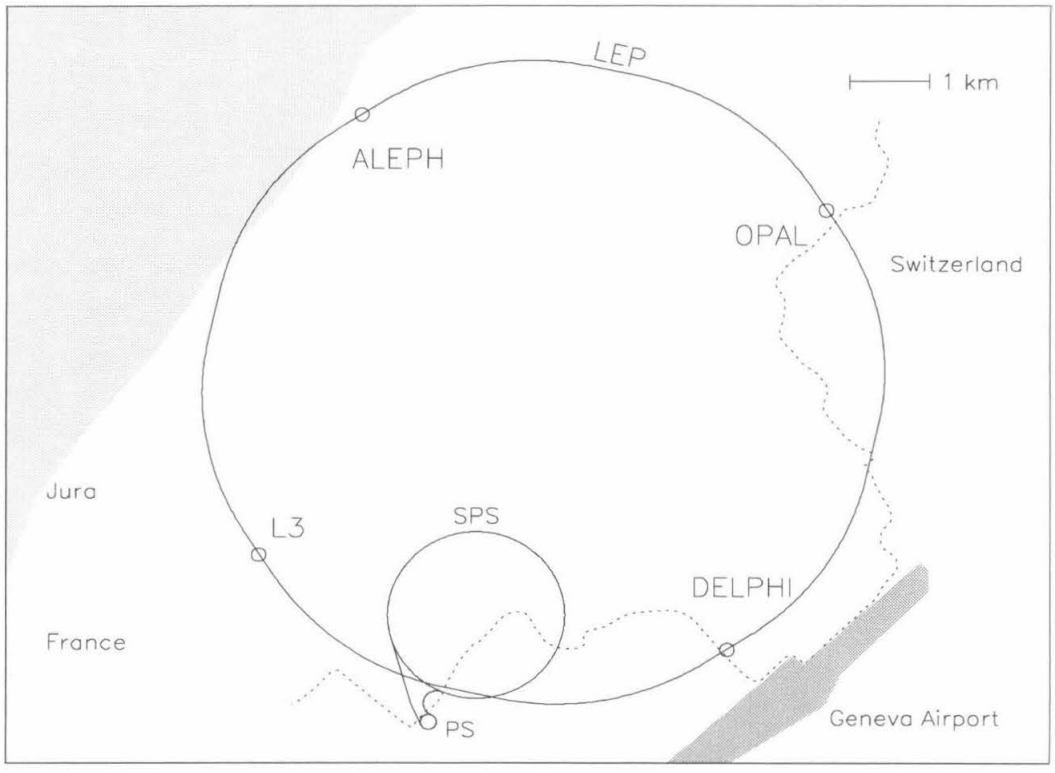

Figure 3.1: Schematic map of the region near Geneva, showing the location of LEP, the Proton Synchrotron (PS) and Super Proton Synchrotron (SPS) together with the four LEP experiments (ALEPH, DELPHI, L3, and OPAL).

radiation losses is provided by 288 superconducting radiofrequency cavities placed in the straight sections. Electron and positron beams, each composed of 4 equidistant bunches, revolve in opposite directions around the ring with a frequency of 11.4 kHz and are collimated and brought into collision at four equidistant interaction points equipped with detectors (ALEPH, DELPHI, L3, and OPAL). The interaction point size, determined by the bunch size, is about 1 cm along the beam direction, and 200 nm and 20 nm in the horizontal and vertical directions respectively in the plane orthogonal to the beam axis.

The construction of the LEP tunnel was started in 1983 and the first electron–positron collisions were recorded in August 1989. During Phase 1 (until 1995) LEP

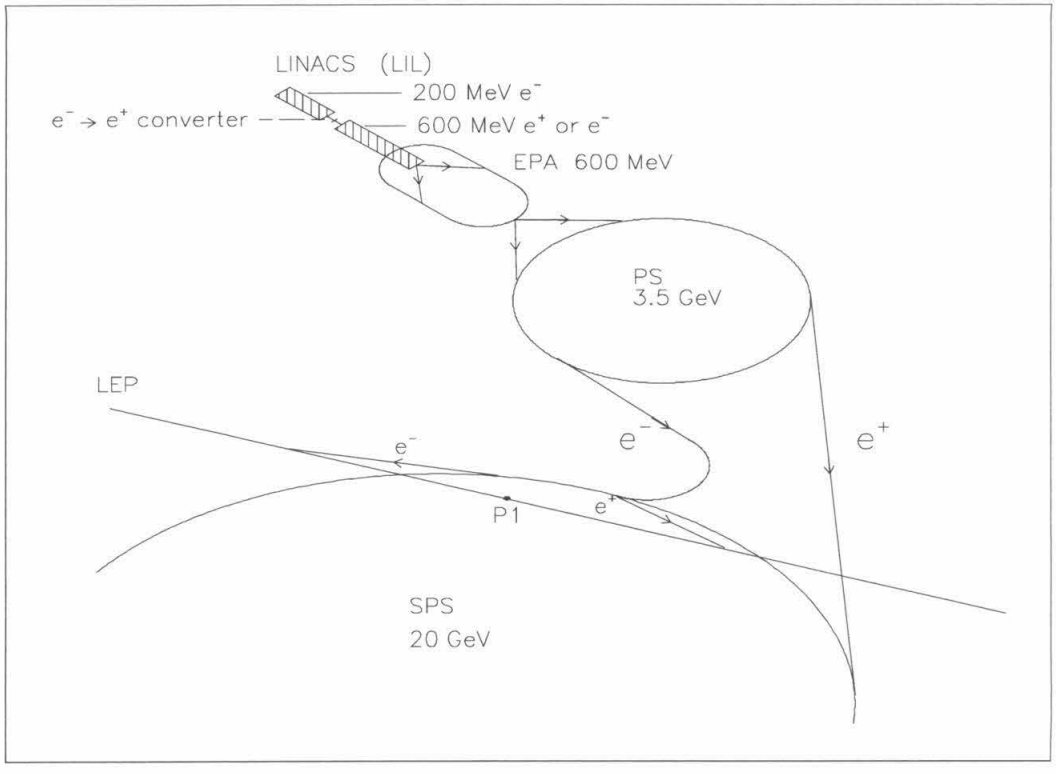

Figure 3.2: The LEP injector chain.

was operated with ~45 GeV beams, corresponding to center-of-mass energies close to the Z^0 boson mass. This allowed each of the four experiments to collect about 4 million $e^+e^- \rightarrow Z^0$ events and make unrivaled precision measurements of the Z^0 boson properties [48].

Phase 2 started in 1995 with superconducting RF cavities replacing the originally installed copper ones, increasing the maximal LEP beam energy from 45 to 70 GeV, and then to 86 GeV and higher in later years. This brought the collision center-of-mass energy above the W^+W^- pair production threshold and allowed precision studies of the W boson. It also greatly extended the scope of searches of new particles predicted by various extensions of the Standard Model.

LEP 2 also accomplished a large increase in the luminosity delivered to the experiments, due to the lesser importance of beam-beam interactions which limited the beam current at LEP 1. Additionally, for parts of the 1996 data-taking LEP was

operated in the bunch train mode, replacing each lepton bunch by two bunchlets separated by ~250 ns, and thus achieving a higher total beam current. A peak luminosity of 1.2×10^{32} $s^{-1}cm^{-2}$ was achieved in 1998. This, together with increasing overall operational efficiency, allowed each experiment to collect up to 2 pb^{-1} of data per day.

3.2 LEP Beam Energy Measurement

Precise knowledge of the LEP beam energy is crucial for some of the most important measurements at LEP, e.g. those of the mass and width of Z^0 and the mass of the W boson.

At LEP 1, the resonant depolarization method [49] gave an opportunity to measure the beam energy with very high precision. The method exploits the Sokolov-Ternov self-polarization of an electron beam due to emission of synchrotron radiation [50]. This transverse polarization can be destroyed by exciting the beam with an oscillating transverse magnetic field of a frequency that matches the electron spin precession frequency. Thus the ratio of the well-measured LEP orbital and resonant depolarization frequencies gives an estimate of the beam energy with a precision of about 200 keV. The beam energy is interpolated between the calibration polarization runs using measurements from NMR probes inserted in 16 of the dipole magnets. Elaborate methods were developed for this interpolation, accounting for a wide variety of external influences, achieving an energy measurement precision of 5 MeV [51].

The calibration became a much more difficult task at LEP 2, as significant transverse polarization cannot be achieved at energies above around 60 GeV due to depolarizing resonance driven by magnetic field imperfections. Therefore, to get a precise beam energy estimate, NMR measurements at LEP 2 center-of-mass energies have to be extrapolated over a wide energy interval down to resonant depolarization measurements in the 41–55 GeV range. The uncertainty of this extrapolation turns out to be the limiting factor of the beam energy measurement at LEP 2. It was evaluated using complementary flux loop probes, with which all LEP dipole magnets are equipped,

and was found to be in the 20–30 MeV range for the data used in my analysis, as shown in Table 3.1.

Data period	ΔE_b [MeV]	σ_{E_b} [MeV]
96A (July – August 1996)	27	144±7
96B (October – November 1996)	30	165±8
97 (July – November 1997)	25	219±11
98 (May – November 1998)	20	237±12

Table 3.1: Beam energy uncertainty and spread measurements measured for the LEP running periods used in the analysis [52].

A new method to measure the LEP beam energy was employed in 1999. The LEP spectrometer [53] is a system of beam orbit monitors designed to determine the beam energy by measuring the deflection of the beam by a LEP lattice bending dipole. Precision of about 10 MeV is expected to be ultimately achieved with this technique.

3.3 The L3 Detector

The L3 detector [54] is designed to study high energy e^+e^- collisions up to center-of-mass energies $\sim$ 200 GeV with emphasis on reliable identification and precise measurement of energy of electrons, photons, and muons. Figure 3.3 shows a perspective view of the detector. L3 subdetectors are arranged in layers of increasing size surrounding the interaction point. The tracking system and calorimeters are contained in a steel tube (see Figure 3.4), which supports also the muon chambers and maintains the alignment of the detector. Starting from the interaction point radially outwards, the main detector components are:

- the tracking system measuring directions and momenta of charged particles
- the Electromagnetic CALorimeter (ECAL), whose purpose is to measure energies and directions of electrons and photons
- the Hadron CALorimeter (HCAL), measuring the energies and directions of

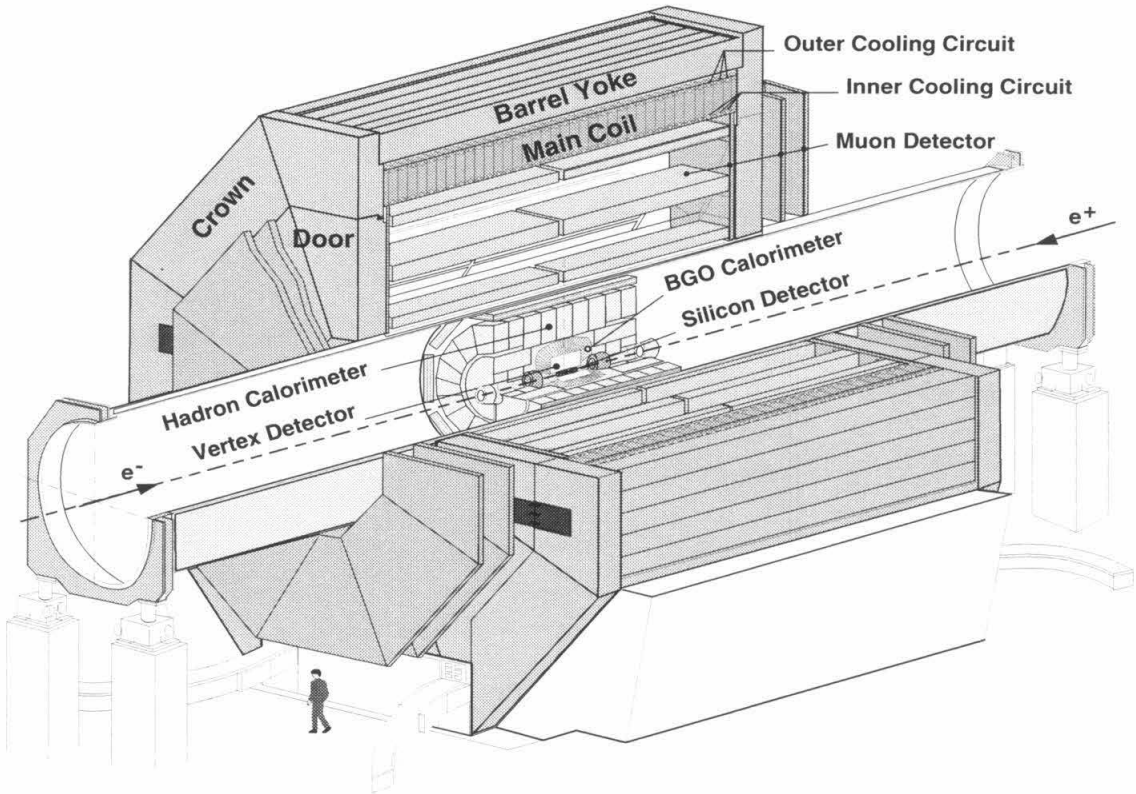

Figure 3.3: A perspective view of the L3 detector.

hadrons

- MUon CHambers (MUCH), measuring the directions and momenta of muons

In addition, luminosity monitors used to detect electrons from small-angle $e^+e^- \rightarrow e^+e^-$ Bhabha scattering, are installed close to the beam pipe at both sides at a distance of 2.8 meters from the interaction point.

The entire detector is surrounded by a solenoidal magnet providing a magnetic field of 0.5 T along the beam axis. Coils wrapped around magnet doors create a toroidal magnetic field of 1.5 T which is used to measure momenta of forward muons.

In the following sections the subdetectors used in the present analysis are described in greater detail.

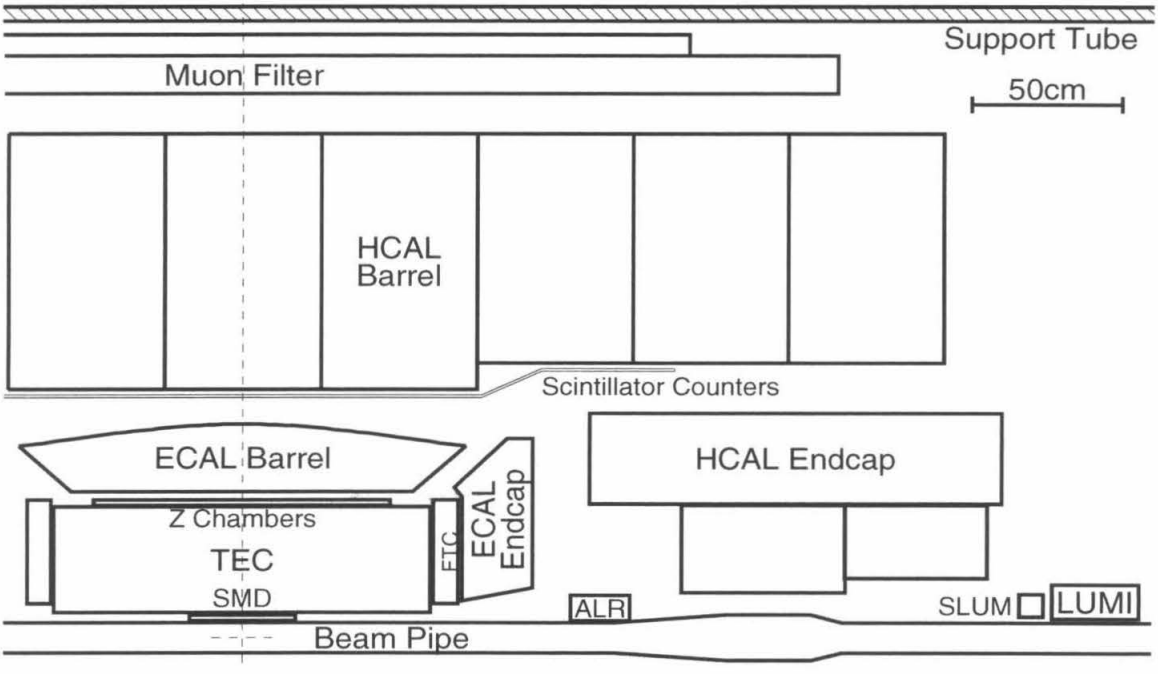

Figure 3.4: A side view of the inner L3 detector. In addition to the main detector components also shown are Active Lead Ring (ALR), and silicon (SLUM) and calorimeter (LUMI) components of the luminosity monitor.

3.3.1 L3 Tracking System

The aim of the L3 tracking system, shown in Figure 3.5, is to reconstruct charged particle trajectories in the central region of L3, to measure particle charge and momentum, and to reconstruct secondary vertices from decays of particles in flight. Its principal components are the Silicon Microvertex Detector (SMD), Time Expansion Chamber (TEC), Forward Tracking Chambers (FTC), and z-chambers.

The SMD [55] consists of two layers of double-sided silicon ladders 35.5 cm long, located at distances of 6 cm and 8 cm from the z-axis and covering the polar angles $22° - 158°$. The outer silicon surface of each ladder is read out using strips with a 50 μm pitch for the $r\phi$ coordinate measurements; the inner surface is read out with a 150 μm pitch (central region) or 200 μm pitch (forward regions) for the z coordinate measurements. The single track resolution of the SMD is 6 μm in $r\phi$ and 20–25 μm in z.

The TEC is a drift chamber with inner radius 8.5 cm, outer radius 47 cm, and

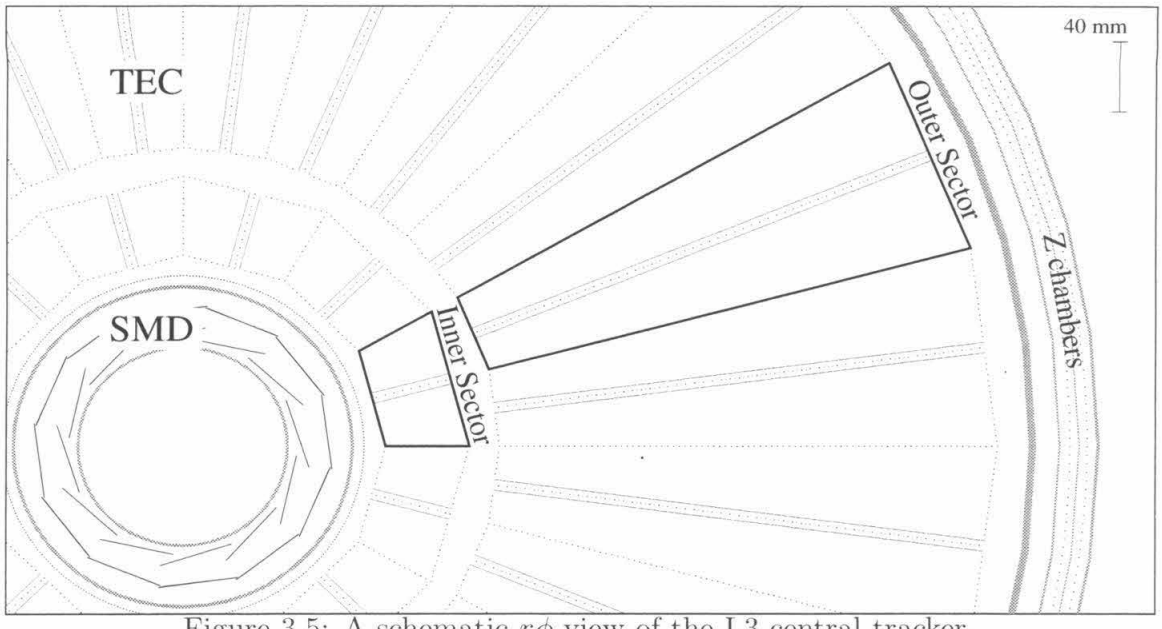

Figure 3.5: A schematic $r\phi$ view of the L3 central tracker.

length 98 cm. Radial cathode wire planes divide the TEC into 12 inner and 24 outer sectors, which are in turn subdivided radially by a plane of mixed anode sense wires and additional cathode wires. Planes of closely spaced grid wires on either side of each anode plane provide a homogeneous low electric field in most of the sector (drift region), with a small high-field region near the anode plane (amplification region). The timing of the ionization signal measured at each anode determines the distance to the track along a line perpendicular to the anode plane with an average resolution of ~ 50 μm.

The z coordinate of a track at fixed distance from the beam axis is measured by two layers of drift chambers surrounding the cylindrical outer surface of TEC and covering the polar angles $45° < \theta < 135°$. The z-chambers provide single track resolution of ~ 300 μm.

Two layers of FTC cover the end of TEC and measure the x-y coordinates of a track at fixed z. These proportional chambers cover the polar angles $9.5° < \theta$ $(180° - \theta) < 37.5°$ and have a spatial resolution of ~ 150 μm.

3.3.2 Electromagnetic Calorimeter

Most of the electromagnetic calorimeter is made of bismuth germanium oxide $Bi_4Ge_3O_{12}$ (BGO) crystals. BGO was chosen to be used as both the showering and detecting medium for electrons and photons because of its very short radiation length and Molière radius and high scintillation light yield.

The BGO calorimeter consists of two symmetrical half barrels (7680 crystals in total) surrounding the central tracking system with polar angle coverage $42° < \theta < 138°$, and two endcaps (1527 crystals each) located behind the FTC with polar angle coverage $10° < \theta\ (180° - \theta) < 37°$.

The crystals are 24 cm long truncated pyramids about 2×2 cm^2 at the inner and 3×3 cm^2 at the outer end, aligned with their axis pointing to the area around the interaction point. Two silicon photodiodes are glued to the rear end of each crystal to detect the BGO scintillation light.

For electrons and photons the energy resolution of the calorimeter is parametrised as [56] $\frac{\sigma_E}{E} = \sqrt{\left(\frac{a}{\sqrt{E}} + b\right)^2 + d^2 + \left(\frac{c}{E}\right)^2}$, where $a = 1.54 \cdot 10^{-2}$ GeV$^{1/2}$, $b = 0.38 \cdot 10^{-2}$, $c = 0.25 \cdot 10^{-2}$ GeV and $d = 0.9 \cdot 10^{-2}$. For electrons and photons of more than 5 GeV energy resolution better than 2% and angular resolution better than 2 mrad are achieved.

The angular interval between the barrel and endcap parts of the BGO calorimeter is covered by ECAL GAP filler (EGAP), a lead-scintillator sampling calorimeter which has a worse resolution. The Active Lead Ring (ALR) is a similar calorimeter covering the forward angular regions between the coverage of BGO endcaps and the luminosity monitor $4.5° < \theta\ (180° - \theta) < 8.8°$.

A more detailed description of the electromagnetic calorimeter can be found in [57].

3.3.3 Scintillation Counters

A layer of plastic scintillation counters located between the electromagnetic and hadron calorimeters provides time-of-flight measurement of traversing charged particles, with a better than 1 ns resolution. This information is used to reject cosmic

muons piercing the detector (and leaving a pair of scintillator hits separated in time), to identify beam bunchlets when LEP runs in the bunch train mode, and also to provide an independent trigger for events originating from e^+e^- collisions.

3.3.4 Hadron Calorimeter

Most hadrons pass through ECAL which has a thickness of about 0.95 nuclear interaction lengths. The hadron calorimeter [58] is designed to absorb and measure the energy of the hadrons.

Layers of depleted uranium with total thickness of 4–7 nuclear interaction lengths, interspersed with 10 proportional wire chambers, serve as the absorber material and shower detectors respectively. The wires in successive layers of the wire chambers are rotated relative to each other, thus providing 2D shower coordinate measurement. The wires are readout in cells (towers) each covering $\sim 2.5^\circ \times 2.5^\circ$ solid angle in the barrel region.

The HCAL barrel is divided into 16 modules in ϕ and 9 modules in z, with angular coverage $35^\circ < \theta < 145^\circ$. The HCAL endcaps consist of three rings: an outer ring and two inner rings, covering the polar angle regions $5.5^\circ < \theta\ (180^\circ - \theta) < 35^\circ$.

The barrel HCAL is surrounded by the muon filter, a system of brass plates interleaved with layers of proportional chambers, adding about 1 nuclear interaction length to the HCAL. Its aim is to absorb the tails of HCAL showers and prevent them from reaching the muon chambers.

3.3.5 Muon Chambers

The barrel muon chambers consist of eight octants, each containing three layers of "P"-chambers, measuring the $r\phi$ coordinates, and two "Z"-chambers, measuring the z coordinate on the muon track. The barrel muon chambers cover the angular range $43^\circ < \theta < 137^\circ$. Three additional layers of drift chambers are mounted on the magnet doors on each side of the interaction point, extending the angular coverage to $22^\circ < \theta < 158^\circ$.

The momentum resolution $\sigma(p_T)/p_T$ for muons varies from approximately 2% in the barrel to approximately 30% in the endcaps.

3.3.6 L3 Luminosity Measurement

The luminosity measurement at L3 is based on small-angle Bhabha scattering, whose cross section is very large at low polar angles and can be calculated with small theoretical uncertainty. The luminosity is derived from the calculated cross section and the number of e^+e^- events counted by the luminosity monitor [59].

The luminosity detector consists of a BGO calorimeter (LUMI) at both sides of the interaction point with polar angle coverage 31–62 mrad, and a silicon tracker (SLUM) in front of LUMI, providing better position measurement for electrons and positrons entering the calorimeter. Bhabha events for the luminosity measurement are selected as back-to-back energy deposits in LUMI.

The precision of the luminosity measurement by L3 is dominated by systematic uncertainties for all data sets I used and is about 0.2%.

3.3.7 Trigger and Data Acquisition

After each beam crossing the trigger system decides whether an e^+e^- interaction took place, in which case the detector signals are read out, digitized and written to tape (the event is triggered).

Triggering is done in three levels of increasing complexity. The level 1 trigger consists of five independent triggers using signals from calorimeters, TEC, luminosity monitor, muon chambers, and scintillation counters, and either initiates digitisation, or clears the front end electronics before the next beam crossing. After a positive decision the detector data are stored within 500 μs in multievent buffers, and during that time all further data taking is stopped (dead time). Negative decisions do not induce dead time, as the electronics are cleared before the next beam crossing. The level 2 trigger combines the fast digitized trigger data from all subdetectors for events which were not automatically accepted by coincidence of at least two level 1 triggers.

The level 3 trigger uses already fully digitized signals from all subdetectors to refine the decision of the level 2 trigger.

The level 1 trigger rate varies between 5–20 Hz, and the final event rate written on tape is about 1–5 Hz.

3.3.8 Event Generation and Detector Simulation

The complexity of the detector makes it impossible to predict analytically the detector response to any particular physics process. Monte Carlo simulations provide a way to predict the properties of the events reconstructed by the detector.

Generation of events usually proceeds via two steps. First events, i.e., lists of particle types and energy-momentum four-vectors, are created with a Monte Carlo generator corresponding to a given interaction process or physical model. Then the generated particles are propagated through a detailed representation of the detector using the GEANT 3 [60] detector description and simulation tool, which simulates energy loss, scattering and showering of the particles in the detector material, as well as the response of each active detector element. Detector imperfections (inactive or noisy BGO crystals, disconnected TEC sectors, etc.) are included in the simulation using detector status databases created during data taking. In the end, the simulated events are used as an input for the same reconstruction and analysis programs that are used on real L3 data.

Comparison of this reconstructed Monte Carlo data with the originally generated events allows one to determine corrections needed to interpret the data recorded by the detector in terms of underlying physics models.

3.4 Energy Flow Reconstruction in L3

The event record written on tape during data taking consists of "raw data," e.g., digitized signals from TEC wires, BGO crystals, HCAL readout towers, etc. A multistep reconstruction procedure is necessary to transform this information into the

intuitively understandable form of lists of measured parameters (momentum, charge, etc.) of reconstructed particles.

The first step involves converting the digitized raw data into physical quantities such as drift distances or deposited energies, using results of dedicated subdetector calibration procedures.

In the second step, active element signals are combined within each subdetector into higher level objects, representing traces of detected particles. Charged tracks are reconstructed by performing circular fits in the $r\phi$ plane for TEC and SMD hits, after which the polar angle information for the tracks is obtained from matched z-chamber hits. Muon tracks are found in a similar way from MUCH hits. Neighbouring ECAL crystals with energy deposits larger than 10 MeV are combined into "bumps." Depending on the pattern of the crystal energy deposits, the bumps are classified as electromagnetic or hadronic, and the corresponding bump energy estimates are calculated. Similarly, HCAL hits with energies more than 9 MeV are combined into clusters.

In the next stage, information from all subdetectors is combined into objects which give the closest possible approximation to particles produced in the e^+e^- collision. ECAL bumps and HCAL clusters are matched according to their angular proximity, and where possible a TEC/SMD track is associated to the resulting object, called "A Smallest Resolvable Cluster" (ASRC). Ideally the ASRCs correspond to individual particles. However, due to the finite resolution of the detector, close-by signals in the detectors sometimes overlap, resulting in clusters which correspond to more than one particle. Muon tracks are matched to characteristic minimum ionising particle deposits in HCAL and to a TEC/SMD track whenever possible.

The last step of the reconstruction starts with the list of reconstructed hadrons, i.e., ASRCs which are not electromagnetic ECAL bumps, and attempts to obtain more precise energy estimates for them than would have been obtained by simply summing up calorimetric energy deposits. The improved energy estimator is a linear function of the energies measured in TEC/SMD, ECAL, and HCAL. The energy of

an ASRC is given by

$$\mathrm{E_{ASRC}} = \sum_i G_i(\theta) E_i, \tag{3.1}$$

where index i runs over ECAL, HCAL modules and TEC/SMD, and E_i is the energy measured by the corresponding subdetector. Different correction factors G_i are calculated for different regions of $|\cos\theta|$. They are determined with a large sample of $\mathrm{Z^0 \rightarrow q\overline{q}}$ events in a minimization which varies the G_i parameters, trying to adjust the sum of energies of all ASRCs and muons in each calibration event to the nominal value of $\sqrt{s}$ [61].

An additional set of correction factors is obtained for about 3% of events which have no reconstructed TEC information, e.g., events recorded during short periods of time in the beginning of each LEP fill when the TEC high voltage is switched off to prevent possible damage to the detector in case of a beam loss.

Combining in this way the information from the calorimeters, the central tracker, and the muon chambers, the total energy of hadronic $\mathrm{Z^0}$ events can be measured with a resolution better than 10%.

Chapter 4

Event Selection and Cross Section Measurement

The first step in my analysis of W boson properties is selection of a data sample enriched in $W^+W^- \to q\bar{q}q\bar{q}$ events. This chapter describes the methods I developed to select and reconstruct such events, and to measure their production cross section. It covers online and offline selection of hadronic multijet events, and Monte Carlo simulations I used to model the signal and background event properties. I describe the multivariate discriminators I used for separating the W^+W^- signal from potentially high backgrounds. Also addressed are the problems of reconstruction of hadronic jets, including the kinematic fits of the reconstructed jet parameters, and combination of the jets into pairs corresponding to the primary W bosons.

This chapter also describes the fit of the neural network output distribution for the multijet events selected from the data, which I use to determine the $e^+e^- \to W^+W^- \to q\bar{q}q\bar{q}$ cross section.

I also present the results of applying these methods to the L3 data samples I analyzed and discuss the systematic uncertainties of these measurements.

The data collected by L3 at $\sqrt{s}$ of 189 GeV is the most statistically significant dataset used in my analysis. In this chapter I use it, together with Monte Carlo sets generated at this value of $\sqrt{s}$, for data-Monte Carlo comparisons.

4.1 Event Characteristics and Main Backgrounds

A four-jet event recorded by the L3 detector, shown in Figure 4.1, illustrates the event properties I rely on in selecting $W^+W^- \to q\bar{q}q\bar{q}$ events in the data.

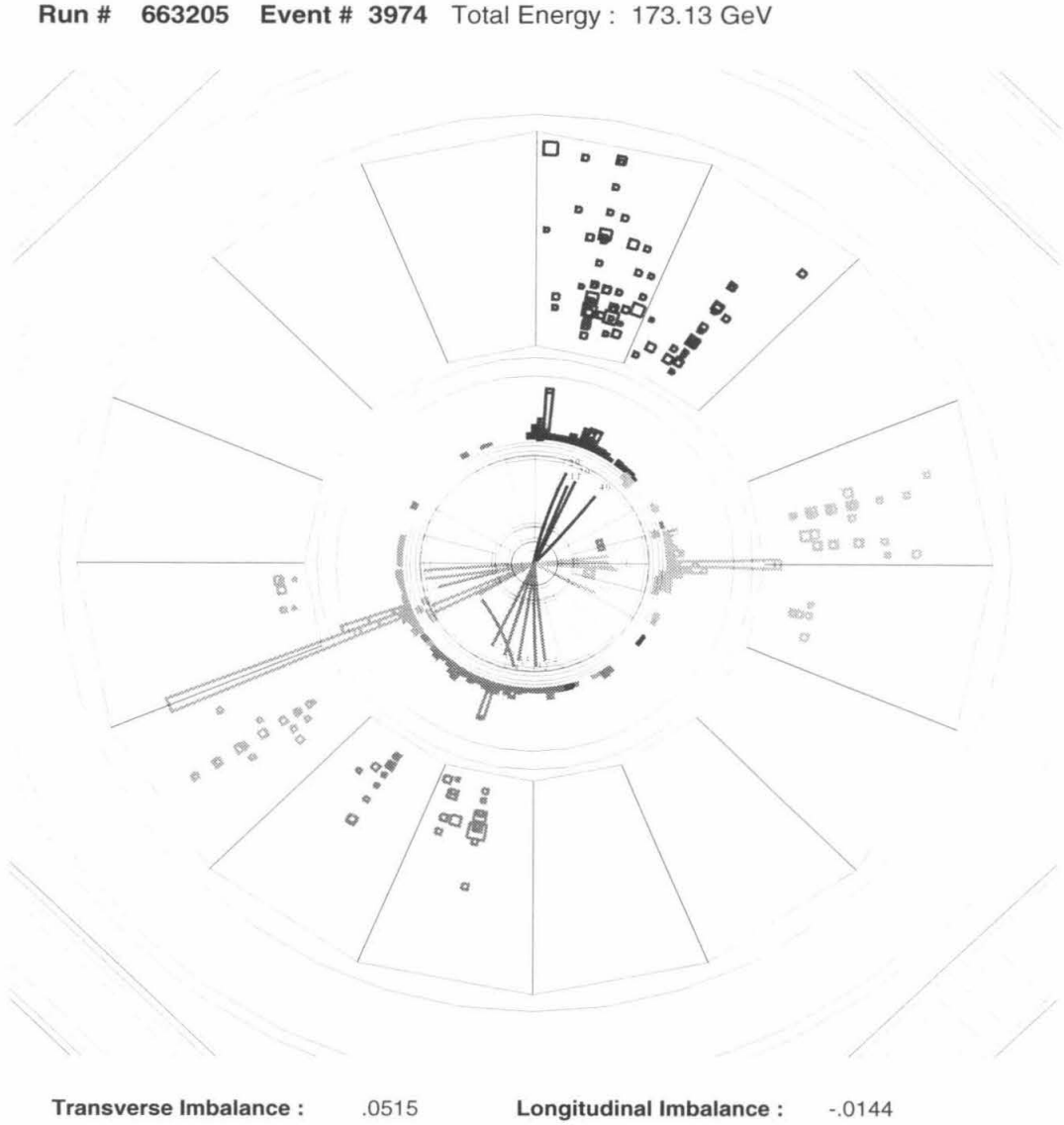

Figure 4.1: End view of a typical four-jet event recorded by the L3 detector.

Hadronization of the two high invariant mass quark-antiquark systems produced in $e^+e^- \rightarrow W^+W^- \rightarrow q\bar{q}q\bar{q}$ events, results in events with a large number of charged and neutral hadrons in the final state, the typical number of reconstructed calorimetric clusters being 50-70.

Fragmentation preserves the clear multijet topology of the $W^+W^- \rightarrow q\bar{q}q\bar{q}$ events. Most of them have a distinct four-jet signature giving a clear representation of the

underlying four quark final state. A small fraction (~10%) of the events appear to consist of more than four jets because of the gluon radiation off the quarks.

As the collision center-of-mass energies accessible at LEP 2 are not much higher than the W pair production threshold, the photons radiated off the incoming electrons typically do not carry a large momentum. This, together with the L3 detector's hermeticity and good momentum resolution for hadronic jets, accounts for the low missing energy and momentum values usually observed in $q\bar{q}q\bar{q}$ events.

Semileptonic decays of c quarks coming from $W^+ \rightarrow c\bar{s}$ decays, typically produce low energy leptons well inside jets. As there are no other significant mechanisms to produce energetic isolated photons or leptons in $W^+W^- \rightarrow q\bar{q}q\bar{q}$ events, one does not expect signal events to contain such leptons or photons.

One more important property of $W^+W^- \rightarrow q\bar{q}q\bar{q}$ decays is due to the smallness of the W boson width ($\Gamma_W \simeq 2$ GeV) relative to the W boson mass ($M_W \simeq 80$ GeV). A consequence of this is the existence in a typical four-jet $W^+W^- \rightarrow q\bar{q}q\bar{q}$ event of at least one combination of jets into two pairs with both dijet invariant masses close to 80 GeV.

Unfortunately, several Standard Model processes with non-negligible cross sections produce events which can fake the apparent characteristics of $q\bar{q}q\bar{q}$ events. Below I describe the background sources which will be corrected for in the subsequent analysis and the Monte Carlo generators used to model them. I also provide a description of the Monte Carlo simulation of the signal events, on which my measurements were based.

4.1.1 QCD Multijet Events

The most important source of background at all the energies considered is due to QCD radiative corrections to $e^+e^- \rightarrow q\bar{q}$ production. Some relevant Feynman diagrams are shown in Figure 4.2.

Although production of events with a four-jet topology is suppressed by a factor α_S^2, the $q\bar{q}$ production cross section is much larger than the signal cross section, as

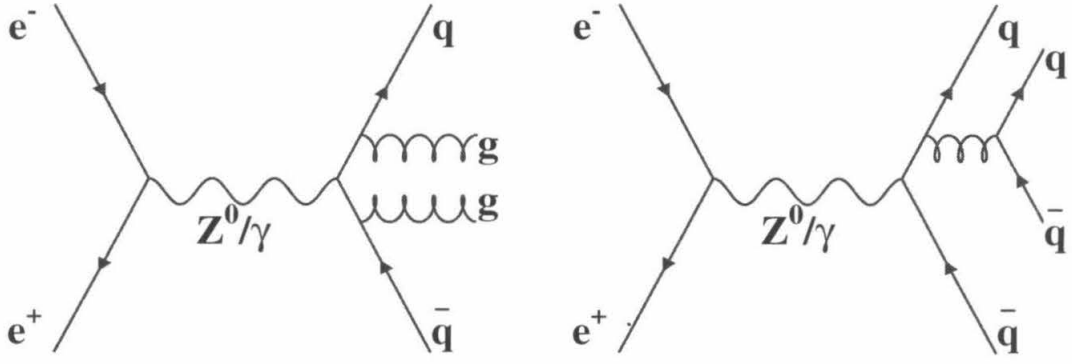

Figure 4.2: Some order α_S^2 QCD diagrams contributing to four-jet final states.

shown in Table 4.1, and leads to significant accepted background at all the energies used in the analysis. Throughout the thesis I will refer to events of this kind as $q\bar{q}$ events.

An important feature of $e^+e^- \rightarrow q\bar{q}$ annihilation, not present at center-of-mass energies at or below M_Z, is the presence of so called "radiative returns to Z^0." In such events, emission of an energetic ISR photon effectively reduces the e^+e^- collision center-of-mass energy to the Z^0 resonance and leads to production of a $q\bar{q}$ system with an invariant mass $\approx M_Z$ together with an energetic photon at a typically low polar angle.

The PYTHIA 5.7 [62] Monte Carlo event generator was used to simulate $q\bar{q}$ events. The electroweak part of the process is based on the first order $e^+e^- \rightarrow q\bar{q}$ matrix element including the γ/Z^0 interference. Initial state radiation is simulated using the JETSET parton shower algorithm. This is expected to provide an imperfect description of events with energetic, high-p_T ISR photons, but it does provide an accurate simulation of full energy $q\bar{q}$ events, which are responsible for the bulk of the background coming from this process.

The JETSET parton shower algorithm is also used to simulate QCD final-state radiation. To better model the hard gluon emission leading to QCD multijet events,

the first branch of the parton shower is adjusted to approximate the first order matrix element $q\bar{q}(\gamma)$ at this branch, thus taking advantage of both leading log and matrix element methods. The validity of this approach to the description of multijet QCD events was extensively tested at LEP 1 [63] and is discussed in Section 4.11.

Fragmentation of the resulting system of quarks and gluons was done with the LUND string fragmentation model [62] with the parameters determined in studies of LEP 1 data [64].

	$\sqrt{s}$ [GeV]			
	161.0	172.0	182.7	189.0
$\sigma(e^+e^- \to W^+W^- \to q\bar{q}q\bar{q})$ [pb]	1.76	5.67	7.17	7.59
$\sigma(e^+e^- \to q\bar{q})$ [pb]	147	121	108	98
$\sigma(e^+e^- \to Z^0Z^0)$ [pb]	0.42	0.43	0.59	0.97
$\sigma(e^+e^- \to e^+e^-$ hadrons) [pb]	12300	12900	13400	13700

Table 4.1: Standard Model cross section predictions for $e^+e^- \to W^+W^- \to q\bar{q}q\bar{q}$ and various background processes. The $e^+e^- \to W^+W^- \to q\bar{q}q\bar{q}$ cross section values given are calculated with GENTLE [65] at $M_W = 80.33$ GeV. The prediction for Z^0Z^0 cross section corresponds to a lower cut on fermion-pair masses of 10 GeV. The prediction for $e^+e^- \to e^+e^-$ hadrons corresponds to a lower cut on the hadronic mass of 3 GeV.

4.1.2 Z^0Z^0 Events

At center-of-mass energies above 2 M_Z the diagram shown in Figure 4.3 becomes important. The Z^0Z^0-mediated four-quark production is suppressed by a significant phase space factor and relatively weak coupling of Z^0 to electrons, but the resulting four-jet events, denoted in the following as Z^0Z^0 events, are indistinguishable from $W^+W^- \to q\bar{q}q\bar{q}$ events on an event-by-event basis and constitute an irreducible, albeit small, background.

Monte Carlo events of this type were generated with PYTHIA 5.7 [62], using the NC02 matrix element (the diagram shown in Figure 4.3). Uncertainties in the simulation of this electroweak process are expected to be small. A dedicated measurement by L3 [66] confirmed that the Monte Carlo correctly describes the observed rate and

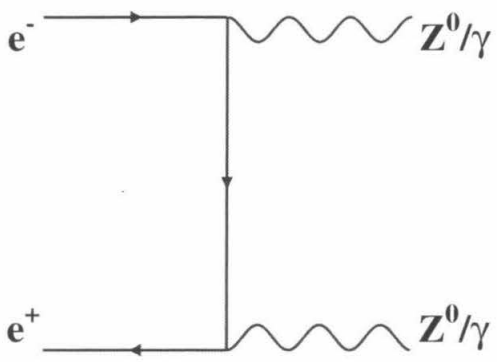

Figure 4.3: The Z^0Z^0 production diagram.

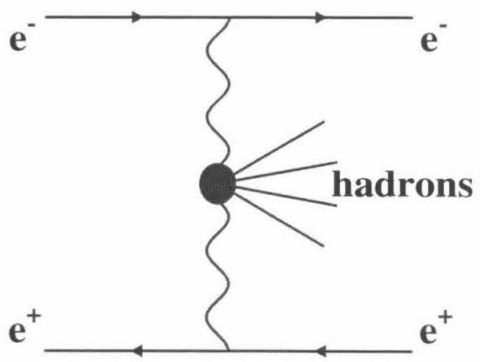

Figure 4.4: Two-photon hadronic event production.

properties of Z^0Z^0 events.

4.1.3 $\gamma\gamma$ Events

The most copious source of hadronic events at LEP 2 is interaction of virtual Weizsacker-Williams photons radiated off the incoming electrons, as schematically shown in Figure 4.4. The electrons are typically scattered by a small angle and escape detection, leading to hadronic events with large missing energy. Requiring a clear multijet structure further reduces the accepted cross section for this process. Nevertheless, due to the very high effective photon flux, the hadronic two-photon cross section is orders of magnitude larger than that of high-energy electroweak processes. Therefore the background coming from this source cannot be neglected and will be taken into account in the analysis.

Monte Carlo simulation of two-photon hadronic events is not very reliable due to incomplete theoretical understanding of the interaction of virtual photons. The PYTHIA 5.7 [62] generator, incorporating the vector dominance model (VDM), resolved and direct interactions of photons, was used as the main Monte Carlo source of $\gamma\gamma$ events. Its predictions were cross-checked with those of PHOJET [67], a dedicated

two-photon event generator based on the dual parton model (DPM) [68].

4.1.4 Monte Carlo Simulation of $W^+W^- \to q\bar{q}q\bar{q}$ Events

I rely on Monte Carlo simulations to estimate the effects of my event reconstruction and selection on W^+W^- events, the purity of the event samples I use in my analysis, and, most importantly, to infer the W boson parameters under study from the observed four-jet event properties that these parameters affect. Special attention should be paid to the choice of the W^+W^- Monte Carlo model and the uncertainties that it implies for this inference.

The KORALW 1.33 [69] event generator was the main source of W^+W^- Monte Carlo events for my analysis. It incorporates the CC03 subset of $e^+e^- \to f_1\bar{f}_2f_3\bar{f}_4$ diagrams with finite W width. The (neglected) interference with other diagrams leading to the same four-quark states, e.g., through Z^0Z^0, breaks the gauge invariance of the procedure in principle, but this effect is small numerically (in the unitary gauge) [70]. All possible W^+W^- four-fermion final states are produced and the full CKM matrix and QCD radiative corrections to $\Gamma(W \to q\bar{q}')$ are used.

Multiple ISR photons with finite transverse momenta are generated according to the $\mathcal{O}(\alpha_{em}^2)$ Yennie-Frautschi-Suura exponentiation technique [71]. Coulomb corrections [72] are taken into account as well.

JETSET parton showers and the LUND string model, with the naive singlet color connection, are used to simulate the QCD radiation off and hadronization of the quarks produced. Bose-Einstein correlations in the resulting multihadron system are modeled with the LUBOEI algorithm [73]. Dependence on these particular choices has to be investigated and will be discussed in Section 4.11.

The EXCALIBUR event generator [74], implementing the full set of $e^+e^- \to f_1\bar{f}_2f_3\bar{f}_4$ diagrams and not limited to CC03 ones, has been used in L3 for studies of $W^+W^- \to q\bar{q}\ell\nu$ events, where this limitation is important. As this is not the case for the four-jet channel, and because EXCALIBUR's ISR scheme is significantly simplified, I do not use it for my analysis. For $e^+e^- \to W^+W^- \to q\bar{q}\ell\nu$, good agreement was observed

between the KORALW and EXCALIBUR predictions.

4.2 Online Trigger

The conditions required by the L3 online trigger to be satisfied by an event to be written into the L3 data stream, constitute the first step in the selection of $W^+W^- \rightarrow q\bar{q}q\bar{q}$ events. A positive decision from the logical OR of three online Level 1 triggers is required to select a high energy hadronic event:

- The energy trigger requires either a total energy in the calorimeters of 25 GeV, or a minimum energy in the barrel region of 15 GeV in both HCAL and ECAL or 8 GeV in ECAL only. This trigger alone has an efficiency more than 99.9% for high energy hadronic events.

- The scintillator trigger requires at least 5 scintillator hits within 30 ns from a bunch crossing, covering at least a 90° angle in ϕ.

- The TEC trigger demands at least two tracks with minimum p_T of 150 MeV and acoplanarity less than 60°. The latter two triggers have efficiencies in excess of 95% for high energy hadronic events each.

Higher levels of the trigger system reduce the accepted rate of correlated calorimetric noise, beam-gas and cosmic events by applying tighter cuts on events selected by only one of the Level 1 triggers, without affecting genuine high energy events. The overall efficiency of the L3 trigger system for $W^+W^- \rightarrow q\bar{q}q\bar{q}$ events is more than 99.9% and is assumed to be 1 in the following analysis.

4.3 Detector and Data Acquisition Status

Severe malfunctioning of the detector components crucial for my analysis, such as the calorimeters or the energy trigger, can have a very large effect on the characteristics and rate of accepted events. Moreover, such time-dependent hardware problems are

difficult to incorporate in the Monte Carlo production. Therefore, to reduce systematic uncertainties related to the performance of the detector, I reject both data and Monte Carlo events in the runs during which any of the relevant L3 subsystems: the hadronic calorimeter, the electromagnetic calorimeter, the energy trigger, the luminosity monitor and the global data acquisition system, were not operating normally according to the online database. As summarized in Table 4.2, this requirement leads to only a small reduction in the integrated luminosity I use in my analysis.

Data period	$\mathcal{L}_{\text{recorded}}$ [pb^{-1}]	$\mathcal{L}_{\text{selected}}$ [pb^{-1}]	$\langle\sqrt{s}\rangle$ [GeV]
96A (July – August 1996)	10.90	10.82	161.34
96B (October – November 1996)	10.25	10.22	172.13
97 (July – November 1997)	55.46	55.30	182.68
98 (May – November 1998)	176.35	176.34	188.64

Table 4.2: Total recorded and selected integrated luminosity for the data sets used in the analysis. The accepted-luminosity averaged center-of-mass energy is also given.

4.4 Multijet Event Preselection

The online trigger does a good job in rejecting noise and cosmic events, but the output rate of the combined L3 trigger is still as high as a few Hz. The bulk of the accepted cross section at this stage, of the order of 50 nb, consists of events which are clearly incompatible with the $W^+W^- \to q\bar{q}q\bar{q}$ hypothesis, such as low-effective-$\sqrt{s}$ $\gamma\gamma$ events, dilepton events and $q\bar{q}$ events with a large energy missing due to ISR.

My multijet event preselection aims to reject such events and leave a clean sample of multijet hadronic events suitable for my measurements. This section describes the criteria I use for this purpose.

4.4.1 Multiplicity Requirements

I require the selected events to have at least 30 ASRCs with energies above 100 MeV. This cut does not affect signal events, as shown in Figure 4.6, while reducing the L3 data by a factor of 125.

In addition I require the event to have at least 10 tracks passing the criteria described in Section 3.4. The purpose of this cut is to remove events with correlated electronics noise faking large spurious energy depositions in the HCAL. An example of such an event is shown in Figure 4.5. This cut also has a negligible effect on the signal, as shown in Figure 4.6.

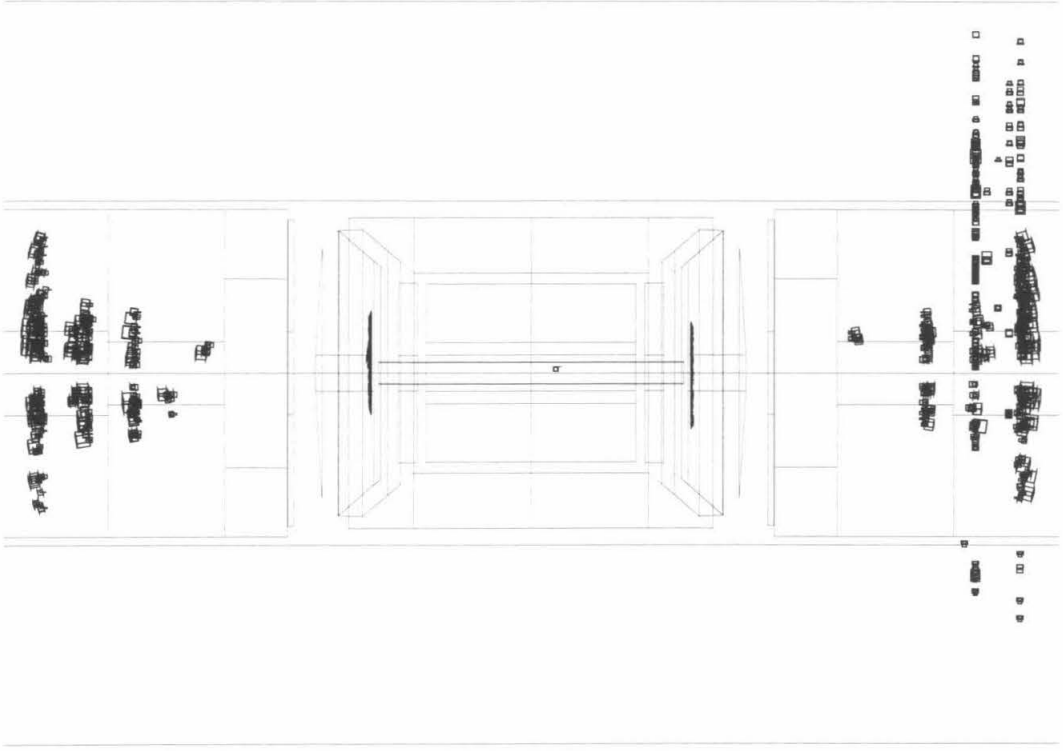

Figure 4.5: An HCAL noise event.

The track requirement for the small fraction of events without TEC information is replaced by demanding an energy of at least 20 GeV deposited in the barrel (central) part of the electromagnetic calorimeter. Studies of beam-gate events (events recorded

outside of bunch-crossing gates) showed that this provides an adequate rejection of HCAL noise events.

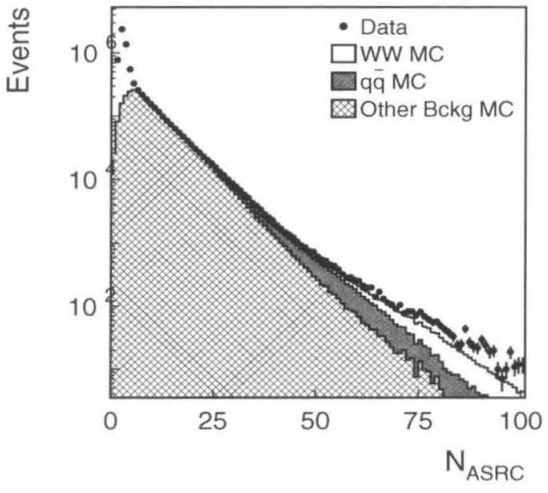

Figure 4.6: Distribution of the number of reconstructed energy flow objects. No cuts are applied. Various processes not included in the MC prediction account for its discrepancy with the data at this level.

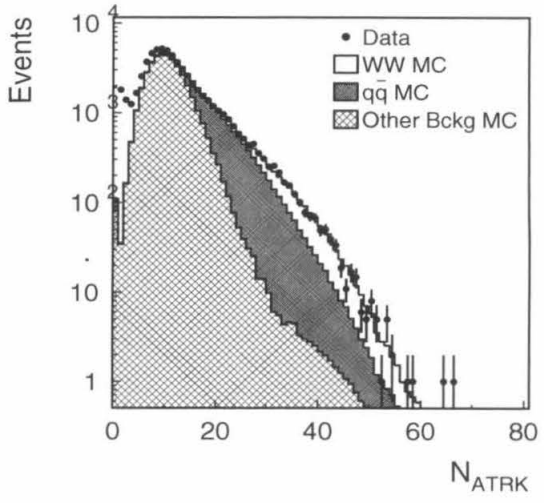

Figure 4.7: Distribution of the number of reconstructed tracks, after the total multiplicity cut has been applied.

4.4.2 Visible Energy and Energy Imbalance

For the events remaining after the ASRC and track multiplicity cuts, a set of momentum vectors $\vec{p}_i$ is reconstructed from the calorimetric clusters and tracks in the central tracker and muon chambers, as described in Section 3.4. In the following I will refer to these momentum vectors as particles.

I define the normalized visible energy E_{vis} and the longitudinal energy imbalance $E_{\|}$ as

$$E_{vis} = \frac{\Sigma p_i}{\sqrt{s}} \tag{4.1}$$

$$E_{\|} = \frac{\Sigma p_i \cos\theta_i}{\Sigma p_i}, \tag{4.2}$$

where the sums are over all the reconstructed particles, $\sqrt{s}$ is the nominal LEP center-of-mass energy.

The distributions of these two quantities for high multiplicity events selected in 98 are compared with the corresponding Monte Carlo predictions in Figure 4.8.

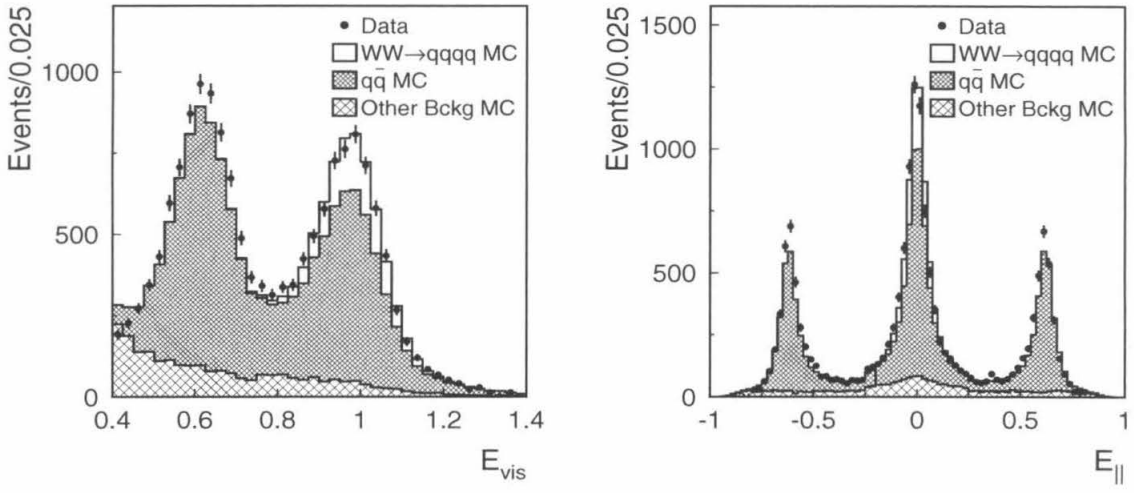

Figure 4.8: Distributions of the normalized visible energy and longitudinal energy imbalance. The discrepancy at low values of E_{vis} is due to the imperfect modeling of $e^+e^- \rightarrow e^+e^-$ hadrons.

I demand the normalized visible energy E_{vis} to be more than 0.7 and the absolute value of the longitudinal energy imbalance $E_{||}$ to be smaller than 0.25. These cuts reject most of hadronic radiative returns to Z^0, which have a preferred value for the visible energy of $\frac{s+M_Z^2}{2s}$ (0.61 - 0.66 for the energies analyzed in this thesis), and $\gamma\gamma$ events. They also help reduce background coming from semileptonic $W^+W^- \rightarrow q\bar{q}\ell\nu$ events, as those typically have significant missing energy and energy imbalance due to presence of neutrinos in the final state.

4.4.3 Lepton and Photon Rejection

Further suppression of radiative return and $W^+W^- \rightarrow q\bar{q}\ell\nu$ events is achieved by rejecting events with identified energetic photons and leptons.

Two requirements are applied to select electromagnetic ASRCs.

Firstly, most electrons and photons are fully absorbed in the BGO calorimeter. Only very energetic ones with an impact point close to a crystal edge deposit some energy in the HCAL. I demand an $\frac{E_{HCAL}}{E_{ECAL}}$ ratio of no more than 10% for an ASRC to be considered electromagnetic.

Secondly, the shape of the ECAL bump must be consistent with the electromagnetic hypothesis. A good discriminating variable sensitive to the bump shape is the $\frac{E_9}{E_{25}}$ ratio, where $E_{9(25)}$ are estimates of the bump energy in the electromagnetic hypothesis, constructed from the crystal energies in the 3×3 (5×5) matrix around the bump center of gravity. I require the $\frac{E_9}{E_{25}}$ ratio to be more than 0.95 for the selected ASRCs.

I reject the event if the most energetic ASRCs satisfying these two criteria has an energy of more than 40 GeV. As shown in Figure 4.9, the high energy part of the electromagnetic ASRC energy distribution is dominated by radiative $q\bar{q}(\gamma)$ events with a smaller contribution from $W^+W^- \rightarrow q\bar{q}e\nu$ events. The peak around 69 GeV is due to radiative returns to Z^0, where the ISR photon, with an energy of $p_\gamma = \frac{s-M_Z^2}{2\sqrt{s}}$ recoiling against a two-fermion system of an invariant mass close to M_Z, is seen in the detector.

I also select muons which satisfy the quality criteria described in Section 3.4. I reject events which contain a muon with a momentum greater than 20 GeV. Figure 4.9 shows the distribution of the reconstructed muon momentum in selected high multiplicity events. The high tail of the distribution is dominated by $W^+W^- \rightarrow q\bar{q}\mu\nu$ events.

The signal $W^+W^- \rightarrow q\bar{q}q\bar{q}$ events are not expected to have energetic leptons or photons and are practically not affected by these cuts.

4.5 Jet and W Boson Reconstruction

Most $W^+W^- \rightarrow q\bar{q}q\bar{q}$ and high energy $q\bar{q}$ events survive the cuts described above. A more detailed analysis of the jet structure and the kinematics of the events is necessary

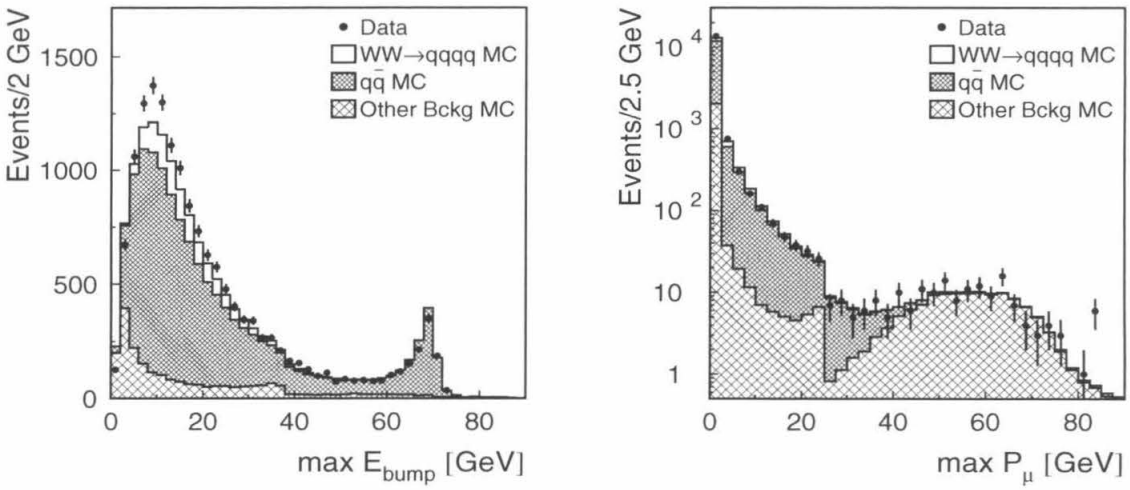

Figure 4.9: Distributions of the maximal EM bump energy and maximal muon momentum. The discontinuity in the P_μ spectrum is due to an artifact of my data analysis software.

to bring the background level down to an acceptable level. This section describes the next two steps of my selection of four-jet W^+W^- events: the reconstruction of jets and combination of jets into pairs corresponding to the primary W bosons.

4.5.1 Jet Construction Algorithm

For each high multiplicity event which satisfied the cuts described so far, I combine particles into jets using the Durham k_T algorithm [75]. This iterative combination procedure starts with the list of N reconstructed energy flow objects and finds the pair (i,j) which minimizes the jet resolution parameter

$$y_{N-1,N} = \frac{2\min(E_i^2, E_j^2)(1-\cos\theta_{ij})}{\Sigma E_k}, \tag{4.3}$$

where $E_{i,j}$ are the energies of the particles and θ_{ij} is the 3D angle formed by their momenta vectors. The two particles are combined into a new one with the 4-momentum

$$p^\mu = p_i^\mu + p_j^\mu. \tag{4.4}$$

The successive combination is repeated until there are exactly four objects left. I call these resulting objects jets in the context of my four-jet event selection. Studies of Monte Carlo $W^+W^- \to q\bar{q}q\bar{q}$ events have shown that the jet 4-momenta give a good approximation of the energies and directions of the generated quarks, accurate to approximately $\mathcal{O}(10\%)$ and $\mathcal{O}(1^\circ)$ respectively, for a typical hadronic jet produced in a $W^+W^- \to q\bar{q}q\bar{q}$ event.

I repeated my whole selection and measurement of the W mass using other jet algorithms (LUCLUS [76] and Cambridge [77]), which are significantly different from Durham and each other in their approaches to particle combination. I found no statistically significant changes in the expected performance of the analysis. This indicates that for my analysis the detector response to hadrons (calorimeter energy resolution and granularity), rather than the effects of particle (mis)assignment to jets, is the factor limiting the jet energy and angular resolution.

For the reconstructed 4 jets, I compute the parameter y_{34} as described above. This separation between the two jets closest in the Durham measure is a valuable discriminator between 4(or more)-jet events and the QCD events with two primary quarks accompanied by hard gluon radiation. In the latter case the gluons tend to be emitted with a small transverse momentum with respect to the quark-antiquark axis. This leads to low momentum jets or jets separated by a small angle. Both of these situations produce a pair of jets with a small Durham distance between them, while in $W^+W^- \to q\bar{q}q\bar{q}$ events y_{34} is determined by the initial quark kinematics, which usually leads to well-separated energetic jets and large values of y_{34}. The distribution of y_{34} in selected hadronic events is shown in Figure 4.10.

As the jet resolution parameter and, therefore, the combination procedure are not Lorentz-invariant, I do the computation in the event rest frame system. This prevents apparent event boosts, due to jet mismeasurements and undetected particles carrying away significant energy, from causing artificial effects in y_{34} and other event shape variables I use later in my analysis.

I reject the events which have y_{34} smaller than 0.0015. This value can be intuitively understood as one rejecting events if the least energetic jet is well isolated but has

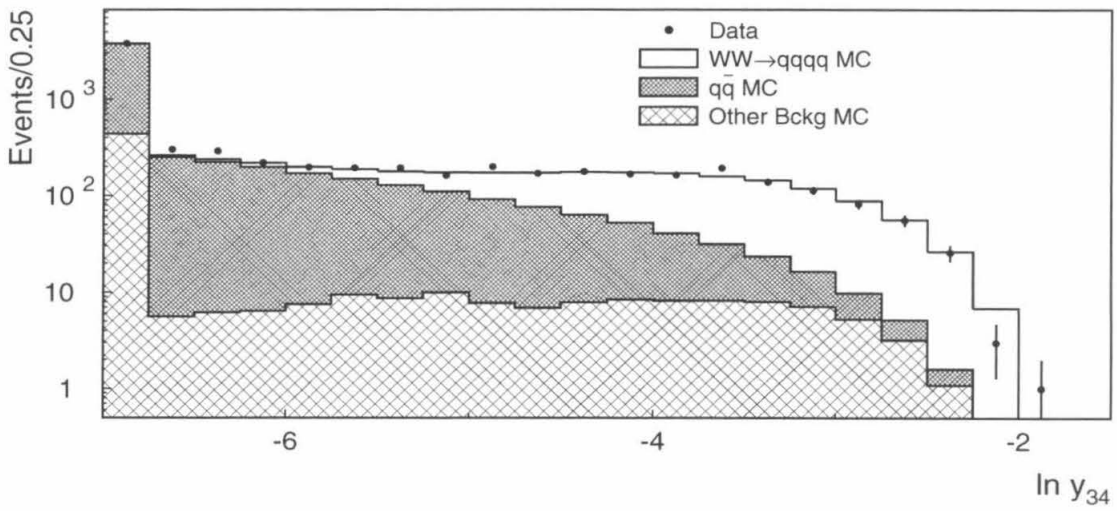

Figure 4.10: Distribution of the y_{34} parameter for selected hadronic events.

an energy of less than ~5 GeV or, alternatively, if all the four jets carry the same energy, but the angle between the two closest ones is less than ~10°.

4.5.2 Jet Quality Requirements

Having reconstructed the jets, I now apply two additional requirements on their quality.

The first one is motivated by the fact that my rejection of events with photons performs less than perfectly for events with energetic ISR photons at ECAL edges or in the EGAP calorimeter that fills the gaps between the barrel and endcap parts of the BGO calorimeter, or for events with converted ISR photons. As the radiative return cross section is very high relative to the signal, misidentification of photons as energetic jets even with a small probability would lead to a significant additional background. Therefore, I require each jet to have the fraction of its energy associated with electromagnetic deposits in ECAL less than 98%. The distribution of the maximal electromagnetic jet energy fraction $\max \frac{E^{jet}_{ECAL}}{E^{jet}}$ for selected hadronic events, after applying the y_{34} cut, is shown in Figure 4.11. A noticeable peak at high values of $\max \frac{E^{jet}_{ECAL}}{E^{jet}}$ is due to misidentified photons discussed above and is well described by

the Monte Carlo.

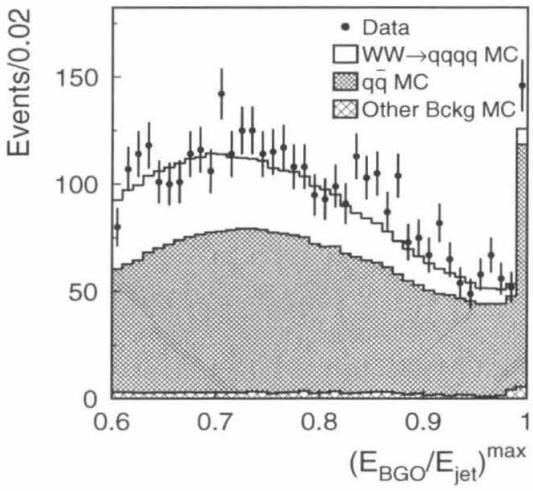

Figure 4.11: Distribution of the maximal electromagnetic jet energy fraction for events which passed the y_{34} cut.

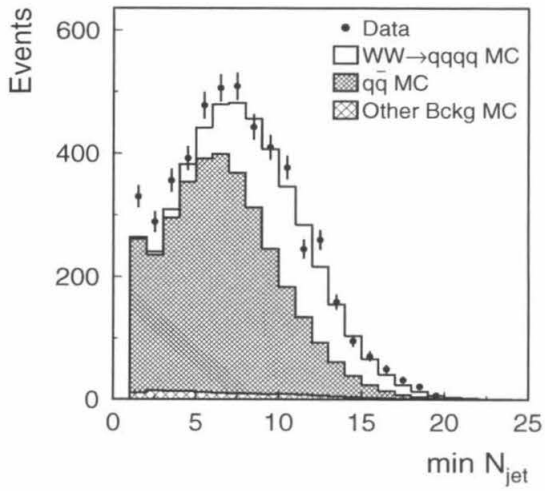

Figure 4.12: Distribution of the minimal jet multiplicity for events which passed the y_{34} cut.

Another jet quality requirement demands each jet to have at least 4 particles with momenta of at least 300 MeV each. This cut rejects events where one jet is faked by an ISR photon hitting the HCAL below the ECAL acceptance, or by a possibly-mismeasured single isolated energetic particle. The rate of the latter class of events is sensitive to the details of fragmentation and is not supposed to be reproduced reliably by Monte Carlo codes. The value of the energy cut was chosen after studies of low energy $Z^0 \rightarrow q\bar{q}$ data. The chosen value optimizes the agreement between data and Monte Carlo, but the agreement remains imperfect because of the difficulties of properly simulating particle-detector interactions. The distribution of the minimal jet multiplicity $\min N_{E>300\ MeV}$ for selected hadronic events, after applying the y_{34} cut, is shown in Figure 4.12.

4.5.3 Constrained Kinematic Fit of Measured Jet Parameters

After applying the rejection described above, I am left mostly with genuine high energy hadronic events without significant initial state radiation. Given an ideal detector, one would expect these events to be reconstructed with the total energy within ~1 GeV (typical ISR energy loss) of the nominal LEP $\sqrt{s}$, and very low transverse and longitudinal energy imbalance. In a real detector, statistical and systematic uncertainties of particle identification and momentum measurement lead to a rather different picture, with the resolution on the total energy of ~15 GeV and significant momentum imbalance for high energy hadronic events.

I try to partially correct the jet parameter measurement by means of a constrained kinematic fit. I choose a new set of values for each jet's energy and direction {E,θ,ϕ} so that they satisfy the energy-momentum conservation constraints

$$\Delta E \equiv \sum_{i=1,4} E_i - \sqrt{s} = 0 \tag{4.5}$$

$$\Delta P_x \equiv \sum_{i=1,4} E_i \sqrt{1 - \frac{m_{0i}^2}{E_{0i}^2}} \sin\theta_i \cos\phi_i = 0 \tag{4.6}$$

$$\Delta P_y \equiv \sum_{i=1,4} E_i \sqrt{1 - \frac{m_{0i}^2}{E_{0i}^2}} \sin\theta_i \sin\phi_i = 0 \tag{4.7}$$

$$\Delta P_z \equiv \sum_{i=1,4} E_i \sqrt{1 - \frac{m_{0i}^2}{E_{0i}^2}} \cos\theta_i = 0, \tag{4.8}$$

while minimizing the difference between the new fitted set of parameters and the measured ones {E_0,θ_0,ϕ_0}. The measure of the difference I use is a χ^2 defined as

$$\chi^2 = \sum_{i=1,4} \sum_{\{E,\theta,\phi\}} \frac{(x - x_0)^2}{\sigma_x^2(E,\theta)}, \tag{4.9}$$

where the sum is over the measured parameters of the four reconstructed jets. My choice of constraints is equivalent to fixing the velocities of the jets to the measured

values. This reduces the number of free parameters in the fit and aims to approximate the correlation intrinsic in the jet energy and mass measurement. I ignore correlations between measured jet energies and angles and correlations between different jets, which is a valid assumption for high multiplicity, collimated, well-separated jets.

The resolutions σ_x depend on jet energy and polar angle as

$$\sigma_E = \sqrt{E}\sqrt{a_E + \frac{b_E}{E}}(1 + \frac{c_E}{\min(\theta, \pi - \theta)} + d_E|\theta - \frac{\pi}{2}|^2) \quad (4.10)$$

$$\sigma_\theta = \frac{1}{\sqrt{E}}\sqrt{a_\theta + \frac{b_\theta}{E}}(1 + \frac{c_\theta}{\min(\theta, \pi - \theta)} + d_\theta|\theta - \frac{\pi}{2}|^2) \quad (4.11)$$

$$\sigma_\phi = \frac{1}{\sqrt{E}}\frac{1}{\sin\theta}\sqrt{a_\phi + \frac{b_\phi}{E}}(1 + \frac{c_\phi}{\min(\theta, \pi - \theta)} + d_\phi|\theta - \frac{\pi}{2}|^2). \quad (4.12)$$

The parameters a_x, b_x, c_x, d_x were obtained from studies of $e^+e^- \rightarrow W^+W^-$ Monte Carlo events [78]. As shown in Section 4.11, the L3 detector simulation provides an adequate description of the actual detector response.

I do the minimization of the χ^2 by gradient descent with the help of the MINUIT software package [79]. The constraints are implemented adding a penalty contribution to the χ^2

$$\Delta\chi^2{}_{4C} = \frac{\Delta E^2 + \Delta P_x^2 + \Delta P_y^2 + \Delta P_z^2}{\sigma_0^2}, \quad (4.13)$$

where the parameter σ_0 is gradually decreased during several iterations of the fit. The fit I described above is referred to as a 4C fit, according to the number of constraints used.

The new jet momentum 4-vectors obtained in the minimization satisfy energy-momentum conservation by construction and greatly improve the measurement of the jet-kinematics-based quantities which are correlated with the total event energy-momentum. The large effect of the kinematic fit on the average of the reconstructed masses of the two W bosons in $W^+W^- \rightarrow q\bar{q}q\bar{q}$ events is shown in Figure 4.13.

Figure 4.14 shows the distribution, in both data and Monte Carlo, of the 4C kinematic fit probability $P_{\chi^2}(\chi^2{}_{4C}; 4)$, defined as the probability of drawing a value

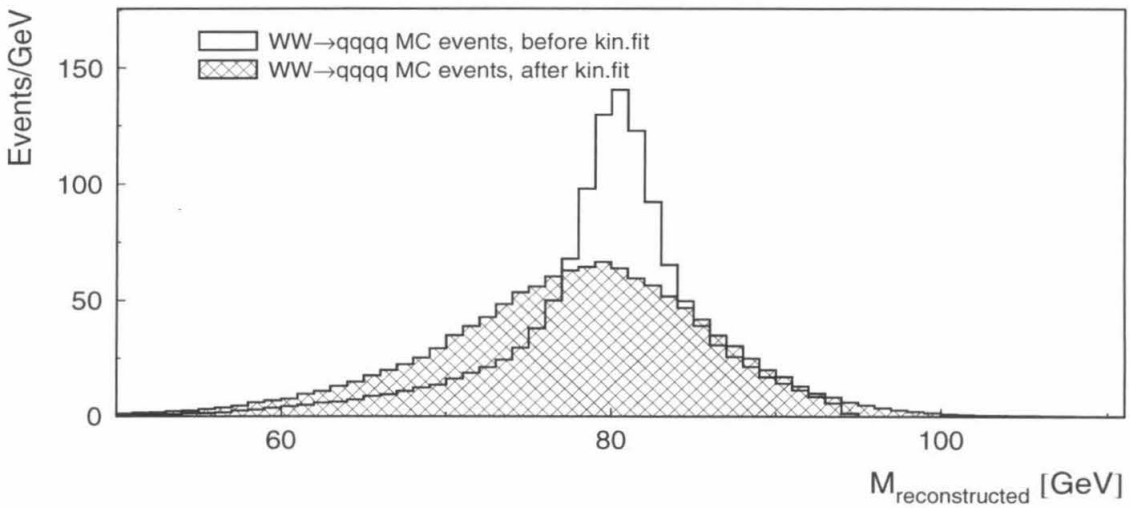

Figure 4.13: Distribution of the average reconstructed W mass before and after 4C kinematic fit for selected $W^+W^- \rightarrow q\bar{q}q\bar{q}$ Monte Carlo events. The resolution on the average mass is improved from 9 GeV to 1.5 GeV by the fit.

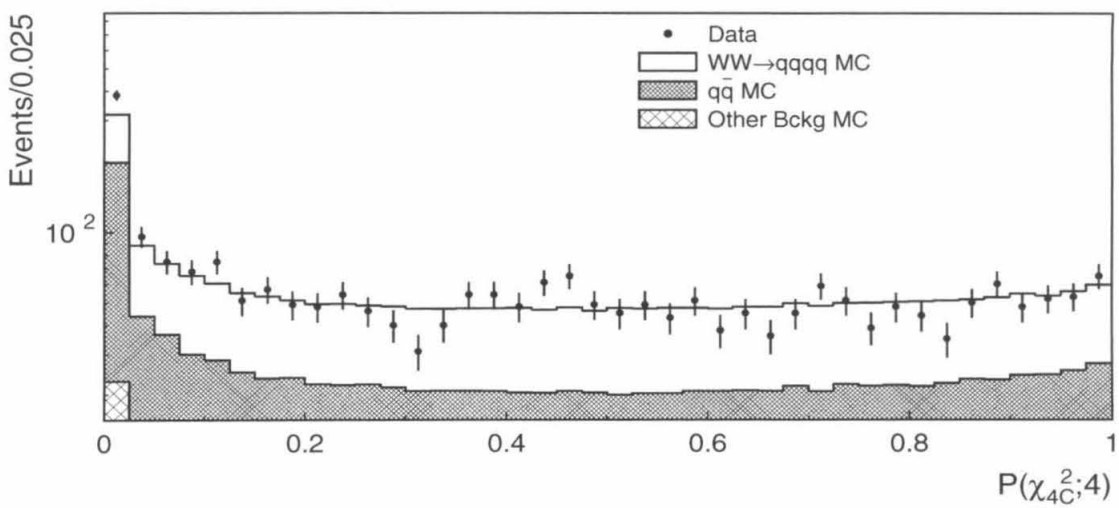

Figure 4.14: Distribution of the 4C kinematic fit probability.

higher than the observed χ^2 from the χ^2 distribution with 4 degrees of freedom. The data are well described by the Monte Carlo in the whole range of the fit probability. The flatness of the distribution for $W^+W^- \rightarrow q\bar{q}q\bar{q}$ events indicates correctness of the

parametrization of the jet errors I used. The peak at low values of the fit probability consists of events in the non-Gaussian tails of the measured jet momentum distribution, mostly due to particle and shower losses, and events with significant initial state photon or final state gluon radiation, with a small admixture of $W^+W^- \to q\bar{q}\tau\nu$ events with the τ-lepton decaying hadronically, that passed the rejection described above. I reject such mismeasurements by demanding the events I consider in the following analysis to have a $P_{\chi^2}({\chi^2}_{4C}; 4)$ of at least 0.1%.

Energy-momentum conservation equations (4.5-4.8) are not the only constraints one can reasonably apply to a $W^+W^- \to q\bar{q}q\bar{q}$ event. The experimental statistical error on a reconstructed W invariant mass, typically of the order of 10 GeV, is much larger than the Breit-Wigner width of the produced W boson, $\Gamma_W \approx 2$ GeV. I can exploit this property of genuine W^+W^- events and assume, once I have combined the jets into two jet pairs, that the two reconstructed W bosons (jet pairs) have equal masses. This gives me an additional constraint which I use in a 5C fit.

The 5C fit is performed for each of the three possible combinations of the jets into pairs. The decision on which pair combination is most likely to represent the two primary W bosons is taken at a later stage in my selection and is described in Subsection 4.5.4.

I form the ith jet combination (i=1,3) by assuming that jets 1 and $i+1$ come from the same W, and the other two jets come from the other one.

The penalty addition to the χ^2 (4.13) is modified to assure that the two W candidates have equal reconstructed masses after the fit,

$$\Delta{\chi^2}_{5C,i} = \Delta{\chi^2}_{4C} + \frac{(E_1 + E_{i+1} - \frac{\sqrt{s}}{2})^2}{\sigma_0^2}. \tag{4.14}$$

As computed with the jet momenta obtained in the 5C fit, the two dijet pairs have the same mass m^{5C}. My measurement of the W mass described in Chapter 5 is based on the analysis of the distribution of this quantity. The W boson masses I obtain after the 4C kinematic fit, two for each jet combination, are more difficult to use for this purpose because of the significant (negative) correlation between them, introduced by

the fit, and non-parabolic errors, introduced by the constraints (non-linear in $m^{4C}_{1,2}$). m^{5C} efficiently combines information contained in $m^{4C}_{1,2}$, taking the above details into account and providing a single M_W estimator per jet combination.

An additional benefit of the 5C fits is the set of the fit probabilities, computed for the χ^2 distribution with 5 degrees of freedom. The fit probability $P_{\chi^2}(\chi^2{}_{5C}; 5)_i$ is a powerful test of the hypothesis that the ith jet combination maps correctly onto the original W bosons. The set of the probabilities $P_{\chi^2}(\chi^2{}_{5C}; 5)_i$ (i=1,3) can also be used to solve the combinatorial problem of choosing the combination of jets with the highest likelihood of correct mapping, as discussed in the following Section.

4.5.4 Jet Combination Algorithms

A problem unique to the $W^+W^- \to q\bar{q}q\bar{q}$ channel is the presence of three possible ways to form two dijet systems in each event. The knowledge of which combination corresponds to the two $q\bar{q}'$ pairs coming from the two W bosons is important for my analysis and especially for the measurements of the W mass and $W^+W^-\gamma/Z^0$ couplings. The ambiguity cannot be resolved for each and every event, but one can devise statistical methods to exploit kinematic properties of $W^+W^- \to q\bar{q}q\bar{q}$ events and to make choices with much higher efficiency than the $\frac{1}{3}$ obtained with random picking.

In my analysis several algorithms of finding the correct jet combination in $W^+W^- \to q\bar{q}q\bar{q}$ events were used for different purposes:

- The Δm algorithm starts with rejecting the combination with the lowest sum of the reconstructed W masses $\Sigma m \equiv m_1^{4C} + m_2^{4C}$, as this combination is unlikely to represent the two W bosons. Out of the remaining two combinations, I choose the one with the smallest difference of the reconstructed W masses $\Delta m \equiv |m_1^{4C} - m_2^{4C}|$.

- Alternatively, one can choose the combination with the highest Σm as the most likely to be the correct one. In a $W^+W^- \to q\bar{q}q\bar{q}$ event, random jet combinations typically do not have invariant masses as high as M_W.

- I can improve the Σm algorithm by using the decision variable of a more general form $\Sigma'\mathrm{m} \equiv \alpha \min \mathrm{m}^{4C}_{1,2} + \max \mathrm{m}^{4C}_{1,2}$. The parameter α optimizing the performance is found to be close to 2 at all the energies considered.

- The χ^2 algorithm orders the combinations according to the probability of the 5C kinematic fit described in Subsection 4.5.3. Incorrect combinations are expected to have low kinematic fit probabilities, as they do not usually satisfy the equal mass constraint.

There is a good data-MC agreement in the variables these algorithms rely on, as shown in Figure 4.15.

	$\sqrt{s}$ [GeV]			
Algorithm	161.0	172.0	182.7	189.0
Δm	55%	66%	70%	72%
Σm	81%	68%	48%	36%
Σ'm	83%	74%	61%	54%
χ^2	52%	58%	61%	62%

Table 4.3: Correct combination efficiency of the jet combination algorithms used in the analysis, at different center-of-mass energies.

The performance of the algorithms, defined as the probability of choosing the correct combination in a $\mathrm{W^+W^-} \to \mathrm{q\bar{q}q\bar{q}}$ event selected with the cuts described so far in this Chapter, was determined with Monte Carlo events generated at different center-of-mass energies, and is shown in Table 4.3. The performance of all considered algorithms varies considerably with energy, because of the significant changes in the kinematics of the $\mathrm{W^+W^-}$ events as the center-of-mass energy rises from the threshold to higher values. The Δm algorithm is the most efficient one at higher energies. Closer to the threshold it suffers from the limited phase space which significantly affects the underlying Breit-Wigner distribution. The Σm and Σ'm algorithms' performance, while the highest near threshold, decreases rapidly as the center-of-mass energy and the rate of random high-invariant-mass combinations increase.

I use the Σ'm and Δm algorithms in the analysis of the 161, 172 and the 183,

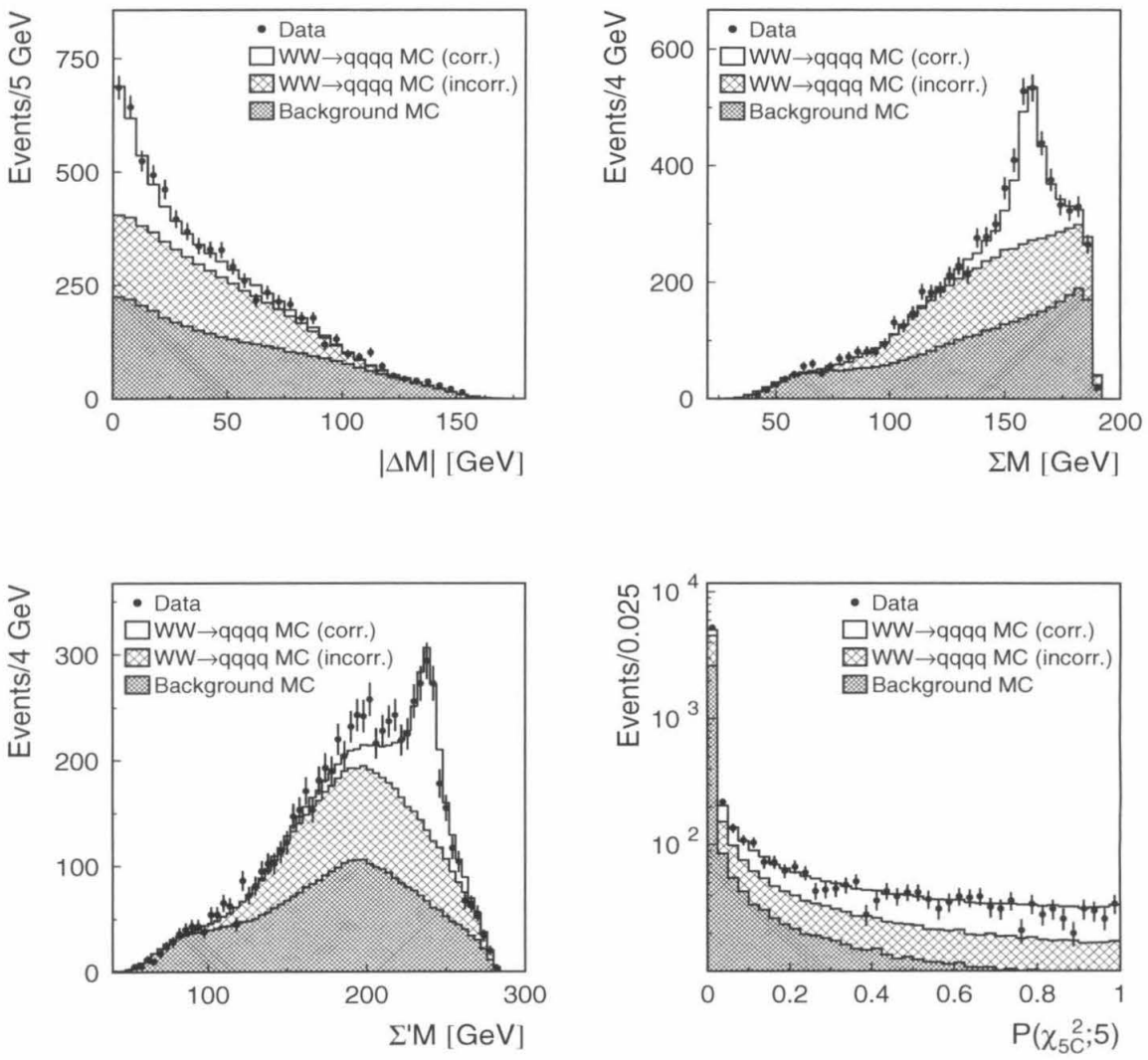

Figure 4.15: Distributions of (a) Δm, (b) Σm, (c) Σ'm, (d) $P_{\chi^2}(\chi^2{}_{5C}; 5)$ for selected multijet events. Three combinations per event are shown.

189 GeV data respectively, to find the preferred jet combination for the purposes of the W^+W^- production cross section measurement and the analysis of anomalous couplings described in Chapter 6. The choice of the combination algorithm is more complicated in the case of the W mass measurement, and will be discussed in Chapter 5.

There is an intrinsic uncertainty in the performance definition due to the ambiguity

of mapping reconstructed jets onto the generated quark momenta. Using different mapping algorithms, I checked that the uncertainty is of the order of 1% and can be neglected.

4.6 Preselection Summary

The preselection I described so far consists of the following requirements:

- $N_{ASRC} \geq 30$
- $N_{ATRK} \geq 10$ or $N_{ATRK} = 0$ and $E_{ECAL\ barrel} > 20$ GeV
- $E_{vis} > 0.7$
- $|E_{\|}| < 0.25$
- $\max E_{EM} < 40$ GeV
- $\max P_{\mu} < 20$ GeV
- $y_{34} > 0.0015$
- $\max \frac{E^{jet}_{ECAL}}{E^{jet}} < 0.98$
- $\min N_{E>300\ MeV} \geq 4$
- $P_{\chi^2}(\chi^2_{4C}; 4) > 0.1\%$

The results of applying these cuts to the data and Monte Carlo samples I considered are summarized in Table 4.4. The preselection achieves efficient rejection of the background events clearly incompatible with the $W^+W^- \rightarrow q\bar{q}q\bar{q}$ hypothesis. Good agreement between the data and Monte Carlo is observed at all considered energies.

	Data period			
	96A	96B	97	98
$\sqrt{s}$ MC [GeV]	161.0	172.0	182.7	189.0
$\varepsilon(e^+e^- \to W^+W^- \to q\bar{q}q\bar{q})$ [%]	94.0	93.7	92.2	92.9
$\varepsilon(e^+e^- \to W^+W^- \to q\bar{q}e\nu)$ [%]	3.1	1.3	1.1	1.1
$\varepsilon(e^+e^- \to W^+W^- \to q\bar{q}\mu\nu)$ [%]	0.4	0.1	0.2	0.1
$\varepsilon(e^+e^- \to W^+W^- \to q\bar{q}\tau\nu)$ [%]	2.7	2.5	2.3	2.3
$\sigma(e^+e^- \to q\bar{q})_{acc}$ [pb]	10.5	8.2	6.3	5.8
$\sigma(e^+e^- \to Z^0Z^0)_{acc}$ [pb]	0.136	0.132	0.211	0.393
$\sigma(e^+e^- \to e^+e^-$ hadrons$)_{acc}$ [pb]	0.07	0.03	0.03	0.01
$N_{selected}$	138	142	797	2402
$N_{SM\ exp.}$	135 ± 12	142 ± 12	741 ± 27	2384 ± 49

Table 4.4: Efficiencies for different W^+W^- event classes, SM background cross sections and number of data events accepted by the preselection cuts. Also given is the standard deviation on the total number of selected events expected in the SM.

4.7 Neural Network Discriminator

The cuts described so far reduce the accepted $q\bar{q}$ cross section by a factor of 17 and the accepted $\gamma\gamma$ cross section by a factor of 10^6, but the backgrounds are still large relative to the $W^+W^- \to q\bar{q}q\bar{q}$ signal cross section.

Moreover, after the rejection I am left with a clean sample of high energy hadronic multijet events with no clear-cut characteristics that would allow me to reject them without cutting into the sample of $W^+W^- \to q\bar{q}q\bar{q}$ events I aim to select.

Nevertheless, one can attempt to combine the information contained in several variables x_i (i=1,N), each not effective enough on its own, into a more efficient multidimensional discriminator $F(\vec{x})$.

Accepting events with all the discriminating variables above their thresholds (cuts) is equivalent to using a discriminator with the very special form of a multidimensional θ-function $\theta(x_1 - x_1^{cut}, ..., x_1 - x_N^{cut})$ which ignores potentially important correlations between the variables and is not necessarily optimal. Analysis of the differential cross section $\frac{d\sigma}{dx_1 ... dx_N}$ would in principle make full use of all the available information, but is numerically complicated for all but prohibitively small values of N by the limited

available Monte Carlo statistics.

A compromise between the two approaches is reached by the artificial neural network method. I chose to use a feed forward neural network with one hidden layer [80] to separate $W^+W^- \rightarrow q\bar{q}q\bar{q}$ from the dominant QCD $q\bar{q}$ background.

The discriminating variable, referred to as the neural network output, is defined as

$$\mathcal{N} = g(\sum_{i=1,15} \alpha_i g(\sum_{j=1,7} \beta_{ij} x_j)), \tag{4.15}$$

where the activation function $g(x)$ is

$$g(x) = \frac{1}{1+e^{-x}}, \tag{4.16}$$

x_j are 7 input variables, normalized to be in the [0,1] range, and the weights α_i, connecting the 15 nodes of the hidden layer with the output, and β_{ij}, connecting the hidden layer with the 7 inputs, are determined during the neural network training. The chosen neural net configuration provides for an efficient projection onto the discriminant of the information contained in $\frac{d\sigma}{dx_1 \ldots dx_N}$ of a very general form, while taking correlations between the input variables into account. I found that increasing further the number of input variables, nodes in the hidden layer or the number of hidden layers does not lead to an increase in the neural network performance.

The following 7 variables were identified as having the most discriminating power and were used as inputs to the neural net:

- $\log y_{34}$, the logarithm of the Durham measure introduced in Subsection 4.5.1.
- spherocity of the event

$$\mathcal{S} \equiv \min_{\hat{n}} (\frac{4}{\pi} \frac{\sum_{particles} E_i \sin\theta_i}{\sum_{particles} E_i})^2, \tag{4.17}$$

  obtained by the minimization of the expression which can be intuitively understood as the normalized total transverse momentum relative to the event axis

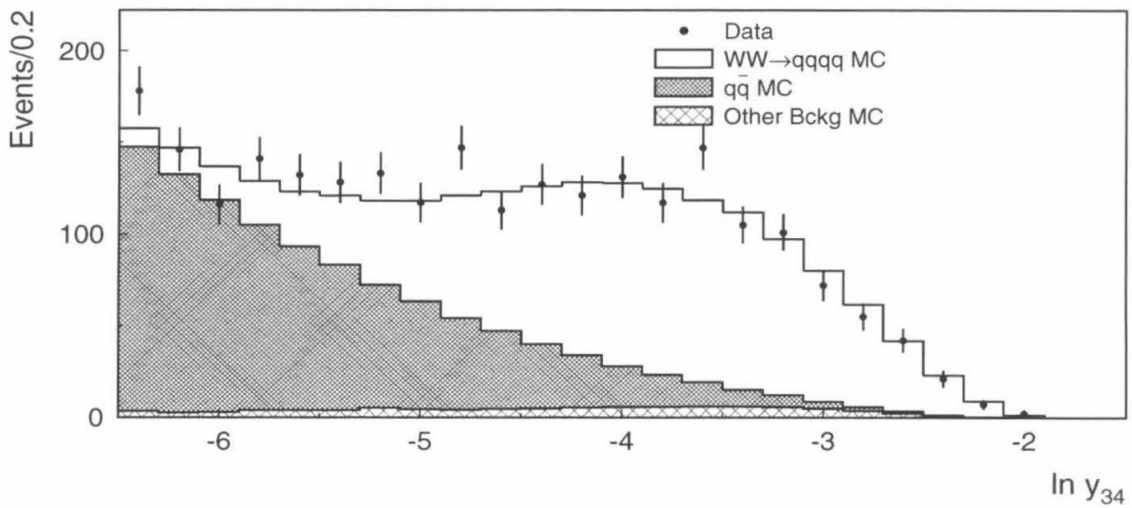

Figure 4.16: Distribution of the y_{34} distance after the preselection.

which varies during the minimization. Spherocity assumes values from 0, for an event which consists of two exactly back-to-back jets of particles, to 1, for a completely isotropic event. The spherocity and y_{34} were computed in the event rest frame.

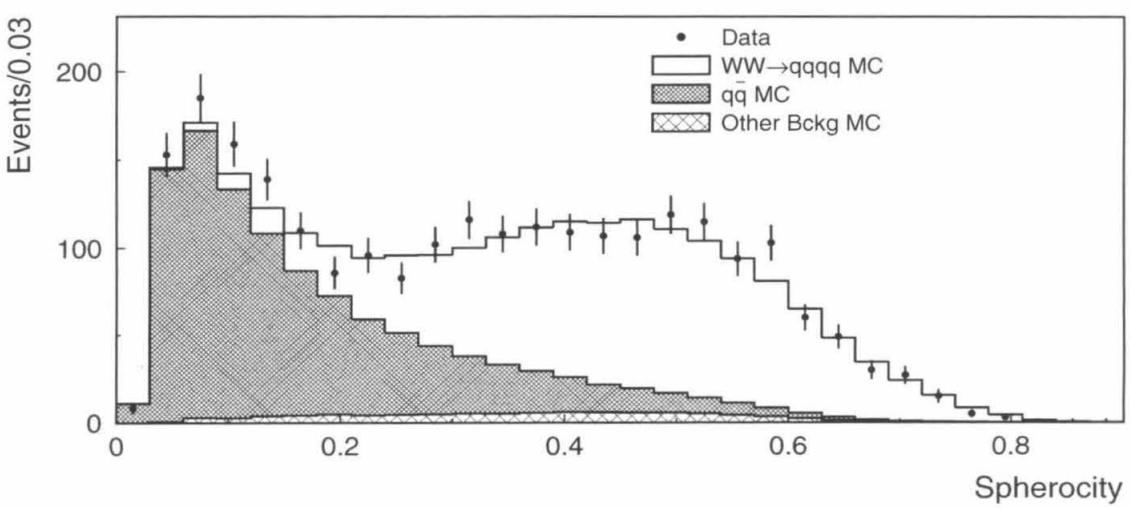

Figure 4.17: Distribution of the spherocity after the preselection.

- E_{min} and E_{max}, the energies of the least and most energetic jet in the event,

after the 4C kinematic fit. In a QCD $q\bar{q}$ event the least (most) energetic jet is usually due to the gluon (quark) coming from a $q\bar{q}(\gamma)$ branching, resulting in a typically large energy difference between the two jets. The energy is split more evenly between jets in a $W^+W^- \rightarrow q\bar{q}q\bar{q}$ event. Close to the W^+W^- threshold each of the four jets has ideally an energy close to $\frac{M_W}{2}$.

- signed m^{4C} mass difference $m^{4C}{}_1$-$m^{4C}{}_2$ for the jet combination chosen with the Δm algorithm. This is small in magnitude for signal events and unlimited for the background.

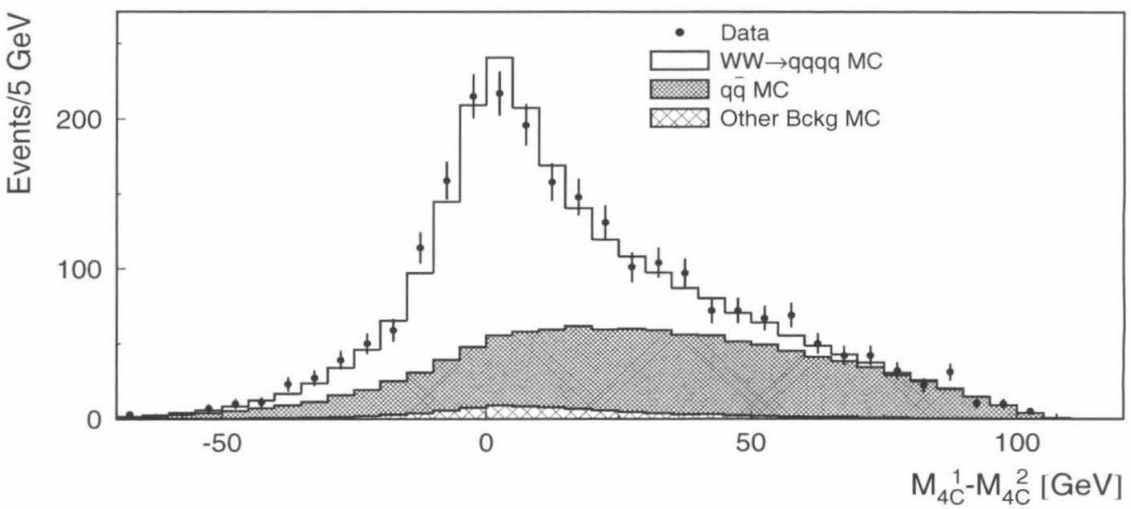

Figure 4.18: Distribution of the W mass difference $m^{4C}{}_1$-$m^{4C}{}_2$ for the jet combination found with the Δm algorithm after the preselection. The distribution is asymmetric because of my ordering of the reconstructed W bosons (the first jet pair contains the most energetic jet by construction).

- θ_{min}, the smallest angle found between any two reconstructed jets. It is expected to be large for $W^+W^- \rightarrow q\bar{q}q\bar{q}$ events and small for $q\bar{q}$ events due to QCD dynamics.

- $< M_h >$, the average mass of the two jets (hemispheres) reconstructed when the Durham recombination proceeds to combine all the particles into two jets. For

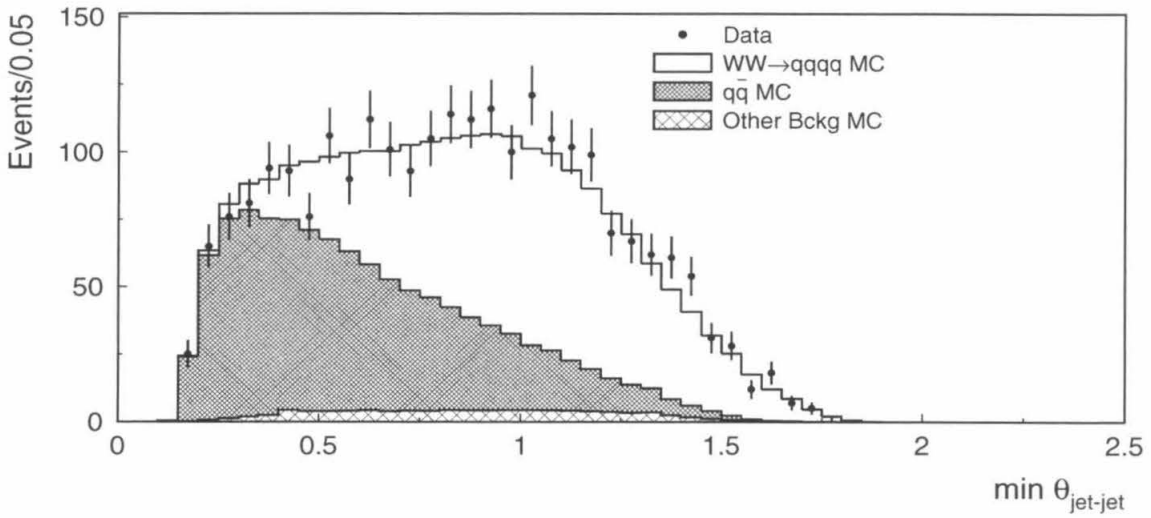

Figure 4.19: Distribution of the minimal jet-jet angle $\theta_{\min}$ after the preselection.

$q\bar{q}$ events the two jets will hopefully correspond to the two primary quarks and have relatively low mass each, while it is impossible to split a typical $W^+W^- \rightarrow q\bar{q}q\bar{q}$ event into two low-mass systems.

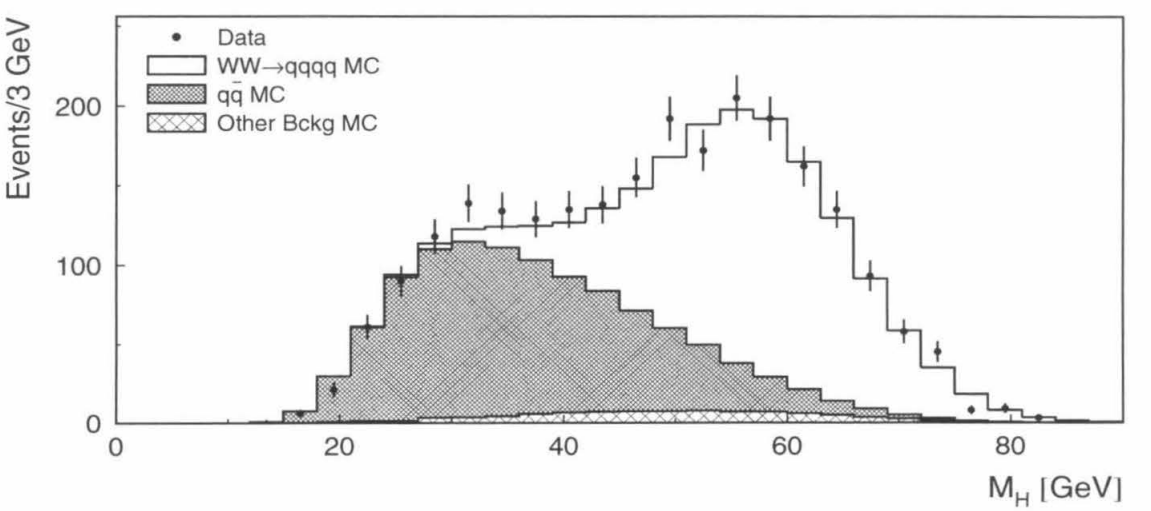

Figure 4.20: Distribution of the average hemisphere mass after the preselection.

Distributions of some of the neural network input variables are shown in Figures 4.16-4.20. There is a good agreement between the data and the Monte Carlo

predictions.

The neural network is trained, i.e., the weights $\vec{w} \equiv \{\alpha_i, \beta_{ij}\}$ are optimized, to produce $\mathcal{N}$ values close to 1 for Monte Carlo $W^+W^- \to q\bar{q}q\bar{q}$ events and 0 for $q\bar{q}$ events. Training is achieved by using the back propagation algorithm which adjusts the weights in a gradient descent minimization

$$\vec{w} \rightarrow \vec{w} - \eta \frac{\partial \mathcal{E}}{\partial \vec{w}} \tag{4.18}$$

of the classification error

$$\mathcal{E} = \sum_{MC\ events} (\mathcal{N} - \mathcal{N}_{target})^2 \tag{4.19}$$

$$= \sum_{q\bar{q}\ MC\ events} \mathcal{N}^2 + \sum_{W^+W^-\ MC\ events} (\mathcal{N} - 1)^2. \tag{4.20}$$

The classification error $\mathcal{E}$ is computed on a large (training) sample of Monte Carlo events with $q\bar{q}$ and W^+W^- events mixed in the proportion expected in the selected data samples. The optimization was redone for each energy point used in my analysis, resulting in four different neural networks used for the four data samples I analyzed.

The distributions of the neural network output for data events accepted by the preselection at different energies are compared to the corresponding Monte Carlo predictions in Figure 4.21. The signal-background separation achieved is superior to that which is possible with any other single variable.

4.8 Selection of $W^+W^- \to q\bar{q}q\bar{q}$ events

The neural network provides an efficient means of selecting the clean four-jet event samples I use for the measurements of the W mass and triple gauge boson couplings described in Chapters 5 and 6.

Demanding accepted events to have the neural network output above some threshold $\mathcal{N}_{\min}$ reduces the amount of background by a further factor of 4-10 and brings the purity of the selected $W^+W^- \to q\bar{q}q\bar{q}$ events to an acceptable level. The value of

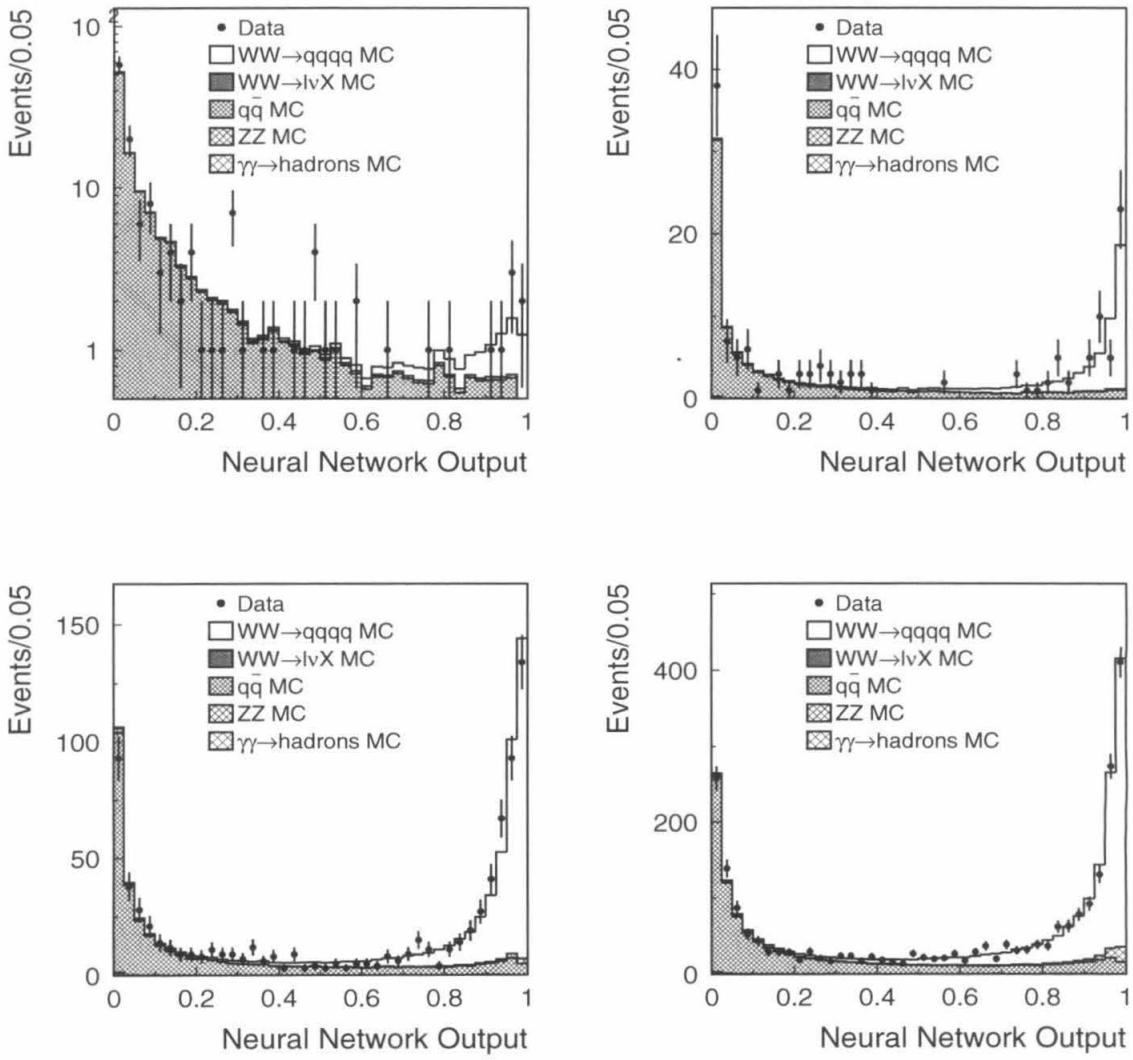

Figure 4.21: Distributions of the neural network output for the data events selected in (a) 96A, (b) 96B, (c) 97, and (d) 98 and the corresponding Monte Carlo predictions. The Monte Carlo distributions are normalized to the cross sections determined in Section 4.9.

the $\mathcal{N}$ cut $\mathcal{N}_{\min}$ was chosen at each energy point to optimize the expected statistical error of the $W^+W^- \to q\bar{q}q\bar{q}$ cross section measurement obtainable with the achieved

selection,

$$\langle \frac{\Delta\sigma(W^+W^- \to q\bar{q}q\bar{q})}{\sigma(W^+W^- \to q\bar{q}q\bar{q})} \rangle = \langle \frac{\sqrt{N^{W^+W^-}_{accepted} + N^{q\bar{q}}_{accepted}}}{N^{W^+W^-}_{accepted} + N^{q\bar{q}}_{accepted} - \langle N^{q\bar{q}}_{accepted} \rangle} \rangle. \quad (4.21)$$

The optimal value of the cut was found to be close to 0.6 at all energies considered. The performance of the selections achieved and the results of applying them to the L3 data, are given in Table 4.5.

	Data period			
	96A	96B	97	98
$\sqrt{s}$ MC [GeV]	161.0	172.0	182.7	189.0
$\varepsilon(e^+e^- \to W^+W^- \to q\bar{q}q\bar{q})$ [%]	79.4	83.8	85.2	84.0
$\varepsilon(e^+e^- \to W^+W^- \to q\bar{q}e\nu)$ [%]	0.4	0.2	0.2	0.3
$\varepsilon(e^+e^- \to W^+W^- \to q\bar{q}\mu\nu)$ [%]	0.0	0.0	0.0	0.0
$\varepsilon(e^+e^- \to W^+W^- \to q\bar{q}\tau\nu)$ [%]	0.5	0.7	0.7	0.6
$\sigma(e^+e^- \to q\bar{q})_{acc}$ [pb]	0.94	1.15	1.16	1.13
$\sigma(e^+e^- \to Z^0Z^0)_{acc}$ [pb]	0.045	0.067	0.151	0.316
$N_{selected}$	14	57	468	1393
$N_{SM\ exp.}$	26 ± 5	62 ± 8	414 ± 20	1391 ± 37

Table 4.5: Efficiencies for different W^+W^- event classes, SM background cross sections and number of data events accepted by the neural network selection. Also given is the standard deviation on the total number of selected events expected in the SM.

4.9 Measurement of the $W^+W^- \to q\bar{q}q\bar{q}$ Cross Section

One could proceed to extract the $W^+W^- \to q\bar{q}q\bar{q}$ cross section from the number of events which passed the neural network selection, corrected for accepted background and selection efficiency. That would not be an efficient use of all the available information though, as such an approach effectively treats equally all selected events irrespective of their likelihood of being $W^+W^- \to q\bar{q}q\bar{q}$. This likelihood can indeed

vary from almost 100% for events with a $\mathcal{N}$ close to 1, down to much lower values for events with $\mathcal{N}$ just above $\mathcal{N}_{\min}$.

I attempt to use this additional knowledge in the determination of the $W^+W^- \to q\bar{q}q\bar{q}$ cross section by using a maximum likelihood fit of the $\mathcal{N}$ distribution for events which passed my preselection.

I divide the [0,1] range into $N_{bins} = 40$ equal bins and find the $W^+W^- \to q\bar{q}q\bar{q}$ and $q\bar{q}$ cross sections by maximizing the binned likelihood

$$\ln L_{\mathcal{N}} = \sum_{i=1,40} (d_i \ln p_i - p_i) + \sum_{j=1,N_{MC}} \sum_{i=1,40} (M_{ji} \ln t_{ji} - t_{ji}), \tag{4.22}$$

where d_i is the number of data events in the ith bin, M_{ji} is the number of Monte Carlo events of class j in the same bin, and t_{ji} are auxiliary parameters varied during the maximization. In my fits index j spans the $N_{MC} = 5$ Monte Carlo event classes which contribute to the neural network output distribution ($W^+W^- \to q\bar{q}q\bar{q}$, $W^+W^- \to q\bar{q}\ell\nu$, $q\bar{q}$, Z^0Z^0, and $e^+e^- \to e^+e^-$ hadrons). The total Monte Carlo prediction for bin i, p_i is given by

$$p_i = \mathcal{L} \sum_{j=1,N_{MC}} \varepsilon_j^{preselection} \sigma_j \frac{t_{ji}}{\sum_{i=1,N_{bins}} t_{ji}}. \tag{4.23}$$

The chosen form of the likelihood takes into account the statistical fluctuations of the bin-by-bin Monte Carlo predictions due to the finite available Monte Carlo statistics. t_{ji} can be interpreted as the (unknown) prediction of Monte Carlo j in bin i, i.e., the mean of the Poisson distribution a random drawing of which produced M_{ji}.

A very convenient property of the likelihood (4.22) is the possibility of performing the optimization in $N_{bins} \times N_{MCs}$ dimensions defined by the t_{ji} variables analytically [81]. The maximization for $W^+W^- \to q\bar{q}q\bar{q}$ and $q\bar{q}$ is performed numerically with the help of the MINUIT software package.

As was noted before, both the $W^+W^- \to q\bar{q}q\bar{q}$ and $q\bar{q}$ cross sections were varied in the maximization. The aim of leaving the $q\bar{q}$ cross section free is to decrease the sensitivity of the measured $W^+W^- \to q\bar{q}q\bar{q}$ cross section on the QCD prediction for

the multijet $q\bar{q}$ event rates. In effect, any changes that affect the rate normalization of preselected $q\bar{q}$ events without affecting the shape of the $\mathcal{N}$ distribution for them, will not introduce any bias into the measurement of the $W^+W^- \to q\bar{q}q\bar{q}$ cross section with floating $\sigma(e^+e^- \to q\bar{q})$.

The more efficient use of the information contained in the data $\mathcal{N}$ distribution, by the maximum likelihood fit, leads to a gain of about 5% in the expected statistical accuracy of the measurement, compared to the simple event counting measurement.

The results of the fit performed on the data are reported in Table 4.6.

Data Period	$\sigma(q\bar{q}q\bar{q})$ [pb]	$\sigma(q\bar{q}q\bar{q})_{SM}$ [pb]	$\sigma(q\bar{q})$ [pb]	$\sigma(q\bar{q})_{SM}$ [pb]
96A	$0.85^{+0.43}_{-0.34}$	–	$167.9^{+15.9}_{-14.9}$	147
96B	$5.32^{+0.90}_{-0.83}$	5.67	$129.6^{+15.6}_{-14.6}$	121
97	$8.30^{+0.47}_{-0.46}$	7.17	$109.2^{+6.9}_{-6.7}$	108
98	$7.53^{+0.26}_{-0.25}$	7.59	$104.5^{+3.8}_{-3.8}$	98

Table 4.6: $e^+e^- \to W^+W^- \to q\bar{q}q\bar{q}$ and $e^+e^- \to q\bar{q}$ cross sections determined in neural network output fits. Statistical and Monte carlo statistics errors are combined. Also included are contributions due to measured cross section correlations. The Standard Model cross sections calculated with GENTLE are also given for comparison. The threshold cross section is strongly dependent on M_W and is not given.

There is a good general agreement between the measured $W^+W^- \to q\bar{q}q\bar{q}$ cross sections and the Standard Model expectations calculated with the GENTLE semianalytical code [65].

4.10 Rarity Analysis

As a cross-check, I use another method of measuring the $W^+W^- \to q\bar{q}q\bar{q}$ cross section using the same 7 variables that were used as neural network inputs.

I repeat the fit described in the previous section with another multidimensional discriminator, rarity [82]. The neural network input variables, already normalized to be in the [0,1] range, are transformed if necessary as $x_i \to 1 - x_i$ so that they assume high values for the $W^+W^- \to q\bar{q}q\bar{q}$ signal and lower values for the $q\bar{q}$ background. An

auxiliary variable $\mathcal{F}$, computed for an event $\vec{d}$ is the fraction of $W^+W^- \to q\bar{q}q\bar{q}$ Monte Carlo events with $x_i < d_i$ for all i,

$$\mathcal{F}(d_1, ..., d_N) = \frac{1}{\sigma(q\bar{q}q\bar{q})} \int_0^{d_1} ... \int_0^{d_N} \frac{d\sigma(q\bar{q}q\bar{q})}{dx_1...dx_N} dx_1...dx_N. \quad (4.24)$$

The rarity $\mathcal{R}$ is defined as the integral probability of $\mathcal{F}$,

$$\mathcal{R}(d_1, ..., d_N) = \frac{1}{\sigma(q\bar{q}q\bar{q})} \int_0^1 ... \int_0^1 \frac{d\sigma(q\bar{q}q\bar{q})}{dx_1...dx_N} \theta(\mathcal{F}(d_1, ..., d_N) - \mathcal{F}(x_1, ..., x_N)) dx_1...dx_N. \quad (4.25)$$

The rarity distribution is flat, by construction, for the $W^+W^- \to q\bar{q}q\bar{q}$ signal, and is concentrated at low values of $\mathcal{R}$ for background.

This discriminator is different from the neural network in its use of the information contained in the spectrum $\frac{d\sigma}{dx_1...dx_7}$. A difference in the results of the fits using the two discriminators would indicate incorrect modeling by the Monte Carlos I used of the correlations between the neural network input variables.

The results of the fits using the rarity distributions shown in Figure 4.22 are reported in Table 4.7 and are in good agreement with the results obtained in the neural network output fits.

Another measurement [83] using the same differential cross section, based on the minimal spanning tree method (a multidimensional generalization of the runs test) gave consistent estimates of the $W^+W^- \to q\bar{q}q\bar{q}$ cross section and confirmed the compatibility of the data with the Monte Carlo simulations.

4.11 Analysis Uncertainties

The $W^+W^- \to q\bar{q}q\bar{q}$ cross section measurement method described in this chapter relies on Monte Carlo simulation of the neural network output distribution for signal and background events, as well as the preselection efficiency for W^+W^- events. Imperfect modeling of these quantities might lead to a bias of the measured cross section. In

Data Period	$\sigma(q\bar{q}q\bar{q})$ [pb]	$\sigma(q\bar{q}q\bar{q})_{SM}$ [pb]	$\sigma(q\bar{q})$ [pb]	$\sigma(q\bar{q})_{SM}$ [pb]
96A	$0.74^{+0.45}_{-0.35}$	1.76	$166.0^{+16.1}_{-15.0}$	147
96B	$5.60^{+0.94}_{-0.86}$	5.67	$125.8^{+15.6}_{-14.5}$	121
97	$8.32^{+0.48}_{-0.47}$	7.17	$110.5^{+7.1}_{-6.9}$	108
98	$7.60^{+0.26}_{-0.25}$	7.59	$103.4^{+3.8}_{-3.8}$	98

Table 4.7: $e^+e^- \to W^+W^- \to q\bar{q}q\bar{q}$ and $e^+e^- \to q\bar{q}$ cross sections determined in rarity fits. Statistical and Monte carlo statistics errors are combined. Also included are contributions due to measured cross section correlations. The Standard Model cross sections calculated with GENTLE are given for comparison.

this section I give estimates for the most important effects which might contribute to such a bias.

I consider three main categories of systematic errors: the ones due to imperfect modeling of signal event properties, uncertainties of the rate and properties of accepted background events, and uncertainties due to mismodeling of the L3 detector response, common to both signal and background.

Most of the uncertainties are expected to be much smaller than the statistical errors of the measurements. One cannot evaluate such biases in the usual way of checking the stability of the result with respect to variations of selection criteria or other technical parameters of the measurement. Such variations would lead to changes of the selected data sample and to statistical variations which would be large compared to the systematic effects under investigation. Therefore, I estimate all systematic errors by varying parameters of Monte Carlo models and then repeating the measurements with modified Monte Carlo samples but without changing the data.

The errors were reevaluated for each data-taking period. In the text I quote numbers relevant for the measurement at $\sqrt{s} = 189$ GeV. Estimates for other data periods are very similar and the differences are indicated whenever necessary.

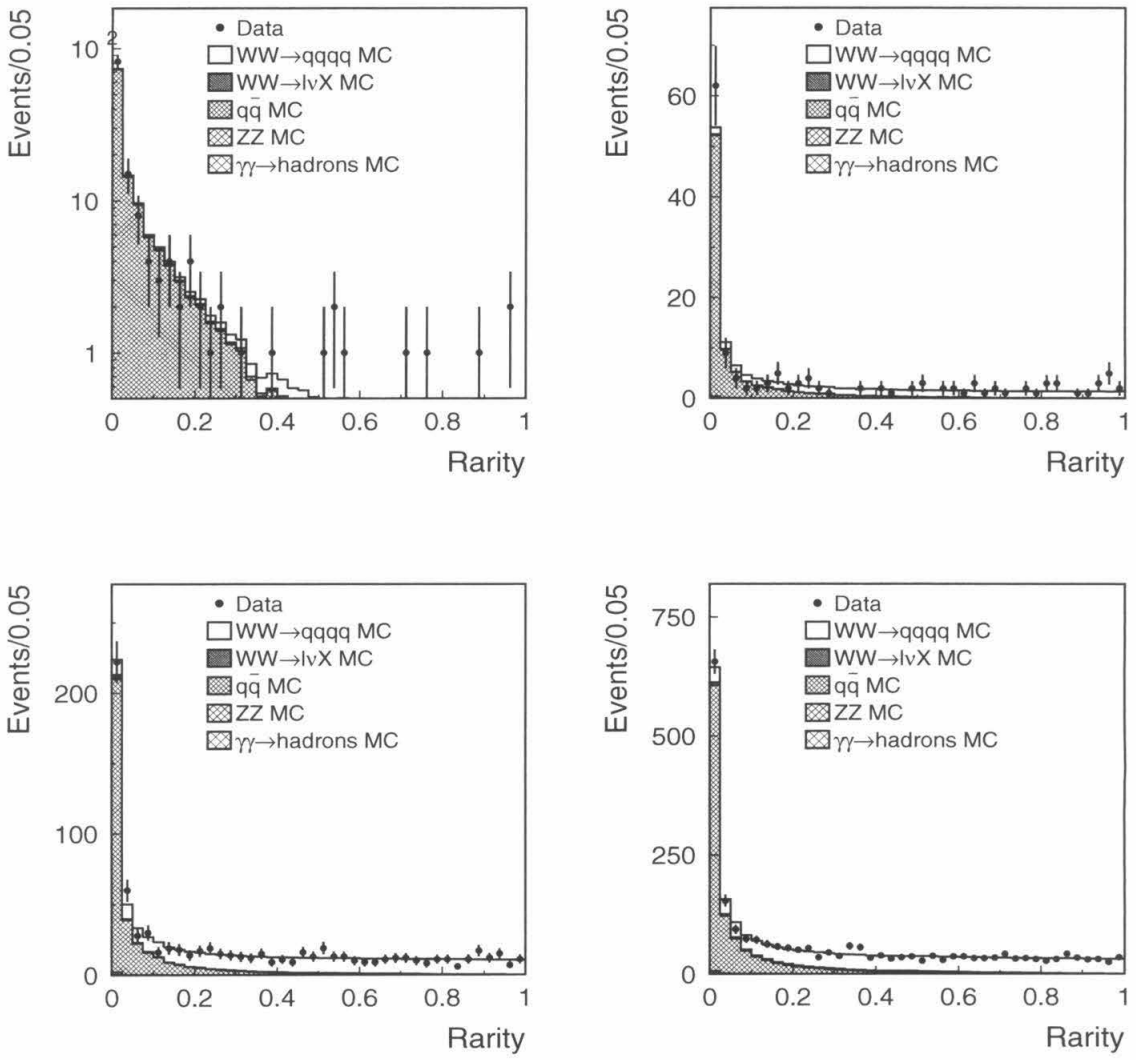

Figure 4.22: Distributions of the event rarity for the data events selected in (a) 96A, (b) 96B, (c) 97, and (d) 98 and the corresponding Monte Carlo predictions. The Monte Carlo distributions are normalized to the cross sections measured in this section.

4.11.1 Modeling of the Detector Response

Mismodeling detector behaviour affects properties of both signal and background events. The corresponding systematic errors are correlated with those of measurements using $W^+W^- \to q\bar{q}\ell\nu$ events. Fortunately, one can gauge, and put tight limits

on such mismodeling using a well-understood control sample of hadronic events.

The data collected during calibration LEP runs at the Z^0 peak provides such a sample. The Z^0-mediated $q\bar{q}$ production has a cross section of 30 nb and is the dominant process in e^+e^- collisions at $\sqrt{s} \approx 91$ GeV. Employing the event selection described in [84], it is possible to select $Z^0 \rightarrow q\bar{q}$ events with efficiencies in excess of 99% and with an admixture of background events, mostly from $Z^0 \rightarrow \tau^+\tau^-$ decays, of approximately 0.3%. The selected high statistics, kinematically unbiased, and virtually background-free samples of $q\bar{q}$ events are a good probe of the detector response to jets of hadrons.

To estimate possible imperfections of the Monte Carlo description of the detector behavior, I compared the data summarized in Table 4.8, with the corresponding MC predictions.

Year	$\mathcal{L}_{\text{selected}}$ [pb^{-1}]	$\langle\sqrt{s}\rangle$ [GeV]	$N^{q\bar{q}}_{\text{selected}}$
1996	1.17	91.1100	35519
1997	2.17	91.2378	65324
1998	3.01	91.3123	90512

Table 4.8: Total selected integrated luminosity for the data sets used in the analysis. Accepted-luminosity averaged center-of-mass energy and number of selected $q\bar{q}$ events are also given.

- In order to judge possible detector miscalibration I study the angular dependence of the energy flow using the selected sample of $q\bar{q}$ events. I measure the total energy of the particles deposited in a unit of solid angle, normalized to the event center-of-mass energy and averaged over the $q\bar{q}$ sample. I assume cylindrical symmetry of the detector, and sum up the energy in rings equidistant in $\cos\theta$. The ratio of the distributions thus obtained for data and MC is shown in Figure 4.23.

  I estimate the effect of the jet energy scale miscalibration by redoing the cross section measurement after correcting energies of all reconstructed particles in the MC samples I use by the found ratio. The procedure leads to a change of

the fitted $W^+W^- \to q\bar{q}q\bar{q}$ cross section of 0.02 pb.

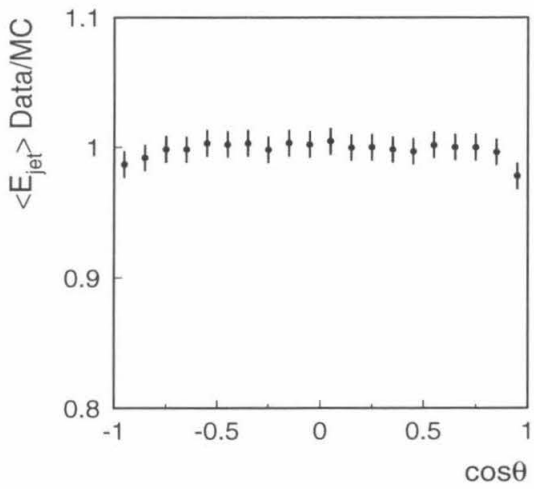

Figure 4.23: Angular distribution of average jet energy in $Z^0 \to q\bar{q}$ events. Ratio of the data and MC distributions is shown.

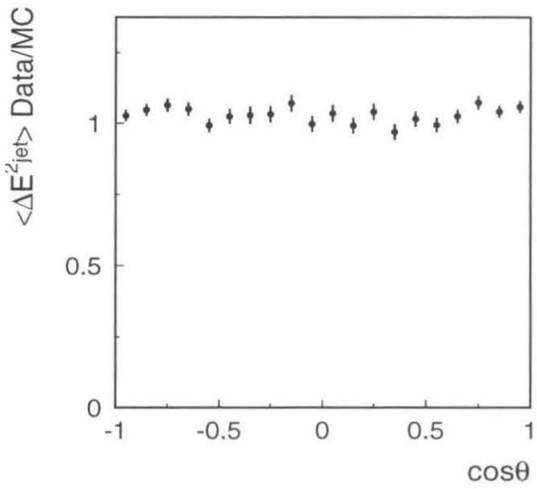

Figure 4.24: Angular distribution of jet energy variance in $Z^0 \to q\bar{q}$ events. Ratio of the data and MC distributions is shown.

- A similar mismatch is found in the modeling of jet energy resolutions. Figure 4.24 shows the ratio of the spreads (variances) of the energies of jets deposited in $\cos\theta$ rings.

  I estimate the effect of the mismatch by redoing the cross section fit after smearing reconstructed jet energies in MC events with Gaussian random noise of the magnitude chosen to reproduce the resolutions found in data. This leads to a (negligible) change of the fitted $W^+W^- \to q\bar{q}q\bar{q}$ cross section of 0.003 pb.

- Another way to estimate possible systematic cross section biases due to detector miscalibration comes from studying the subdetector composition of jet energies. The correction factors applied to raw deposited energies, to compute a particle energy as described in Section 3.4, differ in data and MC by on the order of 3% for ECAL and 10% for HCAL clusters. One can take the difference of the corrections as an estimate of the calibration uncertainty.

I redo the analysis after applying the data correction factors to Monte Carlo events, i.e., ignoring this difference, to estimate the possible influence of detector miscalibration/mismodeling. I observe a shift in the fitted $W^+W^- \to q\bar{q}q\bar{q}$ cross section of 0.04 pb, which I take as an estimate of the systematic error due to uncertainties of jet energy measurement. It is more conservative than but in rough agreement with the two estimates obtained from energy scale and resolution corrections, described above.

- An incorrect description of the detector geometry might lead to a systematic mismeasurement of jet directions. This might influence the cross section measurement and the reconstruction of invariant W masses and is especially important for the measurement of the W mass.

  To quantify possible mismodeling I study the acollinearity between two jets, constructed by the Durham algorithm in the selected $Z^0 \to q\bar{q}$ events, as a function of the direction of the more energetic jet in the event. Misalignments of jet polar and azimutal angles are studied separately. But for initial state radiation, negligible for events at the Z^0 peak, the two jets are produced back-to-back in the laboratory frame, and would have zero acollinearity if reconstructed by a perfect detector.

  I study both the mean of the distributions in each bin of $\cos\theta$, i.e., the bias of the jet direction determination, and the variance, i.e., the angular resolution. The agreement between data and Monte Carlo in both quantities is illustrated in Figures 4.25 and 4.26.

  I estimate the effect of possible jet direction mismeasurement by redoing the cross section fit after applying the found θ-dependent θ and ϕ corrections to directions of all reconstructed jets in the MC samples. This leads to a change of the fitted $W^+W^- \to q\bar{q}q\bar{q}$ cross section of 0.01 pb.

- A small mismatch is also found in the modeling of the resolution of the jet direction measurements. Figure 4.26 shows the ratio of the spreads (variances)

of the acollinearities of jets in two-jet $Z^0 \rightarrow q\bar{q}$ events, as a function of $\cos\theta$.

I redo the cross section measurement after smearing reconstructed jet directions in MC events with Gaussian random noise of the magnitude equal to the found data-MC differences, resulting in a change of the fitted $W^+W^- \rightarrow q\bar{q}q\bar{q}$ cross section of 0.002 pb.

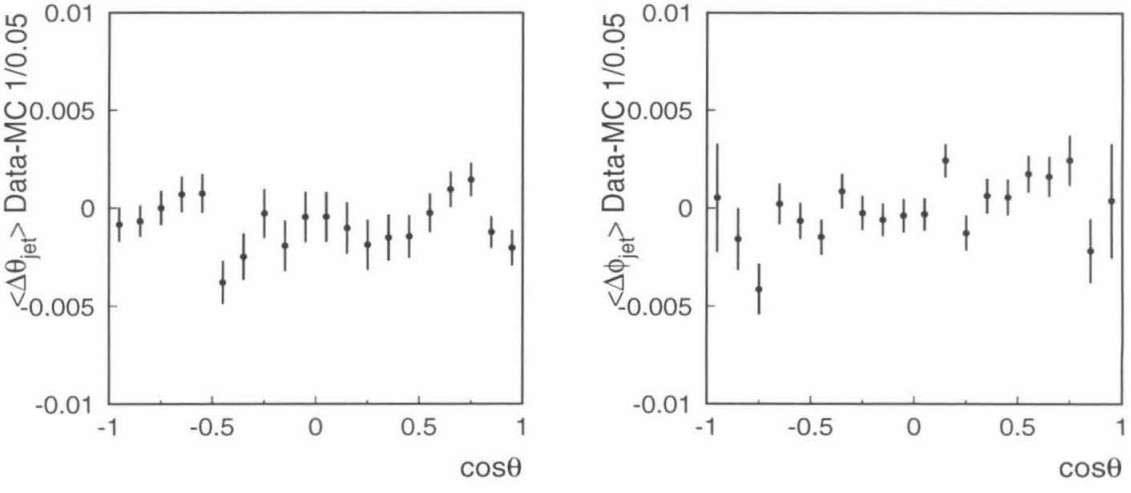

Figure 4.25: Angular dependence of reconstructed jet angle biases in $Z^0 \rightarrow q\bar{q}$ events. Differences of the data and MC distributions for θ and ϕ biases are shown.

4.11.2 Modeling of the W^+W^- Signal Properties

- The distributions of the kinematic variables of W^+W^- events used in the cross section measurement depend on the properties of the W boson. A mismatch between the values of M_W, Γ_W assumed by the Monte Carlo, and the true, unknown values of these parameters could lead to a bias of the cross section estimation. The size of such effects was evaluated by repeating the measurements using W^+W^- Monte Carlo sets generated at different values of M_W, in the 80-81 GeV range, and Γ_W, in the 1.51-2.71 GeV range. The observed dependence of the fitted cross section on the Monte Carlo W mass, of $-1.5 \pm 1.0 \times 10^{-3}$

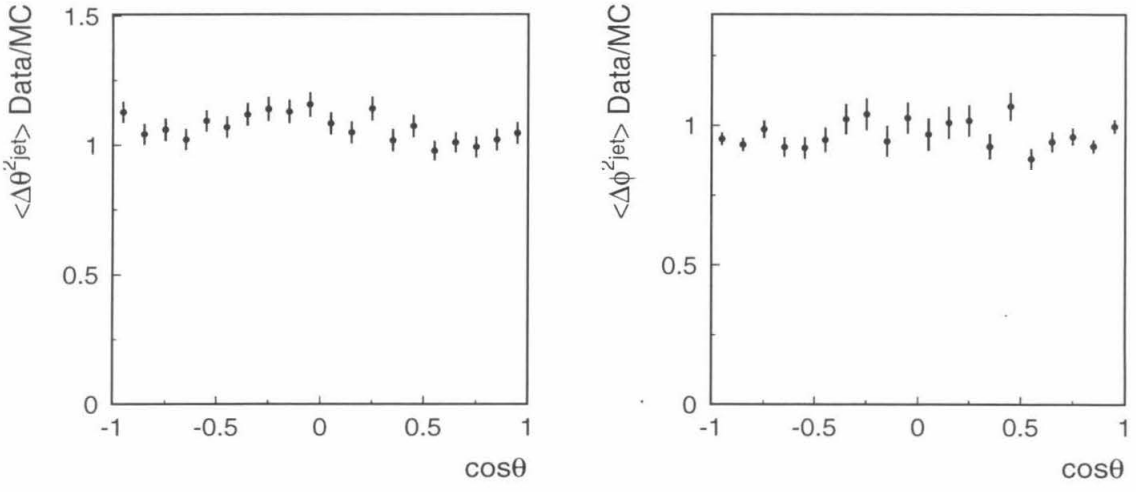

Figure 4.26: Angular dependence of reconstructed jet angle resolutions in $Z^0 \rightarrow q\bar{q}$ events. Ratios of the data and MC distributions for θ and ϕ biases are shown.

pb/GeV, and the W width, of $1.4 \pm 1.0 \times 10^{-3}$ pb/GeV, was convoluted with the current uncertainties of these parameters [23] to give the associated cross section uncertainty of 0.01 pb and 0.01 pb respectively.

Similarly, Monte Carlo events generated at different values of $\sqrt{s}$ were used to determine the influence of the center-of-mass energy uncertainty of the cross section measurement. For all data sets it was found to be negligible, compared to the M_W, Γ_W uncertainties, due to good knowledge of the LEP beam energy.

- KORALW code, used for simulating W^+W^- events, contains only the CC03 subset of $e^+e^- \rightarrow f_1\bar{f}_2f_3\bar{f}_4$ diagrams. Considering Z^0Z^0 four-quark Monte Carlo events as an additional background makes up for most of the deficiency, but still does not take into account the interference between CC03 and the other diagrams. The effect of this simplification was estimated by redoing the cross section fits with W^+W^- events weighted by ratios of the full and CC03 matrix elements, as described in Section 5.4. The change in the fitted cross section of 0.03 pb is taken as the corresponding systematic error.

- It was checked that the selection procedure is not sensitive to the presence of ISR photons in W^+W^- events. The signal Monte Carlo events were put in one of two samples, ISR-enriched and ISR-depleted, depending on whether ISR photons with an energy of at least 8 GeV were found in the list of generated particles. The ISR-enriched sample selected this way constitutes 10% of selected W^+W^- events. The difference of the efficiencies of the neural network selection, evaluated on the two samples, was found to be $0.1 \pm 0.3\%$. This small difference, together with the high theoretical precision of the ISR implementation in the MC, allows me to safely neglect this systematic error.

- Also the measured cross section was shown to be insensitive to the fraction of five-or-more jet events in the signal. Simulation of such events, done with parton shower methods, might be imperfect. I compute the Durham parameter y_{45} as described in Subsection 4.5.1. This quantity is expected to be larger for events with at least five well-defined jets than for four-or-less jet events. A five-jet-enriched sample was constructed by selecting W^+W^- Monte Carlo events with the value of y_{45} larger than 0.008, about 12% of the total sample of $W^+W^- \rightarrow q\bar{q}q\bar{q}$ events. The efficiencies of the selection, evaluated on this sample and the rest of W^+W^- MC events, agreed to $0.4 \pm 0.3\%$. Therefore, I take 0.004 pb as an estimate of the corresponding systematic error on the measured four-jet cross section.

- No precision calculations are available for the non-perturbative process of hadronization. Various phenomenological models have to be used to simulate fragmentation of the four-quark system and the following hadron decays. There are subtle differences in the models' predictions of various properties of the resulting hadronic system. Some of those properties, e.g., charged and neutral multiplicity, or electromagnetic energy fraction, affect the reconstructed jet parameters I use in my selection. This results in an uncertainty of my measurement due to the modeling of fragmentation and hadron decays. I compare the JETSET/LUND and HERWIG [85] models to estimate this uncertainty. Both

models give an adequate description of low energy $q\overline{q}$ event properties [63] and it is not possible to discriminate against one of them on the basis of disagreement with data. I redo the cross section fit using a W^+W^- MC sample obtained by HERWIG hadronization of four-quark systems generated with KORALW. I compare the result with the base one, obtained with a JETSET and KORALW W^+W^- Monte Carlo. I assign the found difference, 0.10 pb, to the systematic error due to fragmentation modeling.

- Bose-Einstein correlation is an enhancement in the two-particle correlation function for identical bosons at small distances, experimentally observed in multihadron events [86, 87]. The effect, similar to Hanbury-Twiss interference [88], is due to the symmetry of the multiboson production amplitudes. This purely quantum mechanical phenomenon has not been incorporated in currently available probabilistic Monte Carlo models of parton showering and string fragmentation. Therefore, ad hoc algorithms have to be applied to the generated multihadron events to reproduce this feature of the data. The LUBOEI algorithm [73] is used in the production of standard L3 MC samples for this purpose. It applies corrections to the momenta of particles belonging to low-invariant-mass identical boson pairs, which could be important for low momentum pions or for pions separated by a small angle. Such corrections change the structure of jets and introduce cross-talk between the two hadronic systems coming from decaying W bosons.

  I repeated the cross section fit using a W^+W^- MC sample generated without applying the algorithm, and I take the difference of the result with respect to the original fit, found to be 0.03 pb, as the uncertainty due to modeling of Bose-Einstein correlation between identical hadrons.

- Another poorly modeled mechanism leading to cross-talk between the two W bosons is due to the interconnection between the two diquark systems during their fragmentation. The typical W boson lifetime, of the order of $1/\Gamma_W \approx 0.1$ fm, is much smaller than the non-perturbative hadronization scale of 1 fm.

Therefore, the hadronization of the two Ws cannot be considered independent. Their overlap is difficult to describe in the framework of currently available fragmentation models. In the language of the string model, in the limit of zero W width Γ_W the fragmentation of an $W^+W^- \rightarrow q_1\overline{q_2}'q_3\overline{q_4}'$ event would proceed through stretching and decay of strings (color flux tubes) binding color singlets $q_1\overline{q_2}'$ and $q_3\overline{q_4}'$. In the case of the large W width, an uncertainty arises due to the inability of the model to predict the probability of an alternative configuration, with the two strings connecting pairs $q_1\overline{q_4}'$ and $q_3\overline{q_2}'$, referred to as color reconnection. Reconnection probabilities, calculated with various models [89, 90, 91, 92] implemented in L3 event generators, vary over a wide range. The probability is difficult to measure experimentally [93]. Moreover, the dependence of the measurement bias on the reconnection probability is different for each color reconnection model. Therefore, a wide range of models has to be considered for estimating the systematic error due to color reconnection. I redid the cross section measurement with W^+W^- Monte Carlos implementing Gustafson-Hakkinen and Sjöstrand-Khoze (types I, II and II′) models of color reconnection in the LUND, HERWIG, and ARIADNE [94] fragmentation frameworks, as well as Monte Carlos with the corresponding fragmentation models with no reconnection allowed. The differences range from -0.01 to 0.03 pb. The shifts are correlated with the reconnnection probabilities predicted by the models. I take the largest of those, corresponding to the Sjöstrand-Khoze I model, as an estimate of the systematic error due to color reconnection.

4.11.3 Modeling of the Backgrounds

- QCD four-jet events constitute the main background for my selection. The events affecting the measurement represent a very small fraction, about 1%, of all $q\overline{q}$ events and their rate and properties may be modeled imperfectly by the parton shower algorithm. While the fit method I use is not sensitive to the total rate of QCD multijet events, a discrepancy in the neural network

output distribution would lead to a bias of the cross section measurement. It is impracticable to study the validity of the parton shower model with the data collected at high energies because of its very limited amount. Therefore, I judge the reliability of the JETSET's description of QCD four-jet events by studying the Z^0 peak data collected by L3. As this data was not used to tune the four-jet rate predicted by JETSET, I believe the quality of the description observed with Z^0 data can be extrapolated to the high energy data I use in my analysis.

To estimate the uncertainty on the cross section, I apply my preselection to a large sample of Z^0 data collected in 1995, and the corresponding Monte Carlo sets, with all energy-scale-dependent parameters reduced by a factor of $M_Z/180$ GeV. I compute y_{34}-dependent correction factors (weights) which have to be applied to 91 GeV $q\overline{q}$ Monte Carlo events to reproduce the y_{34} distribution observed for events selected in the 1995 Z^0 data,

$$w(y_{34}) \;=\; (\frac{dN}{dy_{34}})_{data}/(\frac{dN}{dy_{34}})_{MC}. \tag{4.26}$$

The dependence of the weights on y_{34} is shown in Figure 4.27. I redo the cross section fit with the $q\overline{q}$ Monte Carlo events given weights determined by (4.26), and assign the change in the result, 0.10 pb, to the systematic error due to modeling of QCD background. The reweighting effectively increases the rate of QCD four-jet events which pass the neural network output cut, by about 5%. The result is reproduced when reweighting is done in other variables which reflect the multijet structure of an event, e.g., the neural network output. Also it was checked that the weight function (4.26) computed with 1995 data is consistent with ones obtained with Z^0 data collected during calibration runs in 1996-1998. This indicates that the found data-Monte Carlo disagreement is due to parton shower model deficiencies rather than time-dependent detector miscalibration/mismodeling.

- Distributions of some of the variables used for my selection show differences

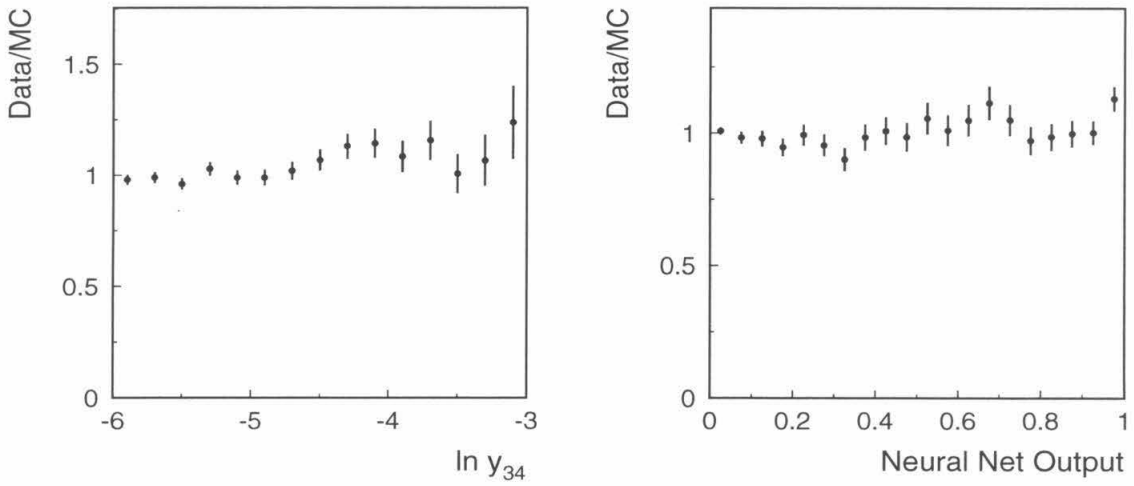

Figure 4.27: The ratio of selected event rates in Z^0 data and MC as a function of y_{34} and neural net output. The combination of data and Monte Carlo statistical errors is shown.

in the background-dominated regions which indicate possible background mismodeling. The most drastic disagreement is found in the distribution of the minimum number of particles in a jet, $\min N_{E>300\ MeV}$ (see Subsection 4.5.2). The excess in the data of events with low-multiplicity jets was also observed with samples of $Z^0 \rightarrow q\overline{q}$ events, and is likely to be due to imperfect modeling of the fragmentation in $e^+e^- \rightarrow q\overline{q}$ events.

The importance of this discrepancy for my measurement was evaluated by redoing the analysis while varying the cut on the minimal jet multiplicity in the [2,6] interval around the default value of 4. This is equivalent to changing the fraction of such mismodeled events in the sample I use for the neural network output fit. The maximal observed cross section shift of 0.08 pb was added in quadrature to the QCD modeling uncertainty evaluated above, to arrive at an estimate of the systematic error due to $q\overline{q}$ background modeling.

- My preselection reduces the rate of accepted $e^+e^- \rightarrow e^+e^-$ hadrons Monte Carlo events by a huge factor of 3×10^6. The accepted cross section is bound to

be unreliable with the properties of two-photon events being poorly modeled by currently available Monte Carlo models. Fortunately, the cross section is very small, and since the accepted events are concentrated at very low values of the neural network output, there is no significant effect on the measured W^+W^- cross section. Changing the Monte Carlo prediction for the accepted $e^+e^- \rightarrow e^+e^-$ hadrons cross section by $\pm 100\%$ changes the fit result by 0.002 pb, which I take as an estimate of the corresponding systematic error. The difference is compatible with the estimate I get by comparing fit results obtained with PYTHIA and PHOJET $e^+e^- \rightarrow e^+e^-$ hadrons Monte Carlo samples.

- The rate of accepted Z^0Z^0 four-jet events has a much greater influence on the fit result, as such events typically have very high values of the neural network output. On the other hand, the cross section and properties of this electroweak process are understood much better. Changing the Monte Carlo prediction for the accepted Z^0Z^0 cross section by $\pm 5\%$ [66] leads to a change of 0.02 pb in the fitted W^+W^- cross section.

4.11.4 Luminosity

- The systematic uncertainty on the integrated luminosity collected by the detector directly translates into an error on the measured cross section. It amounts to 0.2% of the measured cross section at all the energy points I used.

4.11.5 MC Statistics

- I compared results of the measurements obtained with MC event sets used for testing and training the neural network, half of all available Monte Carlo events each, to check the effect of limited Monte Carlo statistics on my measurements. The observed difference, of about 0.1% of the fitted cross section, is in good agreement with binomial expectations given the total and accepted number of Monte Carlo events from various sources. This indicates that the the number of MC events used was sufficient to avoid overtraining of the neural network.

The uncertainty due to limited MC statistics is already implicitly included in the error determined in the maximization of likelihood (4.22) and is not combined with other systematic uncertainties.

4.11.6 Summary of the Systematic Uncertainties

The systematic errors from the sources described above were evaluated for each set of data and Monte Carlo used in my analysis. The values for high-energy (above threshold) data sets are in good agreement with each other. The systematic errors are summarized in Table 4.9.

Source of uncertainty	$\sigma(W^+W^- \to q\bar{q}q\bar{q})$ error [pb] Data period	
	96A	98
Jet energy measurement	0.01	0.04
Jet direction measurement	0.002	0.01
M_W, Γ_W, $\sqrt{s}$ uncertainties	0.01	0.002
CC03 approximation	0.01	0.03
ISR modeling	0	0
FSR modeling	0	0.004
Fragmentation	0.02	0.10
Modeling of BE correlations	0.01	0.03
Modeling of color reconnection	0.01	0.03
$q\bar{q}$ background (QCD modeling)	0.06	0.10
$q\bar{q}$ background (other)	0.02	0.08
$e^+e^- \to e^+e^-$ hadrons background	0	0.002
Z^0Z^0 background cross section	0	0.02
Luminosity	0.002	0.015
MC statistics	0.003	0.01
Total	0.07	0.18

Table 4.9: Systematic errors of the $W^+W^- \to q\bar{q}q\bar{q}$ cross section measurement itemized by the source of the uncertainty. The quadratic sum of all contributions except the error due to finite MC statistics is also given.

The detector miscalibration and W^+W^- mismodeling typically lead to similar errors (relative to the measured cross section) at threshold and at higher energies. Dependence of the selection on the kinematics-affecting parameters M_W, Γ_W, $\sqrt{s}$

is naturally stronger at low energy, but is negligible compared to other systematic uncertainties.

Background modeling errors are dominant at threshold, where the signal-background separation is poor, and are significant at all other energies.

The most important sources of systematic errors are the modeling of hadronization in $W^+W^- \to q\bar{q}q\bar{q}$ events at the higher energies, and the modeling of QCD background at threshold. The systematic errors of the measurements are smaller than the statistical ones even for the highest statistics measurement at $\sqrt{s} = 189$ GeV.

As the same Monte Carlo models and calibration procedures were used throughout my analysis, I assume the systematic uncertainties to be fully correlated when combining results obtained at different $\sqrt{s}$ points.

4.12 Summary of the Results

The measured $W^+W^- \to q\bar{q}q\bar{q}$ cross sections and their statistical and systematic measurements are summarized in Table 4.10. The measured cross sections are in overall agreement with the Standard Model predictions. The statistical error due to limited data statistics is dominant at all energy points considered.

Data Period	$\sigma(W^+W^- \to q\bar{q}q\bar{q})$ [pb]	$\sigma(W^+W^- \to q\bar{q}q\bar{q})_{SM}$ [pb]
96A	$0.85^{+0.43}_{-0.34} \pm 0.07$	1.76
96B	$5.32^{+0.90}_{-0.83} \pm 0.15$	5.67
97	$8.30^{+0.47}_{-0.46} \pm 0.20$	7.17
98	$7.53^{+0.26}_{-0.25} \pm 0.18$	7.59

Table 4.10: The $e^+e^- \to W^+W^- \to q\bar{q}q\bar{q}$ cross sections determined in neural network output fits together with their statistical and systematic errors. The Standard Model cross sections calculated with GENTLE are also given for comparison.

4.12.1 Measurement of the Total W^+W^- Cross Section and the W Branching Ratios

The results of my $W^+W^- \to q\bar{q}q\bar{q}$ cross section measurement can be combined with the studies of other final states [95, 96, 97] to obtain the total W^+W^- production cross sections. Also study of the fractional composition of selected W^+W^- events allows one to make a measurement of the branching ratios of the W boson.

For each L3 data set, dedicated selections were used to select events and measure the W^+W^- cross section in the semileptonic and fully leptonic W^+W^- decay channels ($q\bar{q}e\nu$, $q\bar{q}\mu\nu$, $q\bar{q}\tau\nu$, and six $\ell\nu\ell'\nu'$ final states). The results of the selections were combined with the $W^+W^- \to q\bar{q}q\bar{q}$ cross section measurement in a maximization of the total likelihood

$$\ln L = \sum_{q\bar{q}\ell\nu,\ell\nu\ell'\nu'} (N_i \ln \mu_i - \mu_i) + \ln L_{\mathcal{N}}(\sigma(q\bar{q}q\bar{q})), \tag{4.27}$$

given by the product of Poissonian probabilities of observing the actual number of events found in data N_i, for the $q\bar{q}\ell\nu$ and $\ell\nu\ell\nu$ channels, and the likelihood $L_{\mathcal{N}}(\sigma(q\bar{q}q\bar{q}))$ (see (4.22)) as determined in the neural network output fit of the $W^+W^- \to q\bar{q}q\bar{q}$ cross section. The expectations

$$\mu_i = \mathcal{L}\Big(\sum_{q\bar{q}q\bar{q},q\bar{q}\ell\nu,\ell\nu\ell'\nu'} \varepsilon_{ij}\sigma_j + \sigma_i^{bg} \Big) \tag{4.28}$$

are given by the W^+W^- channel cross sections σ_j to be determined, the matrix ε_{ij} of the efficiencies of selection of final state i to accept events from final state j, and the expected non-W^+W^- backgrounds σ_i. As an example, Tables 4.11 and 4.12 show the efficiency matrix, the expected backgrounds and the number of data events found by the selections used in the analysis of the L3 $\sqrt{s} = 189$ GeV data sample [98].

The W^+W^- channel cross sections σ_j are related to the total $e^+e^- \to W^+W^-$ cross section σ_{WW} and the W decay branching ratios BR($W \to f\bar{f}'$), which are the free

Selection	Efficiencies [%] for									
	$e\nu e\nu$	$e\nu\mu\nu$	$e\nu\tau\nu$	$\mu\nu\mu\nu$	$\mu\nu\tau\nu$	$\tau\nu\tau\nu$	$q\bar{q}e\nu$	$q\bar{q}\mu\nu$	$q\bar{q}\tau\nu$	$q\bar{q}q\bar{q}$
$e^+e^-\to e\nu e\nu$	60.9	0.1	10.3			0.9				
$e^+e^-\to e\nu\mu\nu$		57.4	10.1	0.2	9.4	2.3				
$e^+e^-\to e\nu\tau\nu$	9.4	1.2	39.0		0.2	10.3				
$e^+e^-\to \mu\nu\mu\nu$				49.1	8.7	1.0				
$e^+e^-\to \mu\nu\tau\nu$		4.9	0.5	2.3	33.9	8.2				
$e^+e^-\to \tau\nu\tau\nu$	0.4	0.2	2.8		1.0	23.6				
$e^+e^-\to q\bar{q}e\nu$							87.2	0.3	2.2	
$e^+e^-\to q\bar{q}\mu\nu$							0.3	78.5	4.5	0.1
$e^+e^-\to q\bar{q}\tau\nu$							4.8	5.7	49.3	0.2

Table 4.11: Selection efficiencies for $\ell\nu\ell\nu$, $q\bar{q}\ell\nu$ selections used by L3 at $\sqrt{s}$ = 189 GeV.

parameters of the fit, as

$$\sigma(W^+W^-\to q\bar{q}q\bar{q}) = \sigma_{WW} BR(W\to q\bar{q}')^2 \quad (4.29)$$

$$\sigma(W^+W^-\to q\bar{q}\ell\nu) = 2 f_{q\bar{q}\ell\nu}\sigma_{WW} BR(W\to q\bar{q}') BR(W\to \ell\nu) \quad (4.30)$$

$$\sigma(W^+W^-\to \ell\nu\ell\nu) = f_{\ell\nu\ell\nu}\sigma_{WW} BR(W\to \ell\nu)^2 \quad (4.31)$$

$$\sigma(W^+W^-\to \ell\nu\ell'\nu') = 2 f_{\ell\nu\ell'\nu'}\sigma_{WW} BR(W\to \ell\nu) BR(W\to \ell'\nu'). \quad (4.32)$$

The correction factors f_i, given in Table 4.12, are necessary to correct for the effects of the Feynman diagrams not present in the CC03 set (CC20 for $q\bar{q}e\nu$ and CC/NC56 for $\ell\nu\ell\nu$ final states), to simplify the comparison with the Standard Model predictions and the consequent W mass measurement using the W^+W^- production cross section. The effects of the additional diagrams are negligible and no correction is necessary for $q\bar{q}\mu\nu$, $q\bar{q}\tau\nu$, and $q\bar{q}q\bar{q}$ final states.

The likelihood (4.27) does not take into account possible dependence of the fitted

Selection	N_{data}	Background [pb]	Conversion Factor f
$e^+e^- \to e\nu e\nu$	28	0.014	0.88
$e^+e^- \to e\nu\mu\nu$	41	0.020	1.07
$e^+e^- \to e\nu\tau\nu$	50	0.046	1.07
$e^+e^- \to \mu\nu\mu\nu$	15	0.029	0.96
$e^+e^- \to \mu\nu\tau\nu$	36	0.018	1.10
$e^+e^- \to \tau\nu\tau\nu$	16	0.030	0.96
$e^+e^- \to q\bar{q}e\nu$	358	0.105	1.08
$e^+e^- \to q\bar{q}\mu\nu$	364	0.083	—
$e^+e^- \to q\bar{q}\tau\nu$	313	0.240	—

Table 4.12: Number of selected data events, N_{data}, and expected non-W^+W^- background cross section for $\ell\nu\ell\nu$, $q\bar{q}\ell\nu$ selections used by L3 at $\sqrt{s} = 189$ GeV. The ratio of the CC03 cross section without cuts and the four-fermion cross section within phase-space cuts, calculated with EXCALIBUR, is listed in the last column.

$W^+W^- \to q\bar{q}q\bar{q}$ cross section on the $W^+W^- \to q\bar{q}\ell\nu$ cross sections, fixed to the Standard Model values during the neural network output distribution fit. This dependence is expected to be very small because of very low $q\bar{q}q\bar{q}$ preselection efficiency for $q\bar{q}\ell\nu$ events and the large difference of the $\mathcal{N}$ distribution for them and $W^+W^- \to q\bar{q}q\bar{q}$ events. The largest cross-efficiency, $\frac{d\sigma(W^+W^- \to q\bar{q}q\bar{q})}{d\sigma_{MC}(q\bar{q}\tau\nu)}$ has been numerically determined to be in the 0.2-0.4% range for all energies considered and was neglected.

In addition, one can demand the equality of the leptonic branching ratios BR($W \to \ell\nu$) used in the fit, in the hypothesis of charged current lepton universality. Fits with and without this assumption were performed using all high energy L3 data collected in 1996-1998. The resulting values of the W^+W^- cross section at each energy and W decay branching ratios are reported in Table 4.13. The systematic errors were obtained by propagating the systematic errors on individual W^+W^- channel cross sections, taking into account their correlations. With the currently available statistics,

the statistical errors are dominant for all the measurements.

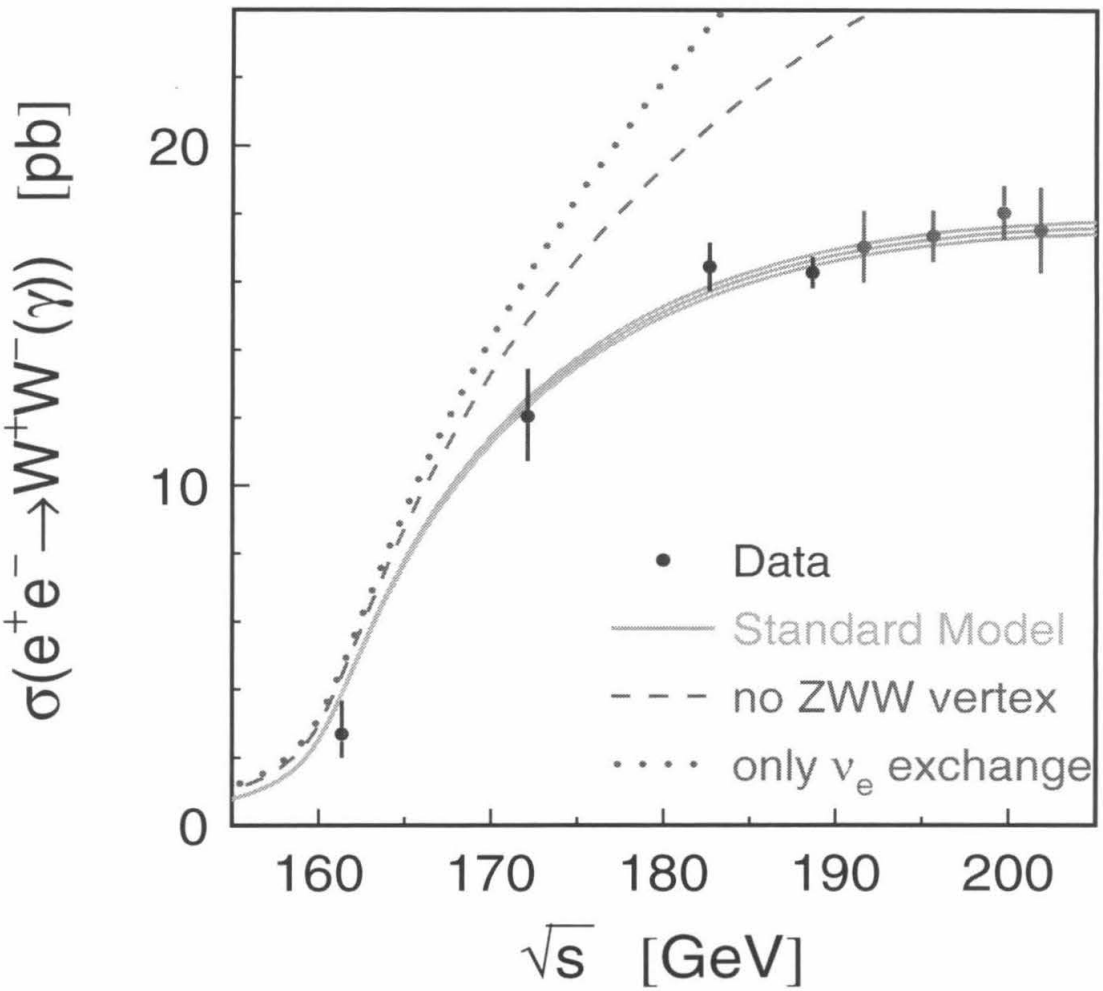

Figure 4.28: The cross section of the process $e^+e^- \to W^+W^- \to f_1\bar{f}_2f_3\bar{f}_4$ as a function of the centre-of-mass energy. The measurements of σ_{WW} are shown as dots with error bars, combining statistical and systematic errors in quadrature. The points at energies higher than 189 GeV are preliminary L3 measurements. The solid curves show the Standard Model expectation and its theoretical uncertainty. The dashed curve shows the expectation if there is no ZWW coupling. The dotted curve shows the expectation if only t-channel ν_e exchange in W pair production is considered.

	Lepton Non-Universality	Lepton Universality	Standard Model
BR(W$\to$eν) [%]	$10.27 \pm 0.44 \pm 0.17$	—	
BR(W$\to\mu\nu$) [%]	$10.00 \pm 0.46 \pm 0.17$	—	
BR(W$\to\tau\nu$) [%]	$11.16 \pm 0.63 \pm 0.25$	—	
BR(W$\to\ell\nu$) [%]	—	$10.43 \pm 0.23 \pm 0.13$	10.83
BR(W$\to$q$\overline{\text{q}}'$) [%]	$68.57 \pm 0.69 \pm 0.38$	$68.72 \pm 0.69 \pm 0.38$	67.51
$\sigma_{WW}(\sqrt{s} = 161.34$ GeV) [pb]	$2.70^{+0.99}_{-0.68} \pm 0.14$	$2.68^{+0.98}_{-0.67} \pm 0.14$	—
$\sigma_{WW}(\sqrt{s} = 172.13$ GeV) [pb]	$12.10^{+1.39}_{-1.30} \pm 0.23$	$12.04^{+1.38}_{-1.29} \pm 0.23$	12.43
$\sigma_{WW}(\sqrt{s} = 182.68$ GeV) [pb]	$16.52 \pm 0.68 \pm 0.26$	$16.45 \pm 0.67 \pm 0.26$	15.72
$\sigma_{WW}(\sqrt{s} = 188.64$ GeV) [pb]	$16.36 \pm 0.39 \pm 0.26$	$16.28 \pm 0.38 \pm 0.26$	16.65

Table 4.13: Measured W decay branching ratios, and total W^+W^- cross sections at different energies, derived with and without the assumption of charged current lepton universality. The correlations between the leptonic branching fractions are -0.008, -0.272, -0.286 for $(e\mu)$, $(e\tau)$, $(\mu\tau)$, respectively. Also shown are the W decay branching fractions and the total W^+W^- cross section as expected in the Standard Model.

The measured values of the W branching ratios for different lepton families are in agreement with each other and with the Standard Model expectations [99], and support the lepton universality hypothesis. The energy dependence of the W^+W^- production cross section, shown in Figure 4.28, also agrees well with the Standard Model and conforms to the SM picture of gauge cancellations between t and s-channel $e^+e^- \to W^+W^-$ diagrams. The branching ratio results represent a significant improvement over previous measurements at Fermilab [23], while the measurement of the $e^+e^- \to W^+W^-$ cross section only became possible with the advent of LEP 2.

4.12.2 Measurement of the $|V_{cs}|$ Matrix Element

The fraction of W bosons decaying into hadrons is determined by the sum of squared Cabibbo-Kobayashi-Maskawa matrix elements over all kinematically allowed quark

pairs,

$$\frac{BR(\mathrm{W}\to \mathrm{q}\overline{\mathrm{q}}')}{BR(\mathrm{W}\to \ell\nu)} = (1+\frac{\alpha_S(\mathrm{M_W})}{\pi}) \sum_{i=u,c;j=d,s,b} |V_{ij}|^2. \quad (4.33)$$

Consequently, my branching ratios measurement puts a constraint on the elements of the CKM matrix

$$\sum_{i=u,c;j=d,s,b} |V_{ij}|^2 = 2.115 \pm 0.068(stat.) \pm 0.038(syst.). \quad (4.34)$$

This constraint can be interpreted as a measurement of a CKM matrix element. The sensitivity is greatest for the diagonal elements V_{ud} and V_{cs}. The V_{cs} matrix element is difficult to measure directly and is the more poorly known of the two. I find it to be

$$|V_{cs}| = 1.033 \pm 0.033(stat.) \pm 0.018(syst.), \quad (4.35)$$

where the statitstical error includes the errors on α_S and the other V_{ij}, but is dominated by the statistical error on the W branching ratios. The measurement has significantly larger sensitivity than other methods of measuring V_{cs} not relying on the unitarity of the CKM matrix.

4.12.3 Limits on the Invisible Decays of the W

Our measurement of the total $\mathrm{W^+W^-}$ cross section assumes that all Ws decay into known fermion doublets and can be detected.

This is not the case in some extensions of the Standard Model. For example, some R-parity conserving supersymmetric theories [44, 45] predict a W decay into a chargino-neutralino pair, with the subsequent decay of the chargino, $\mathrm{W}^\pm \to \chi^0\chi^\pm \to \chi^0\chi^0\ell^\pm$. In the region of SUSY parameter space, especially difficult for direct searches, where the chargino-neutralino mass difference is small, $m_{\chi^0} \leq m_{\chi^\pm}$, and the neutralino is the lightest supersymmetric particle (LSP), such decays would produce no

detectable particles besides the low energy lepton and would be virtually invisible. W^+W^- events in which at least one W decay was of this kind, would be rejected by the standard W^+W^- channel selections. This would lead to a systematic deviation of the apparent W^+W^- cross section from the Standard Model prediction

$$\frac{\sigma_{WW}^{measured}}{\sigma_{WW}^{SM}} \simeq (\frac{\Gamma_{\rm W}^{SM}}{\Gamma_{\rm W}^{SM}+\Gamma_{\rm W}^{invisible}})^2, \tag{4.36}$$

where $\Gamma_{\rm W}^{invisible}$ is the W width corresponding to such invisible decays. Additionally, W^+W^- events with exactly one W decay unobservable would contribute to the measured cross section of single-resonant W production $e^+e^-\rightarrow We\nu$ as

$$\sigma_{We\nu}^{measured} \simeq \sigma_{We\nu}^{SM} + \frac{2\Gamma_{\rm W}^{invisible}\Gamma_{\rm W}^{SM}}{(\Gamma_{\rm W}^{SM}+\Gamma_{\rm W}^{invisible})^2}\sigma_{WW}^{SM}, \tag{4.37}$$

provided the selection efficiency for them is the same as for genuine $We\nu$ events. Absence of significant deviations from the Standard Model cross section predictions for either W^+W^- or single W production [100] allows me to put a limit on the invisible W width

$$\Gamma_{\rm W}^{invisible} < 17 \text{ MeV} \tag{4.38}$$

at 95% confidence level, taking into account the systematic errors of both the W^+W^- and the single W production measurements.

Chapter 5

Measurement of the W Mass and Width

The sample of L3 data I obtained, using the selection procedure described above, is enriched in $W^+W^- \rightarrow q\bar{q}q\bar{q}$ events, and this allows me to make precision measurements of the mass and the width of the W boson. Three methods have been used at LEP 2 for this purpose [101]. The first one, described in detail in Sections 5.1 and 5.2, exploits the strong dependence of the W^+W^- cross section in the threshold region $\sqrt{s} \approx 2M_W$, on the W mass M_W. Due to this dependence, the value of the threshold cross section reported in Section 4.12 can be used to give an estimate of the W mass. The rest of the chapter is devoted to the second, the most statistically powerful method of measuring M_W and Γ_W, which relies on the direct reconstruction of the invariant masses of the produced W bosons, by methods described in the previous chapter. The shape of the reconstructed mass distribution is sensitive to and can be used to measure the W boson mass and width with great accuracy.

In this chapter I describe the invariant mass reconstruction aspects of this measurement, as well as the statistical methods of estimating M_W given the reconstructed invariant mass distribution. The results of applying these methods to the selected L3 event samples and an analysis of the systematic uncertainties of the measurement are also presented.

The third method of measuring M_W employs the fact that in the relatively low W boost regime at LEP2, the energy of the fermions produced, $\frac{M_W}{2}$ in the W rest frame, lies in a relatively narrow window around $\frac{\sqrt{s}}{4}$ in the laboratory frame

$$\frac{\sqrt{s}}{4}(1 - \sqrt{1 - \frac{4M_W^2}{s}}) < \quad E_f \quad < \frac{\sqrt{s}}{4}(1 + \sqrt{1 - \frac{4M_W^2}{s}}). \tag{5.1}$$

The distribution is sensitive to M_W and can be studied for all flavors of leptons in both $W^+W^- \to q\bar{q}\ell\nu$ and $W^+W^- \to \ell\nu\ell\nu$ events [102]. Excellent lepton energy resolution is crucial for this measurement. The method is not practicable for $W^+W^- \to q\bar{q}q\bar{q}$ events because of the much larger experimental errors of jet energy measurement, and is not considered in this thesis.

The data collected by L3 at $\sqrt{s}$ of 189 GeV, together with Monte Carlo sets generated at this energy, is used for data-Monte Carlo comparisons in this chapter as the most statistically significant dataset used in my analysis, except where indicated otherwise.

5.1 Threshold Cross Section Fit

The energy dependence of the W^+W^- production cross section in the threshold region is mainly determined by the 2-body Lorentz invariant phase space available to the two W bosons,

$$\sigma(\sqrt{s}, M_W) \sim \frac{1}{s}\sqrt{1 - \frac{4M_W^2}{s}}, \tag{5.2}$$

in the zero W width limit. This leads to a sharp rise in the cross section at values of $\sqrt{s}$ around $\approx 2M_W$ as the center-of-mass energy increases. Similarly, the cross section at a fixed $\sqrt{s}$ in this energy region exhibits a strong dependence on M_W. A series of cross section curves $\sigma_{W^+W^-}(\sqrt{s})$ for different values of M_W is shown in Figure 5.1. The actual non-negligible W width and initial state radiation decrease the dependence somewhat, but the resulting sensitivity still allows one to transform a measurement of the W^+W^- cross section into a precise measurement of the W mass, given a Standard Model calculation of $\sigma_{W^+W^-}(\sqrt{s}, M_W)$.

The W mass is determined by maximizing the likelihood (4.27), computed with the 96A data, with the W branching ratios set to their Standard Model expectations, and the total W^+W^- cross section replaced by the M_W-dependent Standard Model prediction. The much larger data samples collected at higher energies do not

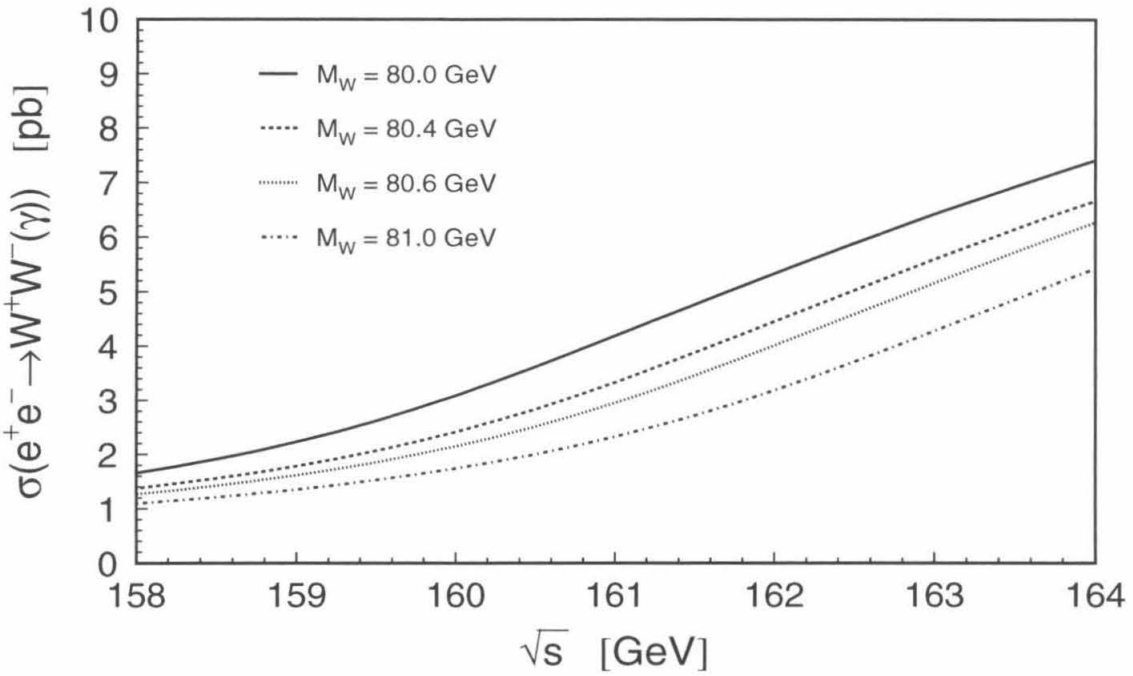

Figure 5.1: W^+W^- cross section in the threshold region, computed with GENTLE. Curves corresponding to different values of M_W are given.

contribute to and were not used for the measurement, as the W^+W^- cross section at higher energies is much less dependent on M_W. The SM cross section was calculated by the GENTLE [65] semianalytical code, implementing the CC03 subset of the $e^+e^- \to f_1\bar{f}_2f_3\bar{f}_4$ Feynman diagrams, at the average center-of-mass energy of the 96A data period $\langle\sqrt{s}\rangle = 161.34$ GeV. The cross section prediction as a function of the W mass, together with the threshold cross section and mass measurements, is shown in Figure 5.2.

The fit gives

$$M_W = 80.94^{+0.50}_{-0.48}\ \text{GeV}, \tag{5.3}$$

where the errors are statistical and correspond to a decrease of the likelihood of 0.5

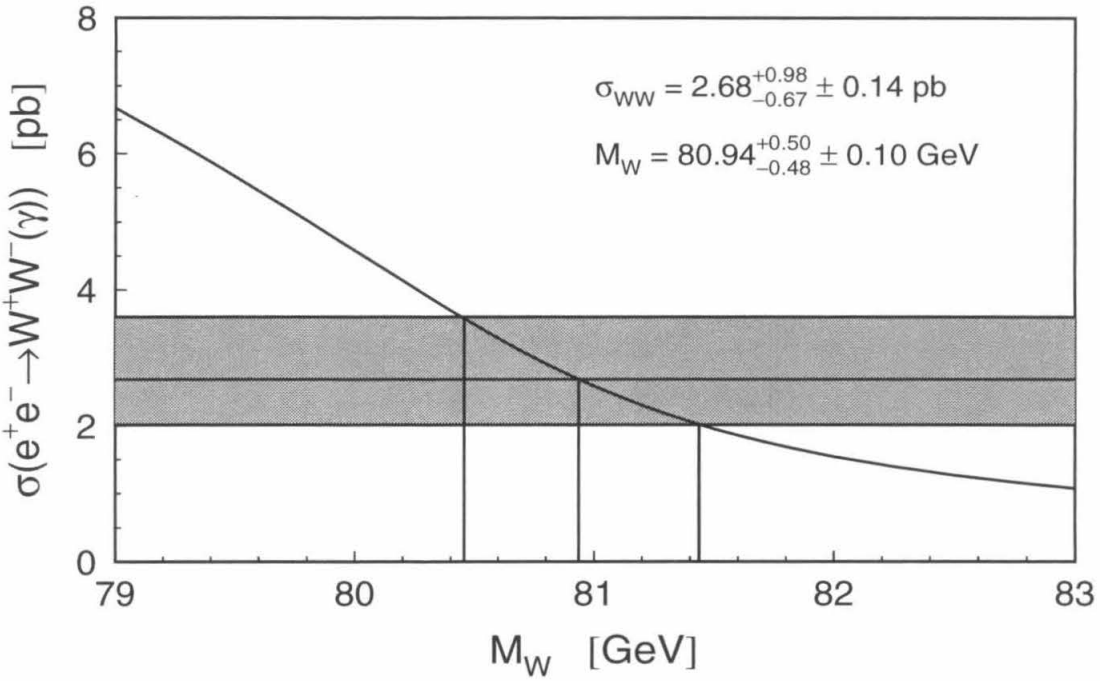

Figure 5.2: W^+W^- cross section at $\sqrt{s} = 161.34$ GeV as a function of M_W. The horizontal and vertical bands indicate my measurements of $\sigma(e^+e^- \to W^+W^-)$ and M_W respectively.

relative to the maximal value. The next section discusses the systematic errors of this measurement.

5.2 Threshold Measurement Uncertainties

There are two sources of systematic errors for this measurement. The first one is the systematic uncertainty of the cross section measurement proper. It contributes an error on the measured W mass of

$$\Delta M_W = \mu \Delta_{syst} \sigma(e^+e^- \to W^+W^-), \tag{5.4}$$

where

$$\mu \equiv |\frac{d\sigma(e^+e^- \rightarrow W^+W^-)}{dM_W}(\sqrt{s}, M_W^{measured})|^{-1} = 630 \text{ MeV/pb} \quad (5.5)$$

is the inverse of the slope of the cross section curve in Figure 5.2, used to convert W^+W^- cross section uncertainties into M_W ones. This error was evaluated to be 88 MeV and turns out to be the dominant one for this method of measuring M_W.

Other systematic errors are due to the uncertainties implicit in the Standard Model calculation. When interpreting the measured cross section in terms of M_W, they translate into the W mass errors with the constant factor μ.

- The W^+W^- cross section depends strongly on $\sqrt{s}$, so any uncertainty on the LEP beam energy directly translates into an error on the measured M_W of

$$\Delta M_W = \mu|\frac{d\sigma(e^+e^- \rightarrow W^+W^-)}{d\sqrt{s}}|\Delta\sqrt{s} \approx \Delta E_{\text{beam}}. \quad (5.6)$$

  This corresponds to an error of 27 MeV for the 96A data period.

- The W width is another parameter the cross section depends on. Fortunately, its current knowledge $\Gamma_W = 2.06 \pm 0.06$ GeV [23] is precise enough to make the corresponding systematic error

$$\Delta M_W = \mu|\frac{d\sigma(e^+e^- \rightarrow W^+W^-)}{d\Gamma_W}|\Delta\Gamma_W \quad (5.7)$$

  negligible compared to ones from other sources.

- Higher-order radiative corrections neglected in the $e^+e^- \rightarrow W^+W^-$ cross section calculations I rely on are assumed to be of the order of $(\frac{\Delta\sigma}{\sigma})_{rad.cor.} \approx 2\%$ at the threshold [29]. The resulting uncertainty in the fitted M_W is

$$\Delta M_W = \mu\sigma(e^+e^- \rightarrow W^+W^-)(\frac{\Delta\sigma}{\sigma})_{rad.cor.}, \quad (5.8)$$

  which corresponds to an error of 34 MeV.

For the statistics of the L3 96A data sample, all the systematic errors of the measurement are much smaller than the statistical one. Including the systematic errors added in quadrature, the result of the threshold cross section measurement of M_W is

$$M_W = 80.94^{+0.50}_{-0.48}(stat.) \pm 0.10(syst.) \text{ GeV}. \quad (5.9)$$

The result is in agreement with the Standard Model expectation and other M_W measurements [23].

This determination of the W mass is based on the assumption that the Standard Model describes correctly the $e^+e^- \rightarrow W^+W^-$ cross section. This qualification is eliminated and the statistical precision of the measurement is greatly improved by the direct reconstruction method applied to the L3 data collected at higher energies, as described in the following sections.

5.3 W Invariant Mass Spectrum Reconstruction

The bulk of the W^+W^- pairs collected by L3 were produced at energies significantly above the threshold. At those energies, the $e^+e^- \rightarrow W^+W^-$ cross section is not sensitive to M_W, but the increased event rate and decreasing importance of phase space effects make it possible to measure M_W studying the resonant shape of the produced W bosons' invariant mass distribution.

Above the threshold, the invariant mass spectrum of the produced W bosons is mostly determined by the W propagators in the $e^+e^- \rightarrow W^+W^-$ matrix element,

$$\frac{d\sigma(e^+e^- \rightarrow W^+W^-)}{dm_1 dm_2} \sim \prod_{j=1,2} \frac{1}{|m_j^2 - M_W^2 + iM_W\Gamma_W|^2}. \quad (5.10)$$

Phase space and radiative corrections and selection and reconstruction effects distort the Breit-Wigner distribution. Nevertheless the prominent invariant mass peak allows one to measure with great accuracy the W mass, which defines its position, and the

W width, which is related to its broadness.

Directly at the threshold the W resonance is severely deformed by the phase space factor, which, together with the low W^+W^- cross section, makes the data collected at 161 GeV of little use in the direct reconstruction measurement. Only the 96B, 97, and 98 data sets were considered in the subsequent analysis.

5.3.1 Direct W Invariant Mass Reconstruction

Different estimators of the W invariant mass could be chosen to construct the spectrum to be analyzed. I find that the average W mass m^{5C} obtained with the 5C kinematic fit, as described in Subsection 4.5.3, is the best for this purpose. No improvement in the expected W mass error was found when the whole analysis was repeated with alternative W mass estimators (W masses obtained with 4C kinematic fits, or rescaled 4C-fitted masses [103], or 2D generalizations of the above).

5.3.2 Jet Combination Algorithm

Another ambiguity in the construction of the spectrum is the choice of the jet combinations to be used for the fit. I chose the $\Sigma'm$ (Δm) algorithms for the $W^+W^- \rightarrow q\bar{q}q\bar{q}$ cross section measurement at 161, 172 (183, 189) GeV, because they gave the highest rate of correct assignment of jets to primary W bosons (see Subsection 4.5.4). This decision has to be reconsidered for the mass measurement. Even the most efficient pairing algorithms has significant (~25%) misassignment probability at all energies. The mass spectrum contribution from the incorrect combinations constitutes a kind of irreducible background, possibly M_W-dependent, which might have a significant effect on the accuracy of the measurement. For that reason, the criterion of the maximal correct combination probability has to be complemented by an attempt to minimize the overlap of the invariant mass distributions for correct and incorrect jet combinations.

Repeating the mass measurement using various jet combination schemes, I found the χ^2 algorithm to provide the best compromise between these requirements, re-

sulting in the smaller expected statistical error of the mass measurement. As shown in Figure 5.3(a), with the χ^2 algorithm, the incorrect combinations form a flat distribution covering a wide range of masses. The overlap with the mass peak given by the correct combinations is much larger for the more efficient Δm algorithm (see Figure 5.3(c)).

In about 40% of $W^+W^- \rightarrow q\bar{q}q\bar{q}$ events the correct jet combination is not found by the χ^2 algorithm. One could try to recover these events for the W mass fit by considering the combinations with the second-highest $P_{\chi^2}({\chi^2}_{5C}; 5)$ as well, approximately 25% of which map correctly onto the underlying W bosons. The m^{5C} distribution for the second-best $P_{\chi^2}({\chi^2}_{5C}; 5)$ combinations for the selected $q\bar{q}q\bar{q}$ events is shown in Figure 5.3(b). The distribution has an acceptable signal-to-background ratio in the peak region and can be used in the mass fit. The combinations with the worst $P_{\chi^2}({\chi^2}_{5C}; 5)$ are seldom the right ones and are not useful for the measurement.

5.3.3 Event Quality Requirements

With the exception of a small fraction of badly reconstructed events with low values of the $P_{\chi^2}({\chi^2}_{5C}; 5)$ probability, most of the $W^+W^- \rightarrow q\bar{q}q\bar{q}$ events, in which the right jet combination was found, lie in the flat part of the kinematic fit probability distribution. This is not the case for the incorrect combinations or for the background events, for which the equal mass assumption is not correct and which typically have low kinematic fit probabilities, as shown in Figure 5.4.

The expected error of the mass measurement was found to decrease after jet combinations with the fit probability of less than 5% were removed from the fit. Those are dominated by incorrect combinations which contain no information about the W mass. Removing them leads to a reduction of the background and increase of the signal-to-background ratio in the mass peak. The improvement is especially large for the second-best combinations. More than 70% of the best combinations and only 25% of the second-best combinations in genuine $W^+W^- \rightarrow q\bar{q}q\bar{q}$ events survive the probability cut and are used in the W mass fit. The results of applying the probability

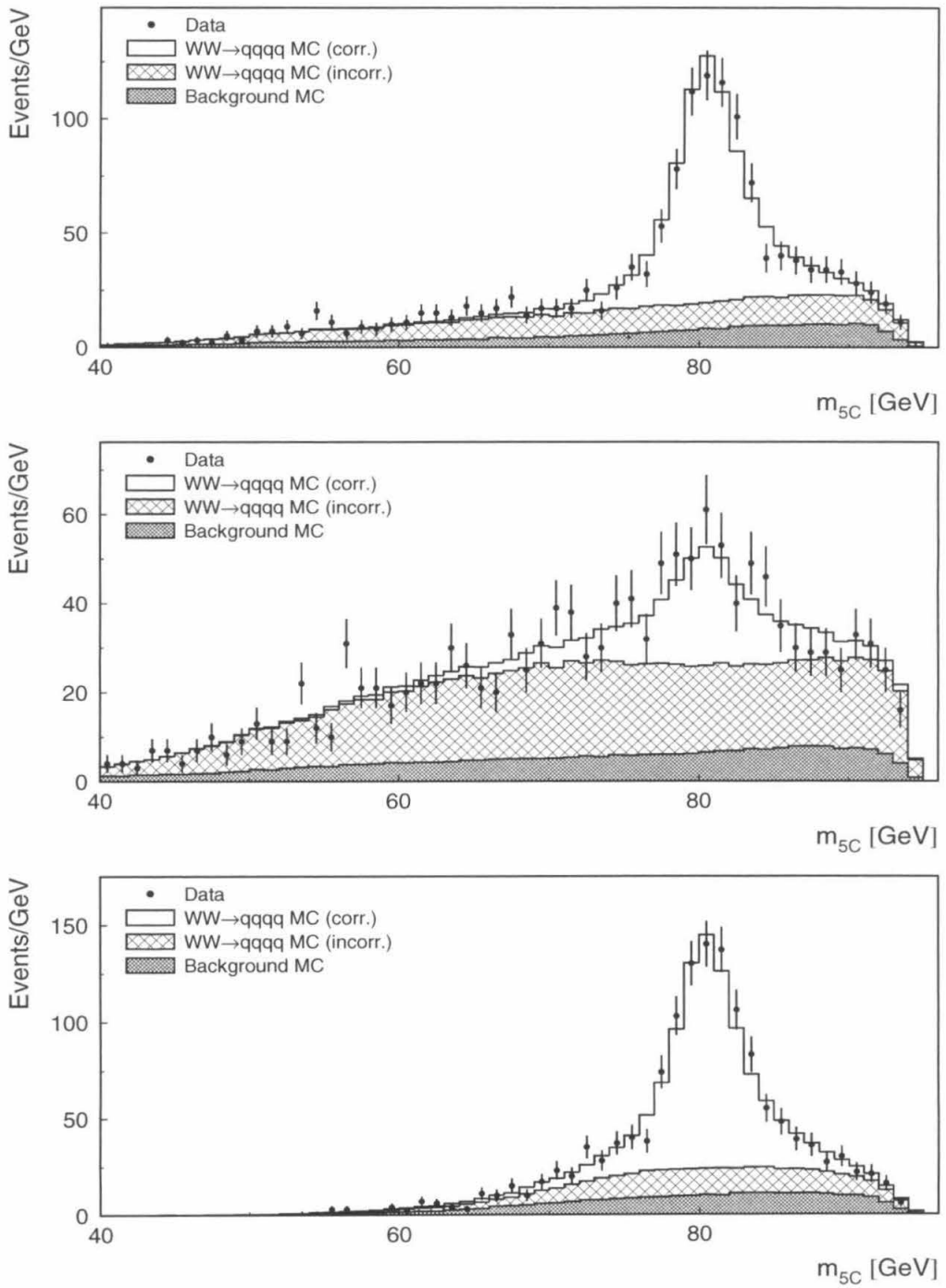

Figure 5.3: The m^{5C} distribution for (a) the best $P_{\chi^2}(\chi^2{}_{5C}; 5)$ combination, (b) the second-best $P_{\chi^2}(\chi^2{}_{5C}; 5)$ combination, and (c) the combination found with the Δm algorithm, for selected $W^+W^- \to q\bar{q}q\bar{q}$ candidates. Correct and incorrect jet combinations are shown separately.

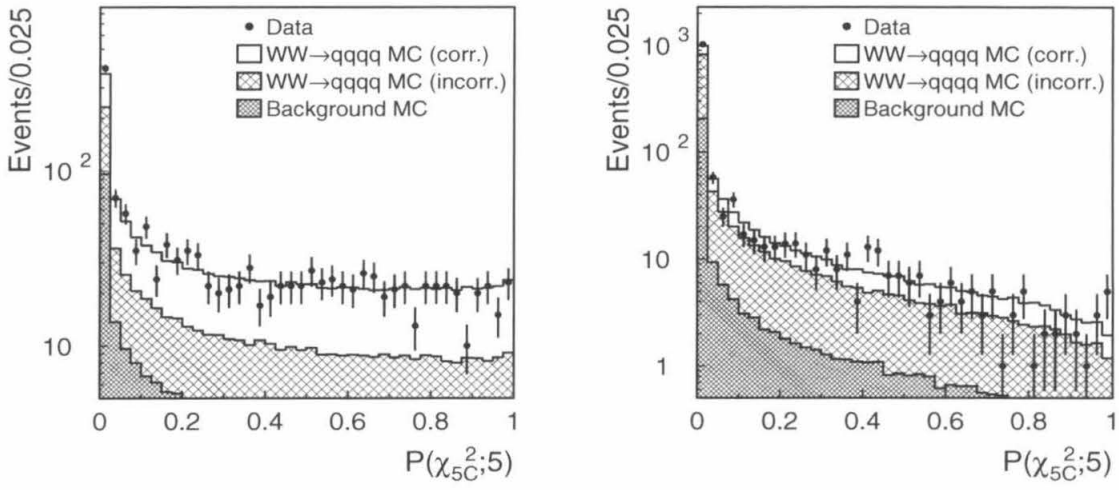

Figure 5.4: Distributions of the 5C kinematic fit probability $P_{\chi^2}(\chi^2{}_{5C};5)$ for the best (a), and second-best (b) jet combinations in the selected $W^+W^- \rightarrow q\bar{q}q\bar{q}$ candidates.

cut to the L3 data samples, selected by the neural network selection described in Section 4.8, are summarized in Table 5.1. The expected and observed ratios of selected events are in good agreement at all energies considered. The reconstructed invariant mass distributions for the events selected at different energies are shown in Figure 5.5. These distributions are used in the W mass fit described in the following sections.

	Data Period		
	96B	97	98
N_{total}	57	468	1393
$N(P_1 > 0.05)$	39	333	935
$N_{exp}(P_1 > 0.05)$	44 ± 7	289 ± 17	949 ± 31
$N(P_2 > 0.05)$	2	51	142
$N_{exp}(P_2 > 0.05)$	6 ± 2	40 ± 6	135 ± 12

Table 5.1: Number of jet combinations selected in $W^+W^- \rightarrow q\bar{q}q\bar{q}$ candidates in data, together with SM Monte Carlo expectations. Also given is the standard deviation on the total number of selected combinations expected in the SM.

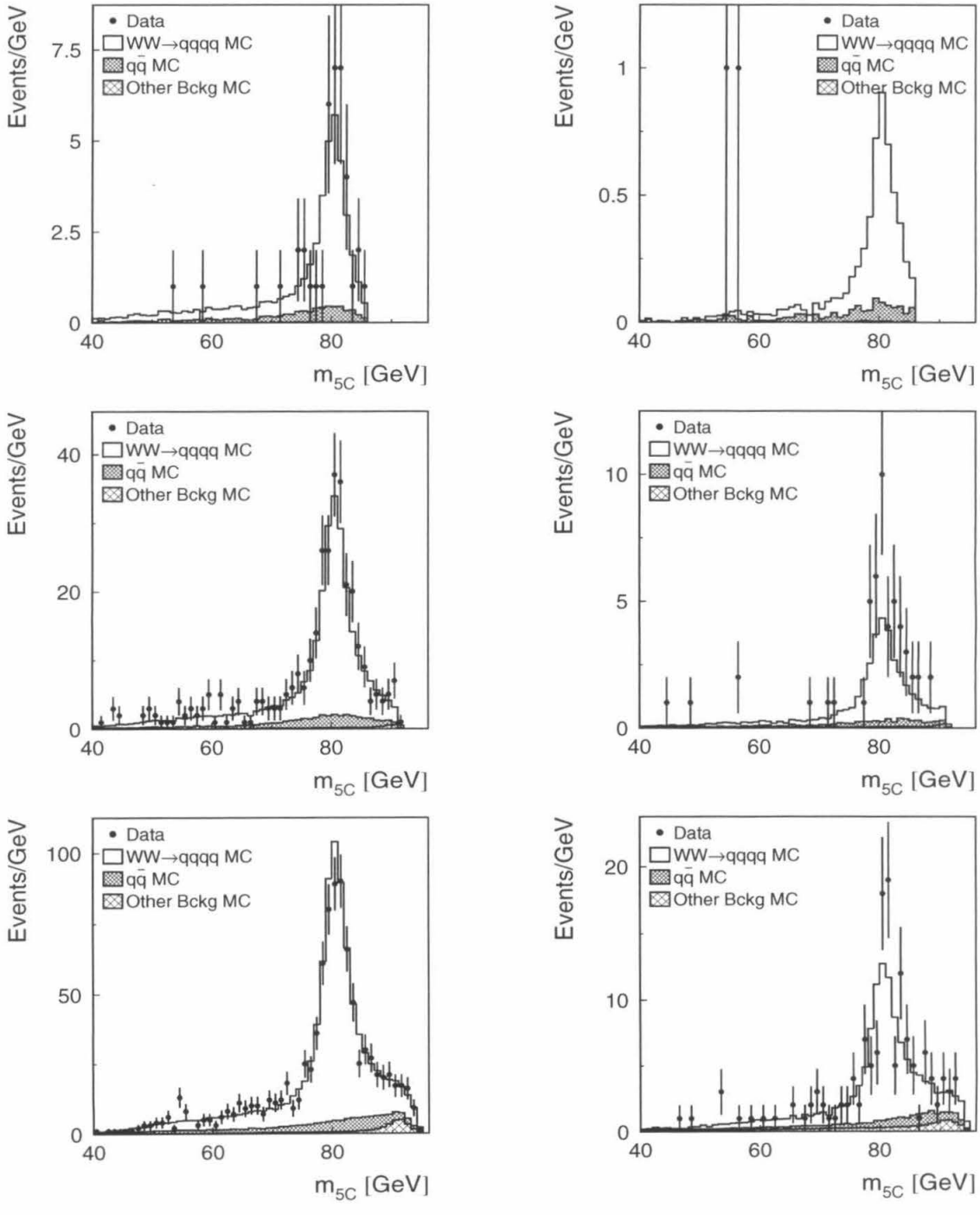

Figure 5.5: Reconstructed m^{5C} invariant mass distributions for the best (a,c,e) and second-best (b,d,f) $P_{\chi^2}(\chi^2_{5C}; 5)$ combinations selected in 96B, 97 and 98 data.

5.4 Monte Carlo Reweighting Method

A straightforward approach to estimate M_W, given the reconstructed invariant mass spectra, would be to compare the distribution observed in data with those obtained by Monte Carlo simulations at different (continuous) values of M_W and choose the W mass value maximizing the likelihood of observing the data with the m^{5C}-dependent probability density given by the Monte Carlo prediction. This approach is not feasible, considering the large amounts of Monte Carlo events necessary for this measurement, but one can obtain Monte Carlo predictions for any value of M_W by using a reweighted Monte Carlo.

To each event i in a W^+W^- Monte Carlo event sample generated with the W mass set to M_W^{MC}, I assign a weight

$$w_i(M_W) = \frac{|\mathcal{M}(M_W, p_i^1, p_i^2, p_i^3, p_i^4)|^2}{|\mathcal{M}(M_W^{MC}, p_i^1, p_i^2, p_i^3, p_i^4)|^2}, \tag{5.11}$$

where p_i^j is the four-momentum of the jth outgoing fermion in event i, and $\mathcal{M}(M_W, p_i^1, p_i^2, p_i^3, p_i^4)$ is the $e^+e^- \to f_1\bar{f}_2f_3\bar{f}_4$ matrix element. In the limit of infinite number of Monte Carlo events, differential cross sections corresponding to a new value of the W mass M_W will be approximated by the reweighted density of the Monte Carlo sample generated at M_W^{MC}.

Many other factors, besides the Born-level matrix element, contribute to the total event weight which determines an event's acceptance or rejection in von Neumann's scheme, such as phase space, initial and final state radiation, and hadronization. None of these additional factors depends on M_W though, which is the basis of the validity of the reweighting method.

This method of extrapolating Monte Carlo predictions as a function of M_W can be straightforwardly generalized to other W boson parameters which affect the $e^+e^- \to W^+W^-$ matrix element, such as the W width Γ_W and $W^+W^-\gamma/Z^0$ couplings. Extrapolation in more than one parameter simultaneously, e.g., M_W and Γ_W, is also feasible with this approach. The reweighting method will be the basis of the measurements

of W boson parameters presented here and in Chapter 6.

The EXCALIBUR [74] implementation of the four-fermion matrix element I use for reweighting, allows me to vary the W mass and width as well as a wide range of $W^+W^-\gamma/Z^0$ couplings used in the calculation of the matrix elements. It also provides a choice of the subset of Feynman diagrams used in the calculation. The fits described in the chapter were performed using the CC03 set, the same one used for generating the W^+W^- Monte Carlo events I used. The uncertainty in the mass determination due to this simplification is addressed in Section 5.6.

Attention should be paid to an important numerical feature of the method. The fluctuations in the fitted value of M_W due to finite Monte Carlo statistics are controlled by the effective number of events $N_{MC}^{eff} = (\sum w_i)^2 / \sum w_i^2$. This number depends on M_W and falls quickly as M_W gets further away from M_W^{gen}. This could lead to increased errors due to finite MC statistics and, more importantly, to M_W-dependent biases (nonlinearity) of the fits based on the reweighted Monte Carlo. I try to reduce these effects by using very large baseline Monte Carlo samples, and by using mixed samples consisting of events generated with different values of M_W^{gen} spanning the range of the fit, whenever possible. As shown in the next section, the Monte Carlo statistics I used was adequate for my measurements.

5.5 Fit of the Invariant Mass Spectra

An unbinned maximum likelihood fit is used to compare the data m^{5C} distribution with reweighted Monte Carlo predictions.

Distributions for the two best jet combinations are fitted separately in the [70 GeV, 90 GeV] range. Events with a reconstructed mass below 70 GeV have a very small chance of coming from a $W^+W^- \rightarrow q\bar{q}q\bar{q}$ event with the correct jet combination found, and do not carry information about the W mass.

The likelihood maximized in the fit is a product of the M_W-dependent probability

densities in m^{5C}

$$L(M_W) = \prod_i \frac{1}{c(M_W)\sigma_{WW}(M_W) + \sigma_{bg}} (c(M_W)\frac{d\sigma_{WW}}{dm^{5C}}(m^{5C}{}_i, M_W) + \frac{d\sigma_{bg}}{dm^{5C}}(m^{5C}{}_i)), \quad (5.12)$$

evaluated for all data events in the fit range. The factor $c(M_W) \equiv \sigma_{WW}^{measured}/\sigma_{WW}(M_W)$ normalizes the M_W-dependent accepted W^+W^- cross section to the measured one. After this correction the results of the fit depend only on the shape of the m^{5C} distributions and not on the number of events in them.

The total and differential cross sections $\sigma_{WW}(M_W)$, $\frac{d\sigma_{WW}}{dm^{5C}}(m^{5C}{}_i, M_W)$, and $\frac{d\sigma_{bg}}{dm^{5C}}(m^{5C}{}_i)$ are evaluated numerically with the box method [104]. A bin (box) with a width Δ_i is constructed around each data event with the reconstructed average invariant mass of $m^{5C}{}_i$. The Monte Carlo prediction for the accepted cross section and the differential cross section at $m^{5C}{}_i$, reweighted to M_W, are then given by

$$\sigma_{WW}(M_W) = \sigma_{WW}(M_W^{ref})\frac{\sum w_i(M_W)}{\sum w_i(M_W^{ref})} \quad (5.13)$$

$$\frac{d\sigma_{WW}}{dm^{5C}}(m^{5C}{}_i, M_W) = \frac{\sigma(M_W^{ref})}{\sum w_i(M_W^{ref})}\frac{1}{\Delta_i}\sum_{j\in\Delta_i} w_j(M_W), \quad (5.14)$$

where the latter sum is over the Monte Carlo events inside the ith box. The weights are unity for background Monte Carlo events and are given by the reweighting formula (5.11) for W^+W^- Monte Carlo events. The reference W mass M_W^{ref} is chosen to be in the middle of the W mass range covered by the W^+W^- Monte Carlos used in the reweighting.

The bins $[m^{5C}{}_i\text{-}\frac{1}{2}\Delta, m^{5C}{}_i+\frac{1}{2}\Delta]$ were centered around the data events $m^{5C}{}_i$ and had equal size of 250 MeV for the W^+W^- Monte Carlo, small enough to provide an adequate description of the Breit-Wigner resonant shape. Bins of 2 GeV were used for background Monte Carlos, large enough to guarantee sufficient Monte Carlo statistics in each background box. Other box algorithms, both data-dependent and fixed, were tried, and no significant difference was found either in the results of the fits on data,

or in expected accuracy of the measurement.

I treat the mass distributions of the best and second best jet combinations as independent, i.e., the likelihood minimized in the fit is given by the product of two likelihoods (5.12), and the ML estimate of the statistical error is obtained by solving numerically

$$\ln L(m^{ML} \pm \Delta_{\pm} m^{ML}) \;=\; \ln L(m^{ML}) - \frac{1}{2}. \tag{5.15}$$

One can question the validity of this approach, as both combinations in an event are formed with the same jets, and the resulting two m^{5C} masses are strongly correlated on an event-by-event basis. A priori, these correlations should lead to a correlation between the results of the fits of the two distributions. This turns out not to be the case. At most one of the two combinations maps correctly onto the two W bosons and carries information about the W mass, contributing to the result of the fit of the corresponding distribution. The other one (or both) lie in the flat background of incorrect combinations and do not significantly affect the result of the fit in which it is used. Therefore, I expect the results of the fits of the first and second combinations to be essentially uncorrelated. This property of the fit was confirmed numerically. 50K samples of $\sqrt{s} = 189$ GeV Monte Carlo events were obtained by randomly combining signal and background Monte Carlo events in numbers given by the Poissonian distributions with the means corresponding to the SM expectations for the 98 data set.

No structure is seen in the scatter plot of the ML fit results of the best and second best jet combinations, performed with the samples, as shown in Figure 5.6. The correlation of the fits of the two jet combinations was evaluated to be

$$\begin{aligned} \varrho_{12} \;&\equiv\; \frac{\langle (m_1 - \langle m_1 \rangle)(m_2 - \langle m_2 \rangle) \rangle}{\sqrt{\langle (m_1 - \langle m_1 \rangle)^2 \rangle \langle (m_2 - \langle m_2 \rangle)^2 \rangle}} \\ &=\; -0.01 \pm 0.03, \end{aligned} \tag{5.16}$$

which allows me to safely neglect the correlation.

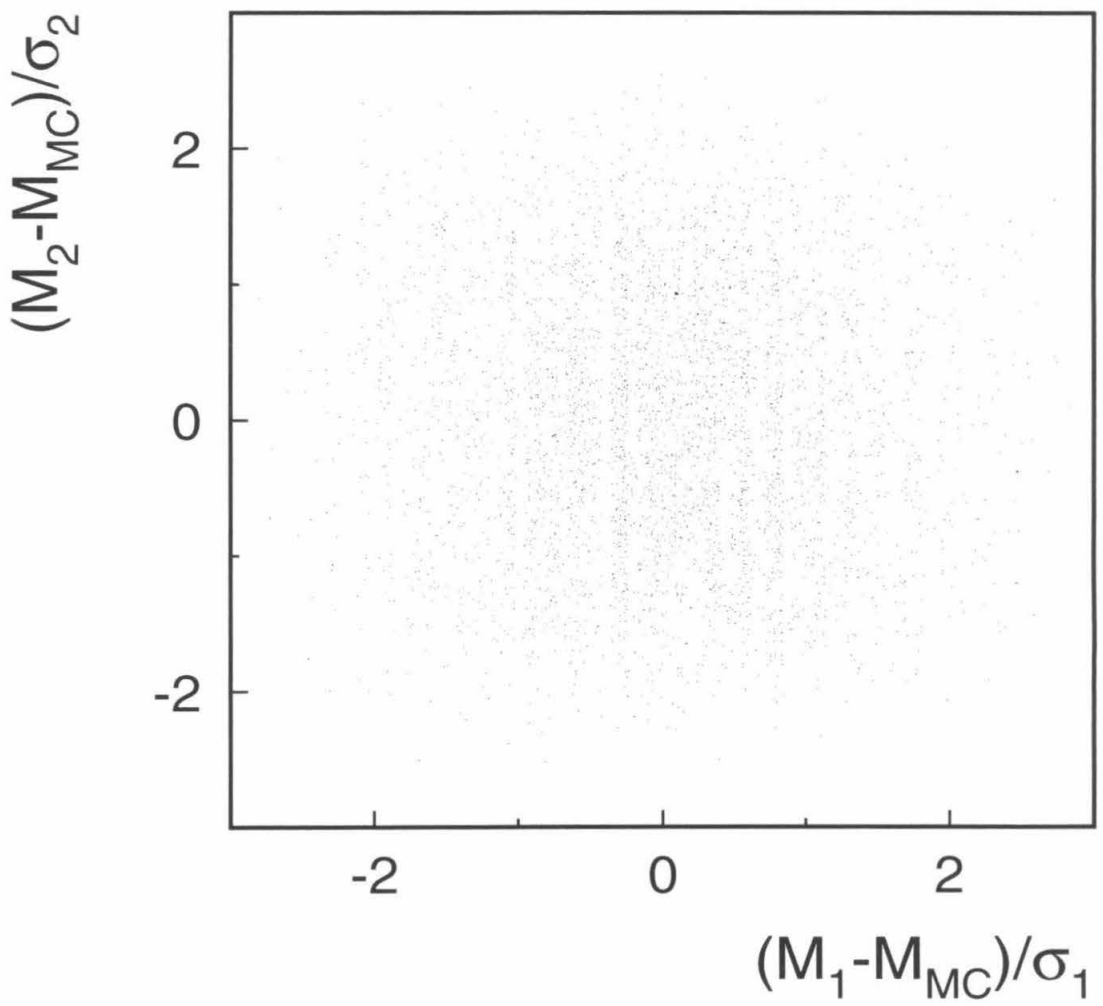

Figure 5.6: Correlation of the best and second best jet combination M_W fit results for Monte Carlo event samples.

The Monte Carlo reweighting ML fit described above gives consistent (asymptotically unbiased) estimates of M_W and the statistical uncertainty of the measurement. All effects affecting the resonant shape are taken into account exactly by the fit, provided they are correctly modelled by the Monte Carlo generators. The consistency of the estimators was checked by applying the fit to a large number of Monte Carlo event

samples, constructed in the way described in the previous paragraph, using W^+W^- MC events simulated at different values of M_W.

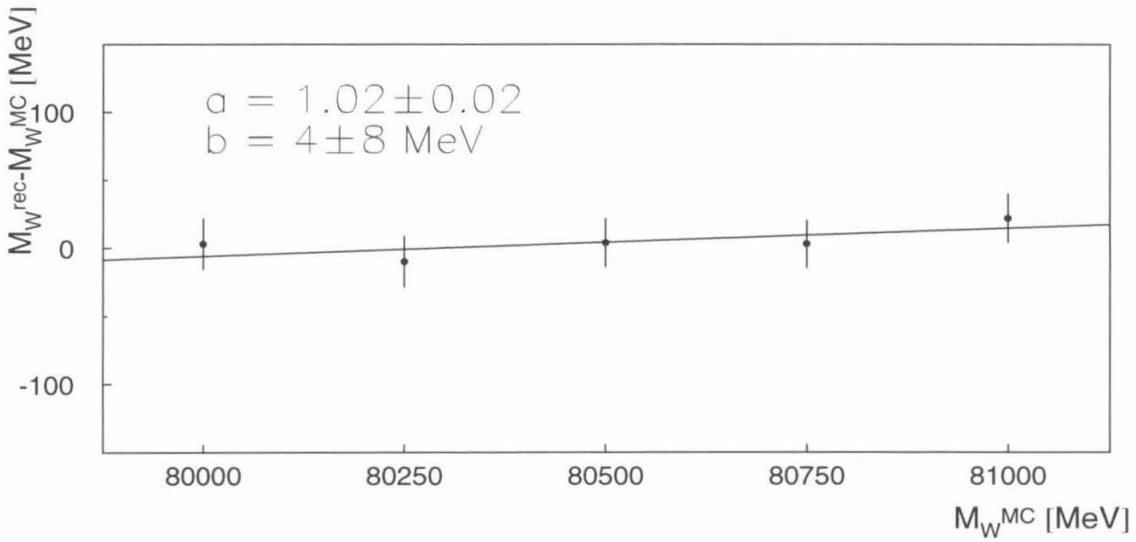

Figure 5.7: Average fitted W mass for small Monte Carlo samples with different M_W. Statistical uncertainties of the averages and the results of the linear regression are also given.

The average fitted W mass and its statistical uncertainty for each M_W point used is shown in Figure 5.7. Linear regression of the data with

$$\langle M_W^{rec} \rangle - 80500 \text{ MeV} = a(M_W^{gen} - 80500 \text{ MeV}) + b \quad (5.17)$$

gives a linearity coefficient $a = 1.02 \pm 0.02$ compatible with 1 and a negligible bias $b = 4 \pm 8$ MeV.

At each M_W point the spread of the fit results was compared to the distribution of the fit errors given by (5.15), as demonstrated in Figure 5.8. The average fit error agrees well with the standard deviation of the fit results at each M_W point considered, and, therefore, gives a good estimate of the statistical uncertainty of the mass measurement.

The technical checks described above were also performed for the W width fits.

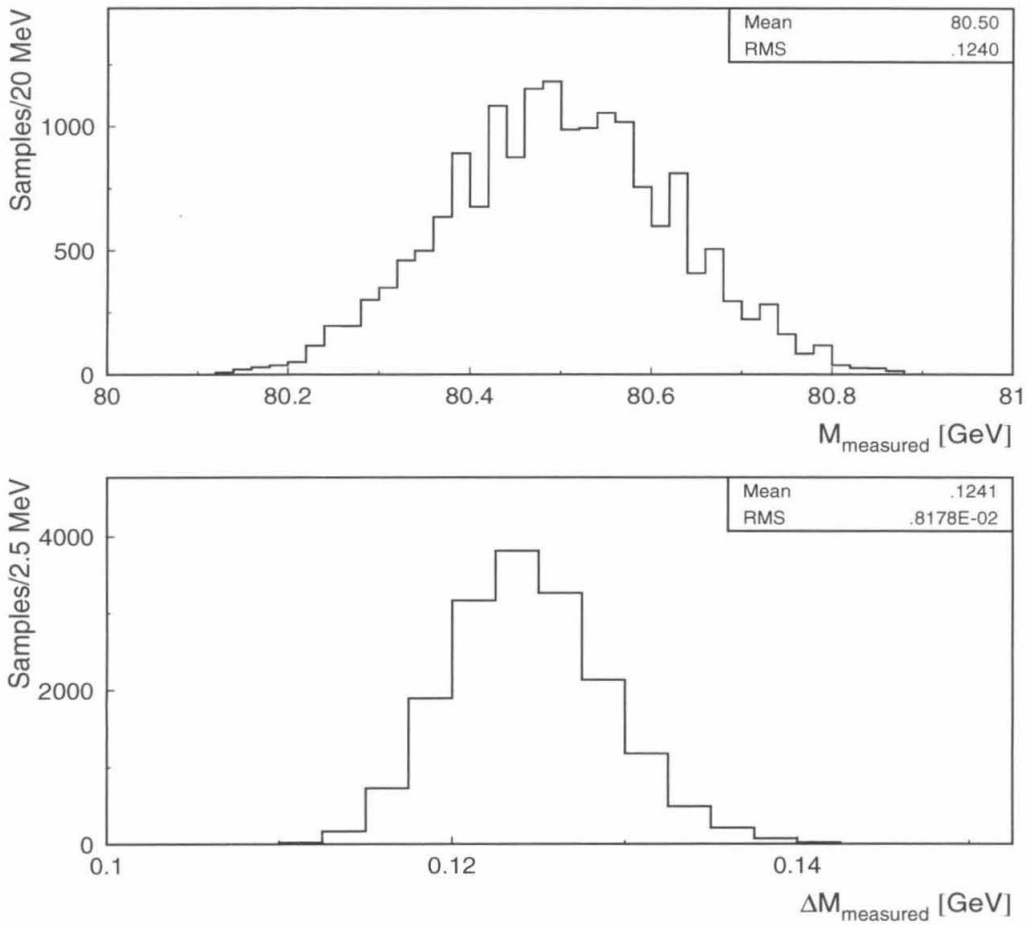

Figure 5.8: Distributions of the M_W fit results (a) and fit errors (b) for small Monte Carlo samples corresponding to $M_W = 80.500$ GeV. Means and standard deviations of the distributions are given.

As shown in Figure 5.9, the results are again compatible with a negligible bias and a linearity of 1. Also for the W width fits, the fit error gives an unbiased estimate of the statistical uncertainty of the measurement (see Figure 5.10).

The fit procedure described above was applied to the samples of $W^+W^- \to q\bar{q}q\bar{q}$ candidates selected in 96B, 97 and 98 L3 data sets, described in Table 5.1, giving the invariant mass spectra shown in Figure 5.5. The results of independent and simultaneous M_W and Γ_W fits with these data are summarized in Tables 5.2 and 5.3.

The results of independent and simultaneous M_W, Γ_W fits, as well as results

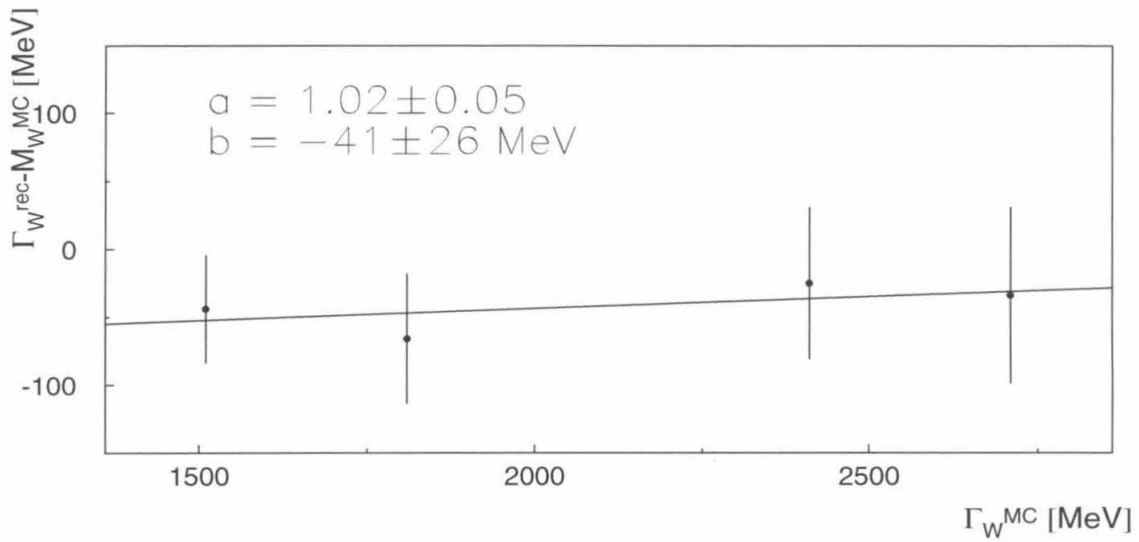

Figure 5.9: Average fitted W width for small Monte Carlo samples with different Γ_W. Statistical uncertainties of the averages and the results of the linear regression are also given.

Data Period	M_W [GeV]	Γ_W [GeV]
96B	$81.000^{+0.453}_{-0.427}$	$1.351^{+1.114}_{-0.639}$
97	$80.563^{+0.209}_{-0.209}$	$1.823^{+0.437}_{-0.508}$
98	$80.587^{+0.130}_{-0.129}$	$2.407^{+0.350}_{-0.382}$
All data	$80.603^{+0.107}_{-0.107}$	$2.167^{+0.291}_{-0.274}$

Table 5.2: Results of independent M_W and Γ_W measurements with direct reconstruction of $W^+W^- \rightarrow q\bar{q}q\bar{q}$ events. The errors are statistical.

obtained with different L3 data sets, are in good agreement with each other. The mass-width correlation for simultaneous fits is small, which agrees with the intuitive understanding of the fit using different features of the reconstructed mass spectra to determine M_W and Γ_W. The observed statistical errors are compatible with MC expectations for event samples of the size observed in the data.

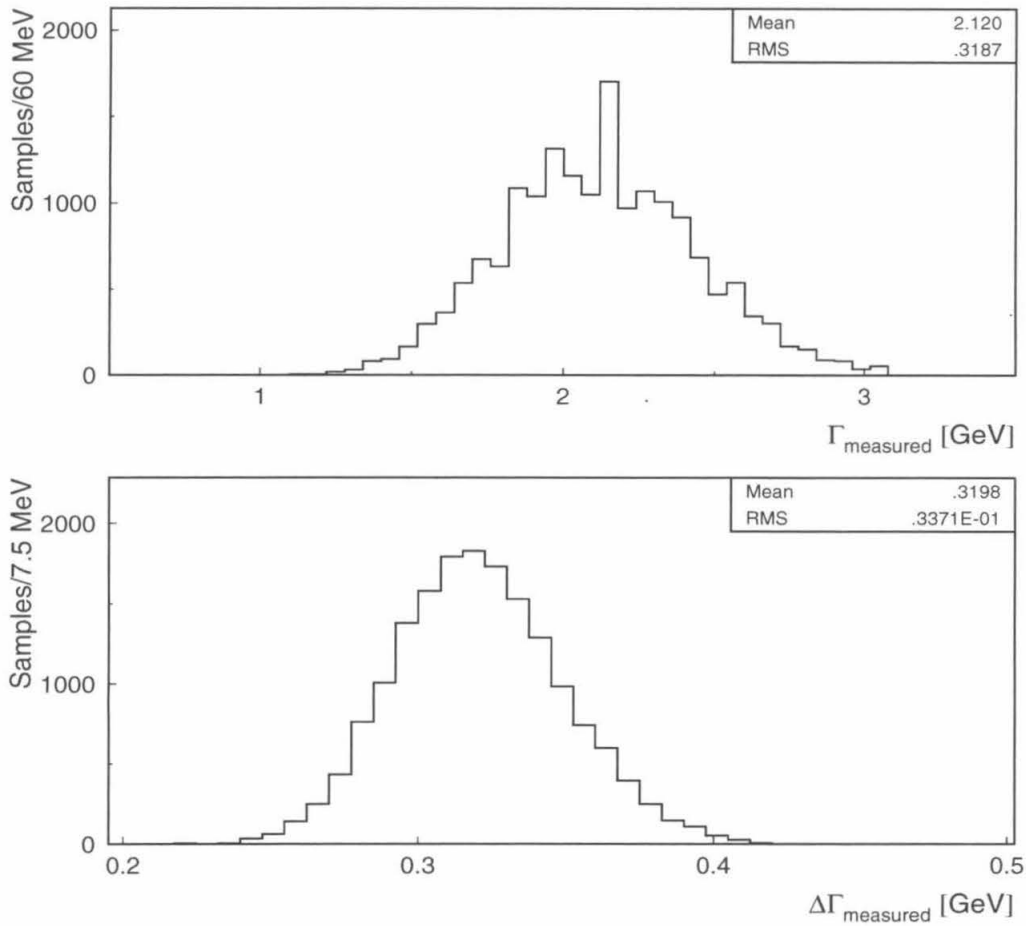

Figure 5.10: Distributions of the Γ_W fit results (a) and fit errors (b) for small Monte Carlo samples corresponding to $\Gamma_W = 2.110$ GeV. Means and standard deviations of the distributions are given.

5.6 Direct Reconstruction Measurement Uncertainties

The fit method described corrects implicitly for many effects that affect the invariant mass distribution provided those are modeled correctly by the Monte Carlo simulations. As already discussed in Section 4.11 possible sources of biases of the W mass measurement are imperfections of the Monte Carlo codes used to simulate signal and background events, and incorrect simulation of the detector response, affecting both

Data Period	M_W [GeV]	Γ_W [GeV]	$\varrho_{M_W\Gamma_W}$
96B	$81.032^{+0.396}_{-0.300}$	$1.168^{+1.131}_{-1.024}$	0.255
97	$80.559^{+0.203}_{-0.202}$	$1.830^{+0.506}_{-0.437}$	0.033
98	$80.580^{+0.134}_{-0.136}$	$2.383^{+0.384}_{-0.351}$	-0.050
All data	$80.603^{+0.107}_{-0.108}$	$2.148^{+0.293}_{-0.272}$	-0.030

Table 5.3: Results of simultaneous M_W and Γ_W measurements with direct reconstruction of $W^+W^- \rightarrow q\bar{q}q\bar{q}$ events. The errors are statistical. The correlation between the measurements is also given.

kinds of MC events. The corresponding systematic errors were evaluated by performing the mass measurements on large Monte Carlo samples generated with modified model parameters or different MC models, with unchanged baseline MC samples.

The systematic errors were reevaluated for each set of data and Monte Carlo used in my analysis and were found to be consistent with each other. I assume errors from any given source, with the exception of the finite MC statistics error, to be fully correlated between data taking periods. I arrive at the combined systematic error by averaging errors for particular data samples, with weights given by the statistical errors of the relevant measurements.

Throughout this section I quote estimates of systematic errors for both the W mass and W width measurements, with the latter given in parentheses.

5.6.1 Modeling of the Detector Response

To evaluate possible systematic errors due to mismodeling the detector response, I follow the method used to calculate similar systematic errors in the measured production cross section. A large sample of hadronic Z^0 events was used to evaluate biases and resolution data-MC differences in the determination of jet energies and directions. The measurements were repeated upon applying the resulting corrections to Monte Carlo signal and background events. The changes of the fit result that these corrections led to were taken as estimates of the corresponding systematic errors.

Corrections of the jet energy scale and resolutions led to M_W (Γ_W) shifts of 10 (5)

and 0 (10) MeV respectively. Alternatively, neglecting data-MC subdetector calibration differences changes the measured W mass (width) by 15 (20) MeV. The latter was chosen as a conservative estimate of the effect of possible detector miscalibration on the measurements.

The same procedure was applied to angular biases and resolutions. θ and ϕ corrections to the directions of reconstructed jets change the fitted W mass (width) by 7 (8) MeV. Smearing jet directions leads to a change of 13 (26) MeV. I use the quadratic sum of these numbers as an estimate of the effect of possible jet direction mismeasurement.

5.6.2 Modeling of the W^+W^- Signal Properties

The uncertainties of the Monte Carlo models of W^+W^- production, which affected the cross section measurement, also were considered from the point of view of the measurement of the W mass.

- The effect of the CC03 approximation was again evaluated by reweighting Monte Carlo W^+W^- events with the ratios of the full and CC03 matrix elements, and redoing the mass fit with the resulting sample of weighted MC events. The result differs by 6 (9) MeV from the one obtained without reweighting.

- Initial state radiation has an important influence on the reconstructed W mass spectrum. Photons radiated by the incoming lepton beams typically escape detection and carry away on the order of 2 GeV of energy per W^+W^- event at 189 GeV. This loss is not accounted for by the kinematic fit, which leads to an upward shift of about

$$\Delta m^{5C} \approx \frac{M_W}{\sqrt{s}} \langle E_{ISR} \rangle \approx 1 \text{ GeV} \tag{5.18}$$

  in the dijet mass spectrum. Fortunately, the uncertainty on the fitted W mass is much smaller than the average energy loss, as reliable QED calculations are available and implemented in the Monte Carlo code that was used to simulate

W^+W^- events [29, 101]. These theoretical calculations have an intrinsic accuracy on $\langle E_{ISR} \rangle$ of about 15 MeV, which was taken as an estimate of possible systematic error on the W mass due to mismodeling of initial state radiation. Due to the effective convolution of the ISR spectrum with the relatively wide Breit-Wigner W resonant peak, I expect the uncertainty of the measured W width due to the mismodeling to be negligible.

- Similarly, emission of hard gluons by the final state quarks affects the reconstruction of dijet invariant masses. The four jet hypothesis, assumed by the jet combination algorithms and kinematic fit I used, doesn't hold for events with significant final state radiation. The success rate of the jet combination algorithm is significantly lower for the five-or-more jet events. For the subset of events with the correct jet combination chosen, the reconstructed mass spectrum still differs from the one obtained with four-jet events, due to worse mass resolution.

  Nevertheless, this doesn't result in large systematic errors as the description of such events by the Monte Carlo models I used was found to be adequate for my measurements. To evaluate a possible contribution to the systematic error, I repeat the mass (width) fit rejecting different fractions, up to 12%, of the data events with the highest values of y_{45}. This changes the fit result by up to 9±20 (13±54) MeV which I take as an estimate of the corresponding systematic error.

- As for the cross section measurement, the systematic errors due to modeling of fragmentation and interaction between two $W \rightarrow q\bar{q}'$ hadronic systems were evaluated by comparing a large number of Monte Carlo models not rejected by low energy data with the default model used for the measurement.

  To evaluate the systematic error due to modeling of hadronization, I perform a W mass fit using a HERWIG Monte Carlo sample as "data" and the default Monte Carlo sample with JETSET/LUND fragmentation as the baseline MC. I assign the difference of the fit result from the nominal W mass used to generate the HERWIG sample, 45±20 (93±59) MeV, to the systematic error of the

measured W mass (width) due to errors in modeling of fragmentation.

In the same manner, the 50±21 (47±61) MeV bias observed when fitting a MC sample generated without simulating Bose-Einstein correlations, relative to the default MC sample, was taken as an estimate of the corresponding systematic error on the W mass (width).

The biases found for various color reconnection models, varied in the 30–80 (20–80) MeV range for the W mass (width), each with a statistical uncertainty of approximately 20 (60) MeV. I take the bias observed for the Sjöstrand-Khoze I model, 54±20 (73±59) MeV, as an estimate of the error due to modeling of color reconnection.

5.6.3 Modeling of the Backgrounds

- To evaluate the sensitivity of the measurement to possible mismodeling of QCD background events, I redo the fit after giving $q\overline{q}$ Monte Carlo events y_{34}-dependent weights determined with Z^0 data, as described in Section 4.11. This leads to a change of the fitted W mass (width) of 0 (20) MeV. Similar shifts are achieved by increasing the accepted $q\overline{q}$ cross section by 5% in the fit, without changing the reconstructed mass distribution of $q\overline{q}$ Monte Carlo events, and by replacing the $q\overline{q}$ Monte Carlo distribution with an appropriately rescaled one obtained with data collected at the Z^0 peak.

- Also, repeating the fit while changing preselection cuts, which is equivalent to changing the fraction of background events in the fitted sample, led to a 9±21 (23±59) MeV shift of M_W (Γ_W). I combine this shift with the result of the y_{34} reweighting to arrive at an estimate of the systematic error due to possible mismodeling of the $q\overline{q}$ background.

- Z^0Z^0 events constitute another non-negligible background component in the event sample used for the W mass fit. For an estimate of the systematic error on M_W (Γ_W) due to modeling of this background, I take the shift of the fitted

W mass (width) of 1 (6) MeV which I obtain by changing the Z^0Z^0 accepted rate by $\pm 5\%$.

5.6.4 Beam Energy Uncertainty

A wrong estimate of the e^+e^- collision energy would force the kinematic fit to over-correct and bias the reconstructed dijet masses. Thus an uncertainty of the LEP beam energy directly translates into a systematic error on the W mass

$$\Delta M_W \approx \frac{M_W}{E_{beam}} \Delta E_{beam}. \tag{5.19}$$

The beam energy uncertainties reported in Table 3.1 lead to an error of 17 MeV on the measured W mass. This estimate was confirmed by repeating the measurements after changing the value of $\sqrt{s}$ used by the kinematic fit, by the amount of the LEP beam energy uncertainty, and observing the resulting change of the measurements. This procedure also leads to an estimate of the systematic error on the W width of 5 MeV.

5.6.5 MC Statistics

Because of the finite number of Monte Carlo events I used, the box method provides an imperfect approximation of the differential cross section used in the fits. The position and the width of the W mass peak is defined by the Monte Carlo with an uncertainty of approximately $\Gamma_W/\sqrt{N_{MC}}$, where N_{MC} is the MC statistics used.

To evaluate the systematic error due to this uncertainty, I split my Monte Carlo event samples into several (2–20) parts and repeat the mass fits using these subsets and the full amount of real data. The spread of the results gives an estimate of the systematic error of 7 (25) MeV, combining all data taking periods. The estimates obtained using different numbers of subsamples are consistent with each other.

5.6.6 Other Checks

A number of other checks of the fit were performed. No statistically significant changes were observed while changing technical parameters of the fit, such as box widths and the algorithms used to construct the boxes. The results were also stable with respect to changes of the sample used for the measurement, namely variations of the neural network output and kinematic fit probability cuts, and the range of the m^{5C} distribution used for the measurement. No additional systematic errors were assigned as a result of these checks.

5.6.7 Summary of the Systematic Uncertainties

The systematic errors of the W mass and width measurements are summarized in Table 5.4.

Source of uncertainty	M_W error [MeV]	Γ_W error [MeV]
Jet energy measurement	15	20
Jet direction measurement	15	27
CC03 approximation	6	9
ISR modeling	15	0
FSR modeling	9	13
Fragmentation	45	93
Modeling of BE correlations	50	47
Modeling of color reconnection	54	73
$q\bar{q}$ background (QCD modeling)	0	20
$q\bar{q}$ background (other)	9	23
Z^0Z^0 background	1	6
$\sqrt{s}$ uncertainty	17	5
MC statistics	7	25
Total	93	138

Table 5.4: Systematic errors of the measurements of M_W and Γ_W itemized by the source of the uncertainty. The quadratic sum of all contributions is also given.

Possible detector mismodeling gives rise to small systematic errors owing to tight constraints on detector miscalibration and misalignment that one can obtain from

low energy $q\bar{q}$ data.

Also small are systematic errors due to uncertainties of the background simulation, due to the high purity of the event sample used for the measurement and the low influence of the flat background m^{5C} distribution on the measurement of the W mass and, to a smaller degree, the width.

The dominant systematic errors in the determination of both W mass and width come from uncertainties of the simulation of hadronic structure in $W^+W^- \rightarrow q\bar{q}q\bar{q}$ events. The fragmentation and color reconnection errors are due to poor theoretical understanding of the non-perturbative QCD processes involved, while the Bose-Einstein correlations error is caused by the intrinsic difficulty of simulating the quantum mechanical phenomenon with probabilistic Monte Carlo models.

The systematic errors are smaller than the statistical ones for my measurements, but they will become more important for the final analysis of the total LEP 2 data sample.

5.7 Summary of the Results

This section summarizes the results of my analysis of the dijet invariant mass spectra reconstructed with four-jet $W^+W^- \rightarrow q\bar{q}q\bar{q}$ events. I measured the W boson mass and width to be

$$M_W = 80.60 \pm 0.11(stat.) \pm 0.09(syst.) \text{ GeV} \quad (5.20)$$

$$\Gamma_W = 2.15 \pm 0.28(stat.) \pm 0.14(syst.) \text{ GeV}. \quad (5.21)$$

Similar measurements were done by L3 with W invariant mass distributions reconstructed with semileptonic W^+W^- events [105]. Their results

$$M_W = 80.22 \pm 0.12(stat.) \pm 0.07(syst.) \text{ GeV} \quad (5.22)$$

$$\Gamma_W = 2.22 \pm 0.30(stat.) \pm 0.17(syst.) \text{ GeV} \quad (5.23)$$

are in agreement with my measurements within their statistical and systematic errors. I combine them to arrive at the best estimate of the W mass and width using the L3 high energy data collected during 1996–1998. Another independent measurement of these parameters using lepton energy spectra is available [102], but its significantly lower precision and partial correlation with the direct m^{5C} reconstruction $q\bar{q}\ell\nu$ measurements make its inclusion impractical.

Some of the systematic errors of the $q\bar{q}\ell\nu$ measurement, described in [105], are positively correlated with those of the $q\bar{q}q\bar{q}$ one, e.g., the LEP beam energy and ISR modeling errors. The contribution of such fully correlated errors into the total systematic error is small for both channels. Some larger ones, for example the errors due to the detector response and fragmentation modeling, are related for both measurements, but the relationship is non-trivial and it is impossible to determine either the size or the sign of the possible correlation. The largest errors, due to Bose-Einstein correlations and color reconnection modeling, are present only for the $q\bar{q}q\bar{q}$ measurement. Therefore, assuming all systematic errors uncorrelated is a valid approximation when combining the $q\bar{q}q\bar{q}$ and $q\bar{q}\ell\nu$ measurements. I checked that this simplification can lead to an underestimate of the combined systematic error of at most 10%.

The result of the combination is

$$M_W = 80.43 \pm 0.08(stat.) \pm 0.06(syst.) \text{ GeV} \quad (5.24)$$

$$\Gamma_W = 2.18 \pm 0.20(stat.) \pm 0.11(syst.) \text{ GeV}. \quad (5.25)$$

The direct reconstruction W mass measurement can be combined with the (uncorrelated) threshold one, (5.9), to obtain the best estimate of the W mass

$$M_W = 80.44 \pm 0.08(stat.) \pm 0.06(syst.) \text{ GeV}. \quad (5.26)$$

The measured value of the W mass is in good agreement with measurements by other LEP and Tevatron experiments [106, 107, 108, 109, 110, 111], as well as indirect determination using other precision electroweak measurements [112].

The measurement of the W width agrees well with the Standard Model prediction (2.13) using the measured value of the W mass, and with other direct and indirect measurements [23].

Chapter 6

Search for Anomalous Triple Gauge Boson Couplings

The $W^+W^- \to q\bar{q}q\bar{q}$-enriched event sample I select can also be used to study triple gauge couplings involving the W boson.

The total W^+W^- production cross section already provides some information about the structure of the $e^+e^- \to W^+W^-$ matrix element. Delicate cancellations between the Feynman graphs shown in Figure 2.2 are necessary for good high-energy behavior of the W^+W^- cross section. A coupling set different from the one predicted by the Standard Model would destroy the gauge cancellations and force some partial-wave amplitudes to violate the unitarity bounds above some energy threshold. Already at the energies available at LEP 2, non-SM triple gauge boson couplings would result in significant deviations of the measured W^+W^- cross section from the SM predictions, as illustrated in Figure 4.28.

Still more information about the gauge couplings is contained in the differential W^+W^- cross section. Changes of the couplings affect each $e^+e^- \to W^+W^-$ helicity amplitude differently and generally modify the angular dependence of both the production rate and polarization of the W bosons. The polarization of the W bosons determines, in turn, the angular distributions of their decay products relative to the W flight direction, through the V-A charged weak current interaction. To access all available information about $e^+e^- \to W^+W^-$ amplitudes, one would study the full four-fermion production differential cross sections.

In the limit of zero W width and no initial state radiation, both W momenta in the rest frame and the fermion momenta in the W bosons' rest frames are constants determined by $\sqrt{s}$ and M_W. Provided the incoming lepton beams have no significant

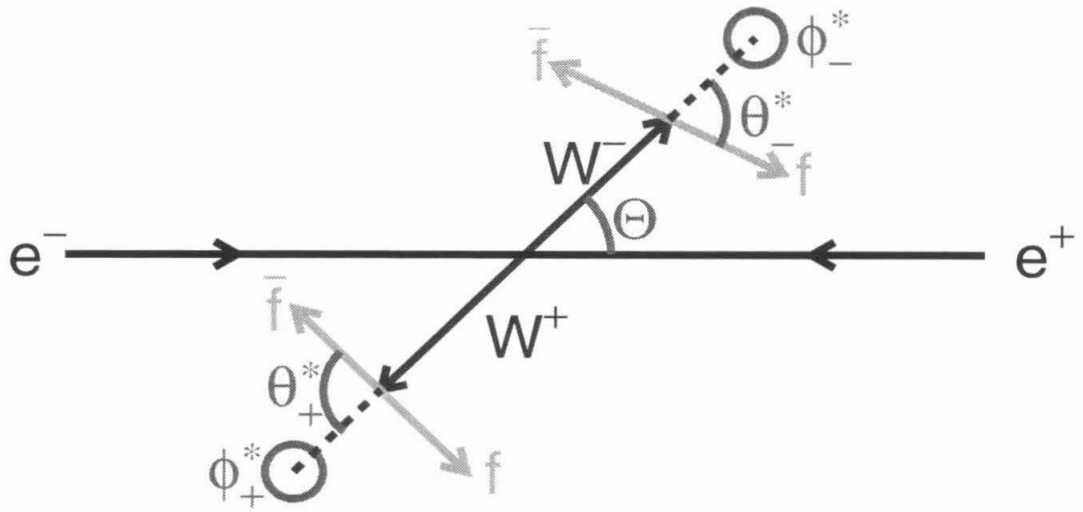

Figure 6.1: The phase space of the $e^+e^- \to W^+W^- \to f_1\bar{f}_2f_3\bar{f}_4$ four-fermion system.

transverse polarization, the final state is invariant with respect to rotations around the beam axis. With these assumptions the final four fermions' phase space is completely described by the set of the five decay angles shown in Figure 6.1. The polar angle Θ_W determines the direction of the negatively charged W boson with respect to the direction of the incoming electron. Two more polar (θ_1, θ_2) and two azimuthal (ϕ_1, ϕ_2) angles describe the fermion flight direction in the respective W boson rest frames.

While one would ideally study the full five-dimensional differential cross section $\frac{d\sigma(e^+e^- \to f_1\bar{f}_2f_3\bar{f}_4)}{d\cos\Theta_W d\cos\theta_1 d\phi_1 d\cos\theta_2 d\phi_2}$, it is impossible in practice to reconstruct all of the angles in W^+W^- events of any category. Measurement difficulties are especially large for four-jet events and restrict the analysis to the W^- polar angle Θ_W. In semileptonic W^+W^- events it is possible to determine the charge of the lepton with high reliability, and that allows one to reconstruct the decay phase space of the leptonically-decaying W boson. Other advantages of this class of W^+W^- events are the absence of combinatorial problems and the straightforward identification of the negatively charged W boson. While both lepton charges are known in $\ell\nu\ell\nu$ events, the flight directions of the W bosons cannot be determined unambiguously, which limits the usefulness of such events for measurements of anomalous couplings.

This chapter describes my study of the $\cos\Theta_W$ distribution, including the deter-

mination of the flight direction of the W^- and the selection of $W^+W^- \to q\bar{q}q\bar{q}$ events used for my measurements, as well as the maximum likelihood fit used to obtain estimates of the gauge couplings given the reconstructed distributions in $\cos\Theta_W$. The results of applying these methods to the selected L3 event samples and an analysis of the systematic uncertainties of the measurement are also presented.

The data collected by L3 at $\sqrt{s}$ of 189 GeV are used for data-Monte Carlo comparisons in this chapter as the most statistically significant dataset used in my analysis, except where indicated otherwise.

6.1 Parametrization of Trilinear Couplings of the W Boson

To check for and quantify possible deviations of the $e^+e^- \to W^+W^-$ matrix element from the sum of SM amplitudes shown in Figure 2.2, one has to consider a more general form of the matrix element. The most general form of a Lorentz-invariant Lagrangian, describing triple gauge boson vertices involving the W boson [113], contains seven arbitrary constants for each neutral gauge boson,

$$\begin{aligned} i\frac{\mathcal{L}_{VW^+W^-}}{g_{VW^+W^-}} =& g_1^V V^\mu (W^-_{\mu\nu} W^{+\nu} - W^+_{\mu\nu} W^{-\nu}) + \kappa_V W^+_\mu W^-_\nu V^{\mu\nu} + \frac{\lambda_V}{M_W^2} V^{\mu\nu} W^{+\rho}_\nu W^-_{\rho\mu} \\ &+ i g_4^V W^+_\mu W^-_\nu (\partial^\mu V^\nu + \partial^\nu V^\mu) \\ &+ i g_5^V \epsilon_{\mu\nu\rho\sigma} ((\partial^\rho W^{-\mu}) W^{+\nu} - W^{-\mu} (\partial^\rho W^{+\nu})) V^\sigma \\ &+ \frac{\tilde{\kappa}_V}{2} \epsilon^{\mu\nu\rho\sigma} W^+_\mu W^-_\nu V_{\rho\sigma} - \frac{\tilde{\lambda}_V}{2M_W^2} W^-_{\rho\mu} W^{+\mu}_\nu \epsilon^{\nu\rho\alpha\beta} V_{\alpha\beta}, \end{aligned} \tag{6.1}$$

where the coupling strengths for $V=\gamma, Z^0$ are

$$g_{\gamma W^+W^-} = e = \sqrt{4\pi\alpha_{em}} \tag{6.2}$$

$$g_{Z^0 W^+W^-} = e \cot\theta_W. \tag{6.3}$$

The Standard Model Lagrangian can be derived from (6.1) by assuming

$$g_1^V = 1, \quad \kappa_V = 1, \quad \lambda_V = 0, \tag{6.4}$$

and the rest of the couplings vanishing.

Linear combinations of the coupling constants in (6.1) determine the static electromagnetic properties of the W boson, namely the electric charge

$$q_W = -eg_1^\gamma \xrightarrow{SM} -e, \tag{6.5}$$

the magnetic and electric dipole moments

$$m_W = \frac{-e}{2\mathrm{M_W}}(g_1^\gamma + \kappa_\gamma + \lambda_\gamma) \xrightarrow{SM} \frac{-e}{\mathrm{M_W}}, \tag{6.6}$$

$$d_W = \frac{-e}{2\mathrm{M_W}}(\tilde{\kappa}_\gamma + \tilde{\lambda}_\gamma) \xrightarrow{SM} 0, \tag{6.7}$$

and the electric and magnetic quadrupole moments

$$Q_W = \frac{e}{\mathrm{M_W^2}}(\kappa_\gamma - \lambda_\gamma) \xrightarrow{SM} \frac{e}{\mathrm{M_W^2}}, \tag{6.8}$$

$$M_W = \frac{e}{\mathrm{M_W^2}}(\tilde{\kappa}_\gamma - \tilde{\lambda}_\gamma) \xrightarrow{SM} 0. \tag{6.9}$$

It is difficult to interpret experimental data in terms of 14 free complex parameters. Therefore the triple gauge boson couplings parameter space has to be restricted by applying additional requirements on the Lagrangian (6.1). I assume all couplings to be real, and disregard those inducing C or P-violating interactions. This leaves a set of six parameters $g_1^V, \kappa_V, \lambda_V$, where V=$\gamma$,$Z^0$. Moreover, g_1^γ is fixed to be 1 by the electromagnetic gauge invariance requirement. The space of the remaining five parameters can be further reduced by classifying all possible SU(2)×U(1)-invariant operators involving triple gauge boson vertices, according to their dimension. Operators of higher dimensions are expected to be suppressed by powers of the presumably large "new physics" scale. The couplings corresponding to the remaining operators

become constrained. In the scheme adopted by the LEP experiments one considers models with a relatively light Higgs boson, in which case the "new physics" and the SU(2)×U(1) breaking happen independently, and operators giving rise to triple gauge boson vertices can be constructed with only Standard Model vector and scalar fields. The relations between lower-dimensional operators of such kind provide two more constraints [114] on the VW^+W^- couplings:

$$\Delta\kappa_\gamma = \cot^2\theta_W(\Delta\kappa_Z - \Delta g_1^Z) \quad (6.10)$$

$$\lambda_\gamma = \lambda_Z, \quad (6.11)$$

where

$$\Delta\kappa_V \equiv \kappa_V - 1, \qquad \Delta g_1^Z \equiv g_1^Z - 1. \quad (6.12)$$

The additional constraints reduce the number of free parameters to three. I choose the set of Δg_1^Z, $\Delta\kappa_\gamma$, and λ_γ to parametrize possible deviations of the triple gauge boson vertices from the Standard Model form. Other parametrizations, inspired by different realizations of "new physics," are possible [115].

6.2 Reconstruction of the W^- Direction Distribution

In my analysis I study the angular dependence of W^+W^- production. I reconstruct the distribution of the polar angle of W^- bosons in three steps. First I combine the jets into pairs to form candidate primary W bosons. Then I try to find the dijet combination which is most likely to form a negatively charged W boson. To that end I estimate the charges of the jet pairs using a jet charge algorithm. At the last step I tighten the event selection requirements to avoid dealing with events where my measurements have especially large uncertainties.

The problem of combining jets is simpler for this measurement than for the mea-

surement of the W mass. The distribution in $\cos\Theta_W$ given by incorrect jet combinations always has a large overlap with the one given by correct combinations. The best way to reduce the background given by incorrect combinations is to maximize the success rate of the combination algorithm. For the reconstruction of the $\cos\Theta_W$ distribution, I choose the algorithms I used for the $W^+W^- \to q\bar{q}q\bar{q}$ cross section measurement, the Σ'm (Δm) algorithms at 172 (183, 189) GeV, as they give the highest rate of correct assignment of jets to primary W bosons (see Subsection 4.5.4).

I don't use the data collected at the W-pair production threshold for my measurements of triple gauge boson couplings. At low energy a W boson is reconstructed as a pair of back-to-back jets with typically low total momentum. Because of that both the magnitude and the direction of the momentum vector can be measured only with very large errors. Moreover, at the threshold the s-channel amplitudes containing triple gauge boson vertices are suppressed by a factor of β_W, which makes the total cross section at this energy less sensitive to possible anomalous VW^+W^- couplings.

On the contrary the contribution of s-channel diagrams is large at higher energies. The direction of the flight of the W can be measured with an uncertainty of only a few degrees, provided the correct jet pairs were constructed by the jet combination algorithm. This uncertainty is small compared to the characteristic width of the $\cos\Theta_W$ distribution and doesn't impair the sensitivity of the distribution to anomalous couplings.

6.2.1 Jet and W Boson Charge Estimation

The most serious uncertainty in the reconstruction of $\cos\Theta_W$, in an event with the correct jet combination found, is due to the difficulty of determining which of the two W boson candidates represents the primary W^-. Incorrect W charge assignments produce $\cos\Theta_W \to -\cos\Theta_W$ migration of events. This results in a background whose distribution is fully anticorrelated with the one given by the correct combinations, with respect to changes of gauge boson couplings. Thus a W^- charge confusion probability of x would lead to a decrease in the sensitivity of the measurement by

a factor 1-2x, which is very significant for the values of x which can be achieved in practice.

The charge of a W boson would be trivial to deduce given the charges of the quarks into which it decayed. Assuming quarks i and j were produced in the decay of a W boson, the sign of the combination of quark charges

$$Q_{ij} \equiv q_i + q_j - \sum_{k \neq i,j} q_k \tag{6.13}$$

would coincide with the sign of the charge of the original W boson. Unfortunately, one can only attempt to estimate the quark charges given information about the detected products of their fragmentation.

The jet charge estimator I used for this purpose is inspired by the parton cascade picture of fragmentation. In the simplest model of this kind, the Field-Feynman independent fragmentation model [116], the information about the charge of the fragmenting quark is carried by a few higher-momentum particles produced during the fragmentation, which have a higher chance to be produced at the top of the parton cascade and to actually contain the original quark. Therefore, an estimator of the quark charge could be given by an average of charges of particles belonging to a jet, with higher weights given to faster particles and lower ones to less energetic ones.

Given the list of particles combined into a jet by the Durham algorithm (see Subsection 4.5.1), I define the charge of the jet as a normalized weighted average of charges of all tracks in the list

$$q_{jet} = \frac{\sum w(p_i) q_i}{\sum w(p_i)}, \tag{6.14}$$

with the weights given by a power of the projection of the track momentum on the jet axis

$$w(p_i) = (p_i^{||})^{\kappa}. \tag{6.15}$$

Only tracks with a minimal p_T of 150 MeV are included in the average. The optimal

value of the exponent was found to be 0.5 in a dedicated study of the jet charge algorithm [117].

The precision of the quark charge estimates obtained with this algorithm is low because of the fluctuations intrinsic in the parton cascade. The performance is further degraded by neutral particles produced in the shower and particle decay products. Nevertheless it still turns out to be possible to correctly identify the charges of the W bosons in a large fraction of $W^+W^- \to q\bar{q}q\bar{q}$ events.

6.2.2 Event Selection and Jet Combination

Starting with the sample of four-jet events accepted by the neural network selection described in Section 4.8, I try to increase the fraction of correctly identified W^- bosons by improving or rejecting some jet charge measurements which are likely to be incorrect.

First I reject a small fraction of events without TEC information, recorded in the beginning of each LEP fill. Jet charges cannot be reconstructed in such events and they are not used for the measurement.

Also I consider unreliable any jet charge obtained with less than 3 tracks. Such jets are concentrated at low polar angles, which is an area of low efficiency of the tracking system and high particle losses. I try to correct such possible mismeasurements by assigning to such jets the charge found for the other jet of the W boson candidate pair. This has an effect of neglecting the mismeasured jet charge while estimating the charge of the jet pair it belongs to. The distribution of the number of tracks used for jet charge measurements, shown in Figure 6.2, is in agreement with the MC prediction.

If both jets in a W candidate have less than 3 tracks, I consider the jet pair charge undetermined and assign zero to both jet charges. This has the effect of using only the charge of the other W candidate while constructing the difference (6.13).

Finally, I reject events in which both W candidates have undetermined charges. In the remaining events I compare the two jet pairs found as described in the previous

section, and assume the one with the algebraically smaller value of Q defined by (6.13) to be the W^-. Figure 6.3 shows the distribution of the W charge estimator Q observed in data.

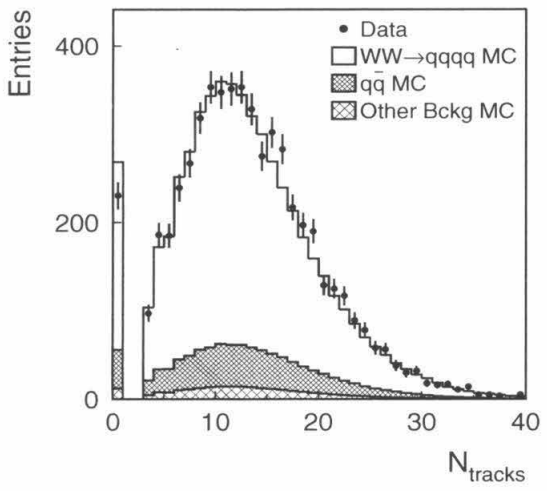

Figure 6.2: Distribution of the number of tracks used in jet charge measurement.

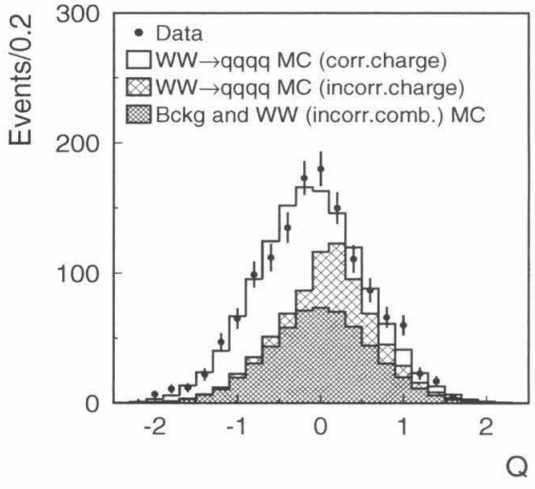

Figure 6.3: Distribution of the W boson charge sign estimator. Difference of the charges of the forward ($\cos\Theta_W > 0$) and the backward ($\cos\Theta_W < 0$) W candidates is shown.

The additional requirements reduce the data statistics, but increase the statistical sensitivity of the $\cos\Theta_W$ distribution for the selected sample. The results of applying the jet charge cuts to the L3 data samples I used in my analysis are summarized in Table 6.1. The expected and observed ratios of selected events are in good agreement at all energies considered.

I evaluate the performance of the W charge estimator (6.13) by applying it to a large sample of Monte Carlo events. The negatively charged W boson is found by the algorithm in 72% of $W^+W^- \to q\bar{q}q\bar{q}$ events in which the correct jet pairs were constructed by the jet combination procedure. The estimates of the probability of the correct charge assignment obtained at different energies were found to be consistent with each other.

	Data Period		
	96B	97	98
N_{total}	57	468	1393
$N_{selected}$	56	449	1384
N_{exp}	57 ± 8	381 ± 20	1363 ± 37

Table 6.1: Number of selected $W^+W^- \rightarrow q\bar{q}q\bar{q}$ candidates in data, together with SM Monte Carlo expectations. Also given is the standard deviation on the total number of selected events expected in the SM.

The charge separation provided by the jet charge algorithm proves to be useful to distinguish two W bosons with a charge difference of $2e$. Unfortunately, this is not adequate for the much more challenging task of distinguishing two quarks coming from the same W, with a charge difference of only $\frac{1}{3}e$. Consequently, one cannot determine quark flavors and reconstruct the W decay phase space for W bosons decaying into hadrons. This precludes the use of information about W decays, i.e., W polarizations, in my measurement of triple gauge boson couplings using four-jet events.

6.3 Extended Maximum Likelihood Fit

To determine the W boson couplings given the reconstructed $\cos\Theta_W$ distributions, I use a method similar to the one developed for the W mass fit.

A binned maximum likelihood fit is used to compare the data distribution with reweighted Monte Carlo predictions. The reconstructed $\cos\Theta_W$ distributions are fitted in the [-1, 1] range in bins of equal size of 0.1, $\Delta_i = [-1 + 0.1(i-1), -1 + 0.1i]$. The chosen bin size is small in comparison to the characteristic structure size of the $\cos\Theta_W$ distribution, and is sufficient to guarantee large enough MC statistics in each bin.

Denoting the number of data events found in bin i and the vector of the coupling values to be determined $\vec{\Omega}$, the likelihood maximized in the fit is a bin-by-bin product

of Poissonian probabilities

$$L(\vec{\Omega}) = \prod_{i=1,20} \frac{1}{N_i!} e^{-\mu_i} \mu_i^{N_i}, \tag{6.16}$$

where the bin content Monte Carlo expectations are

$$\mu_i = \int_{\Delta_i} \frac{d\sigma_{\mathrm{WW}}}{d\cos\Theta_{\mathrm{W}}}(x, \vec{\Omega}) + \frac{d\sigma_{bg}}{d\cos\Theta_{\mathrm{W}}}(x) dx. \tag{6.17}$$

The cross section integrals are evaluated as sums of weights of the Monte Carlo events inside the ith bin,

$$\int_{\Delta_i} \frac{d\sigma}{d\cos\Theta_{\mathrm{W}}}(x, \vec{\Omega}) dx = \frac{\sigma(\vec{\Omega}_0)}{0.1 \sum w_j(\vec{\Omega}_0)} \sum_{j \in \Delta_i} w_j(\vec{\Omega}). \tag{6.18}$$

The background Monte Carlo events have constant weight independent of the couplings $\vec{\Omega}$ while the $\mathrm{W^+W^-}$ MC events are reweighted from the Standard Model parameter set $\vec{\Omega}_0$ to $\vec{\Omega}$ according to formula (5.11). EXCALIBUR matrix elements were used to calculate the weights, as described in Section 5.4.

Unlike the likelihood (5.12) maximized in the $\mathrm{M_W}$ fits, the one used here makes use of the W-coupling dependence of the total $\mathrm{W^+W^-}$ production cross section, i.e., the overall normalization of the distribution. In this case the information contained in the total event rate is significant compared to the one given by the shape of the distribution and cannot be ignored. Using the event rate information reduces the statistical uncertainty of the fit results by 20–40%, depending on the coupling.

As in the $\mathrm{M_W}$ case, the reweighting method corrects implicitly for selection and reconstruction biases as well as their possible dependence on the couplings fitted.

As I did not have samples of Monte Carlo $\mathrm{W^+W^-} \rightarrow \mathrm{q\bar{q}q\bar{q}}$ events generated with various non-zero anomalous triple gauge boson couplings, I used samples of semileptonic $\mathrm{W^+W^-}$ MC events for technical checks of the maximum likelihood estimator. As for the $\mathrm{M_W}$ fits, the estimates of both the fitted parameters and their uncertainties were found to be unbiased in the whole range of the fit.

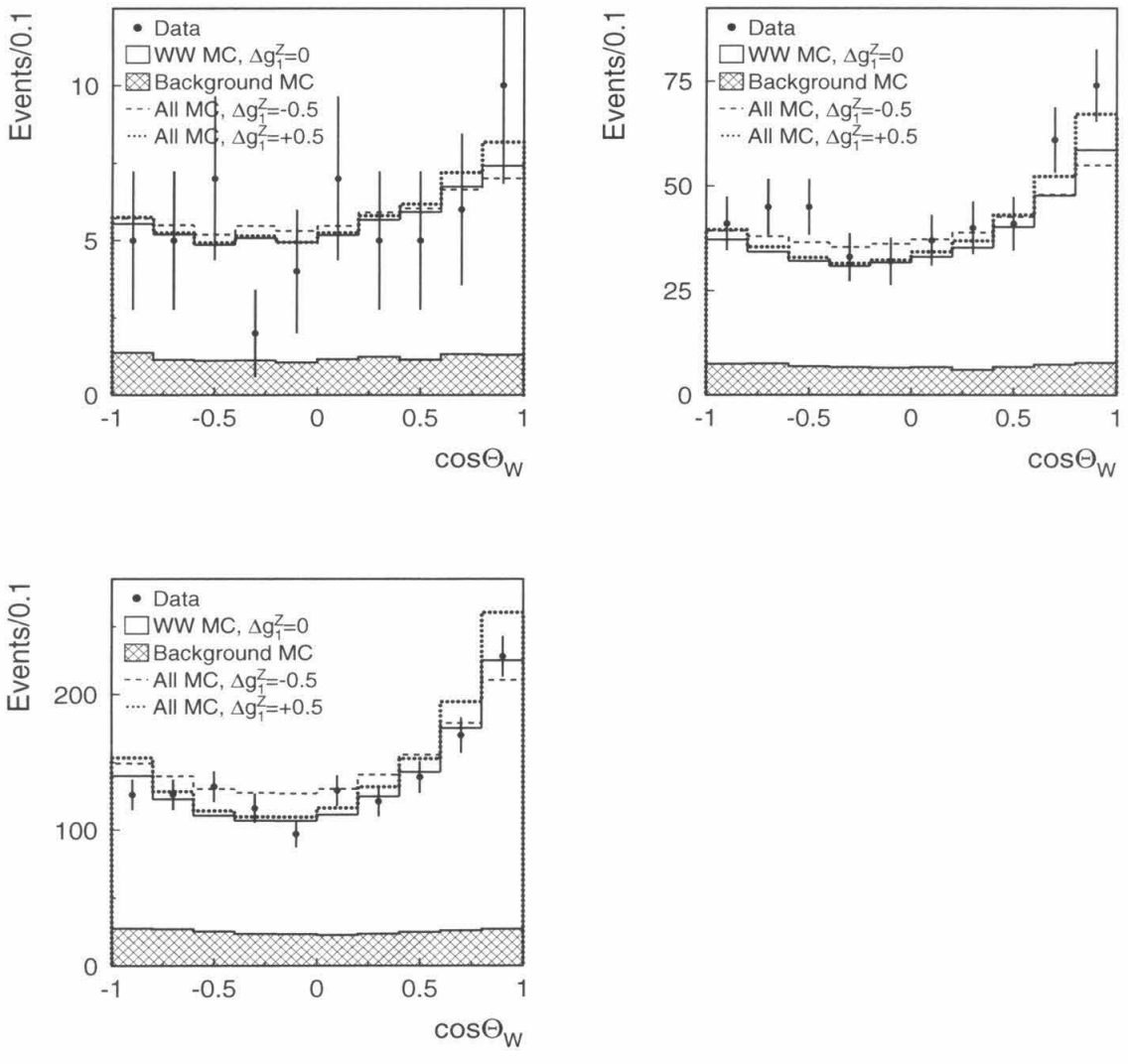

Figure 6.4: Reconstructed $\cos\Theta_W$ distributions for events selected in the 96B, 97 and 98 data sets and the corresponding Monte Carlo predictions. Effects of a non-zero anomalous coupling Δg_1^Z are also shown.

The fit procedure described above was applied to the samples of $W^+W^- \rightarrow q\bar{q}q\bar{q}$ candidates selected in the 96B, 97 and 98 L3 data sets, described in Table 5.1. The reconstructed $\cos\Theta_W$ distributions for the events selected at different energies are shown in Figure 6.4. The results of the Δg_1^Z, $\Delta\kappa_\gamma$, and λ_γ fits using these distributions

are

$$\Delta g_1^Z = 0.16^{+0.13}_{-0.20} \quad \Delta\kappa_\gamma = 0.26^{+0.24}_{-0.33} \quad \lambda_\gamma = 0.18^{+0.13}_{-0.20} \tag{6.19}$$

As in the case of the M_W fits, the statistical error estimates were obtained by finding parameter ranges in which the logarithm of the likelihood isn't smaller than that at the maximum by more than $\frac{1}{2}$ (see Equation (5.15)). Unlike the M_W fits, the dependence of the maximized likelihood on any coupling is non-Gaussian, due to interplay of the cross section and the $\cos\Theta_W$ distribution contributions. Therefore, the errors obtained in this way don't necessarily correspond to a coverage of 68% but nevertheless they can be used to indicate the statistical uncertainty of the measurement.

The results of the anomalous couplings fits are in good agreement with the Standard Model expectations. The observed statistical errors are compatible with MC expectations for event samples of the size observed in the data.

It turns out to be difficult to separate effects due to changes of various gauge couplings, and therefore the analysis of results of simultaneous fits of several anomalous couplings is technically complicated because of large correlations between different measured couplings. Dedicated analyses [118, 119] have shown that the agreement with the Standard Model holds also in the full multidimensional space of anomalous couplings.

6.4 Analysis Uncertainties

To evaluate the systematic uncertainties of my measurements, I rely on the methods used for the M_W fit, described in Section 5.6.

To estimate the errors, I perform the fits on large Monte Carlo samples generated with modified model parameters or different MC models, using the unchanged baseline MC sample.

The systematic errors were reevaluated for each set of data and Monte Carlo used in my analysis, and were found to be consistent with each other and independent of

energy. I assign the error estimates obtained for the 189 GeV data samples, to the combination of the fits of all data samples considered.

Throughout this section I quote estimates of systematic errors for the Δg_1^Z measurement, with the ones for $\Delta\kappa_\gamma$ and λ_γ given in the summary.

6.4.1 Modeling of the Detector Response

Corrections of the jet energy scale and resolutions led to a Δg_1^Z shift of 0.01. Neglecting data-MC subdetector calibration differences changed the measured Δg_1^Z by 0.02. The latter was chosen as a conservative estimate of the effect of possible detector miscalibration on the measurements.

Changes of fitted Δg_1^Z due to θ and ϕ corrections, and smearing of directions of reconstructed jets, amount to 0.01, added in quadrature.

6.4.2 Modeling of the W^+W^- Signal Properties

The uncertainties of the Monte Carlo models of W^+W^- production which affected the cross section measurement, also were considered from the point of view of the measurement of the W mass.

- Reweighting the Monte Carlo W^+W^- events with the ratio of the full and CC03 matrix elements was used to evaluate the effect of the CC03 approximation. The reweighting leads to shifts of less than 0.005 for all the fitted couplings.

- Initial state radiation changes the W^+W^- cross section by a few percent and introduces an additional fluctuation of the W^- flight direction of the order of 1°. The uncertainty of the simulation of these effects is much smaller than the (already small) effects themselves. The precision of the QED calculations implemented in the Monte Carlo codes I used [25] allows me to neglect this source of uncertainty.

- Emission of hard gluons by the final state quarks affects both the success rate of the jet combination algorithm, which is significantly lower for the five-or-more

jet events, and the W flight direction resolution.

To evaluate possible systematic error due to mismodeling of multijet events, I repeat the fits rejecting different fractions, up to 12%, of the data events with highest values of y_{45}. This changes the fit result by up to 0.04±0.04 which I take as an estimate of the error.

- To evaluate the systematic error due to modeling of hadronization, I repeated the fits using a HERWIG Monte Carlo sample as data and the default Monte Carlo sample with JETSET/LUND fragmentation as the baseline MC. I assign the Δg_1^Z bias found, 0.09±0.04, as the systematic error due to modeling of fragmentation.

  Similarly, the 0.01±0.04 bias observed when fitting a MC sample generated without simulating Bose-Einstein correlations with the default one, was taken as an estimate of the corresponding systematic error.

  The biases found for several color reconnection models varied in the 0.01–0.04 range, with a statistical uncertainty of approximately 0.02. I take the shift observed for the Sjöstrand-Khoze I model, 0.02, as an estimate of the error due to modeling of color reconnection.

- An additional uncertainty in the measurement is due to the use of the total event rate in the fit. The accuracy of the theoretical prediction of the W^+W^- cross section is approximately 1%. This introduces an uncertainty in relating the measured W^+W^- cross section to the triple gauge boson couplings. To evaluate this error, I repeated the fits changing the W^+W^- cross section by 1% to obtain a shift of the fitted Δg_1^Z of 0.03.

6.4.3 Modeling of the Backgrounds

- Increasing the accepted $q\bar{q}$ cross section by 5%, which is a realistic estimate of the uncertainty in the background from this source, leads to a change in the fitted Δg_1^Z of 0.02.

- Repeating the fit while changing preselection cuts, which is equivalent to changing the fraction of background events in the fitted sample, led to small, less than 0.01, shifts in Δg_1^Z. I take the quadratic sum of these shifts as an estimate of the systematic error due to possible mismodeling of the $q\bar{q}$ background.

- Z^0Z^0 events are the only other non-negligible background in the event sample used for the measurements. I obtain negligible, less than 0.002, shifts when changing their accepted rate by $\pm 5\%$.

6.4.4 MC Statistics

To evaluate the systematic error due to the finite number of Monte Carlo events, I rely on the procedure used for the M_W measurement. I split my Monte Carlo event samples into several parts and repeat the fits of real data with these subsets. The spread of the results gives an estimated systematic error of 0.02.

6.4.5 Other Checks

The results of the fits were found to be stable with respect to changes of the bin size and changes of the sample used for the measurement, controlled by the neural network output cut. No additional systematic errors were assigned as a result of these checks.

6.4.6 Summary of the Systematic Uncertainties

The systematic errors of the triple gauge boson couplings measurements are summarized in Table 6.2.

As was the case for the W mass measurements, uncertainties of detector response and background modeling lead to small systematic errors due to good understanding of the detector behavior achieved with large amounts of $q\bar{q}$ data and high purity of the selected event samples. The uncertainty of the total W^+W^- cross section also leads to a small error, as the fit results are determined mostly by the reconstructed W^-

Source of uncertainty	Δg_1^Z error	$\Delta\kappa_\gamma$ error	λ_γ error
Jet energy measurement	0.02	0.04	0.02
Jet direction measurement	0.01	0.01	0.01
W^+W^- cross section	0.03	0.05	0.03
CC03 approximation	0	0	0
FSR modeling	0.04	0.07	0.04
Fragmentation	0.09	0.12	0.08
Modeling of BE correlations	0.01	0.02	0.01
Modeling of color reconnection	0.02	0.01	0.03
$q\bar{q}$ background	0.02	0.03	0.02
Z^0Z^0 background	0	0	0
MC statistics	0.02	0.04	0.02
Total	0.11	0.16	0.11

Table 6.2: Systematic errors of the triple gauge boson couplings measurements itemized by the source of the uncertainty. The quadratic sum of all contributions is also given.

angular distribution rather than the accepted event rate. The dominant systematic errors in the determination of the gauge couplings come from uncertainties in the simulation of hadronization of $W^+W^- \rightarrow q\bar{q}q\bar{q}$ events.

The statistical errors are dominant for all the measurements.

6.5 Summary of the Results

This section summarizes the results of my analysis of the distributions of the W flight direction $\cos\Theta_W$ reconstructed with four-jet $W^+W^- \rightarrow q\bar{q}q\bar{q}$ events.

I choose the Δg_1^Z, $\Delta\kappa_\gamma$, λ_γ parameter set to quantify possible deviations of the triple gauge boson couplings from their Standard Model values.

I measured the anomalous couplings to be

$$\Delta g_1^Z = 0.16^{+0.13}_{-0.20}(stat.) \pm 0.11(syst.) \quad (6.20)$$

$$\Delta\kappa_\gamma = 0.26^{+0.24}_{-0.33}(stat.) \pm 0.16(syst.) \quad (6.21)$$

$$\lambda_\gamma = 0.18^{+0.13}_{-0.20}(stat.) \pm 0.11(syst.). \quad (6.22)$$

The results are in agreement with the Standard Model expectation of vanishing anomalous couplings. Both the total event rate and the shape of the $\cos\Theta_W$ distribution agree with the Monte Carlo predictions. The results are in agreement with and complementary to L3 measurements using semileptonic W^+W^- and "single W," $W \rightarrow e\nu$ events [119, 120, 100].

Chapter 7

Summary and Conclusions

This thesis describes the study of the properties of the W boson I performed using $e^+e^- \rightarrow W^+W^- \rightarrow q\bar{q}q\bar{q}$ events found in the data collected by the L3 experiment in 1996–1998. Approximately 250 pb^{-1} of data collected at center-of-mass energies between 161 and 189 GeV was used in my analysis, resulting in a sample of 1,932 selected events.

The large sample of high purity well-reconstructed events allowed me to study this novel physics process, and to measure a variety of the properties of the W boson with an accuracy unachievable in the past.

The measurements of the W boson parameters have proven to be a sensitive probe of the Standard Model and to provide information about crucial components of the theory, in particular the electroweak symmetry breaking mechanism and the non-Abelian triple gauge boson interactions.

7.1 Summary of Results

I developed a neural network discriminator to distinguish $W^+W^- \rightarrow q\bar{q}q\bar{q}$ events from events from various background sources and used it to measure the $e^+e^- \rightarrow W^+W^- \rightarrow$

$q\bar{q}q\bar{q}$ cross section in a wide energy range,

$$\sigma(e^+e^- \to W^+W^- \to q\bar{q}q\bar{q}) = \begin{cases} 0.85^{+0.43}_{-0.34}(stat.) \pm 0.07(syst.) \text{ pb}, & \sqrt{s} = 161.34 \text{ GeV} \\ 5.32^{+0.90}_{-0.83}(stat.) \pm 0.15(syst.) \text{ pb}, & \sqrt{s} = 172.13 \text{ GeV} \\ 8.30^{+0.47}_{-0.46}(stat.) \pm 0.20(syst.) \text{ pb}, & \sqrt{s} = 182.68 \text{ GeV} \\ 7.53^{+0.26}_{-0.25}(stat.) \pm 0.18(syst.) \text{ pb}, & \sqrt{s} = 188.64 \text{ GeV} \end{cases} . \tag{7.1}$$

I combined my measurements with those using other W^+W^- decay channels to arrive at measurements of the total W^+W^- production cross section at these energies,

$$\sigma(e^+e^- \to W^+W^-) = \begin{cases} 2.68^{+0.98}_{-0.67}(stat.) \pm 0.14(syst.) \text{ pb}, & \sqrt{s} = 161.34 \text{ GeV} \\ 12.04^{+1.38}_{-1.29}(stat.) \pm 0.23(syst.) \text{ pb}, & \sqrt{s} = 172.13 \text{ GeV} \\ 16.45 \pm 0.67(stat.) \pm 0.26(syst.) \text{ pb}, & \sqrt{s} = 182.68 \text{ GeV} \\ 16.28 \pm 0.38(stat.) \pm 0.26(syst.) \text{ pb}, & \sqrt{s} = 188.64 \text{ GeV} \end{cases} , \tag{7.2}$$

and the branching ratios of the W decays

$$\text{BR}(W \to e\nu) = 10.27 \pm 0.44(stat.) \pm 0.17(syst.) \ \% \tag{7.3}$$

$$\text{BR}(W \to \mu\nu) = 10.00 \pm 0.46(stat.) \pm 0.17(syst.) \ \% \tag{7.4}$$

$$\text{BR}(W \to \tau\nu) = 11.16 \pm 0.63(stat.) \pm 0.25(syst.) \ \% \tag{7.5}$$

$$\text{BR}(W \to \ell\nu) = 10.43 \pm 0.23(stat.) \pm 0.13(syst.) \ \% \tag{7.6}$$

$$\text{BR}(W \to q\bar{q}') = 68.72 \pm 0.69(stat.) \pm 0.38(syst.) \ \%. \tag{7.7}$$

The measured values of the $e^+e^- \to W^+W^-$ cross section and W branching ratios are in good agreement with the predictions of the Standard Model. The W^+W^- results, together with measurements of the single W boson production $e^+e^- \to We\nu$, allowed

me to limit the width of non-SM invisible decays of the W

$$\Gamma_{\mathrm{W}}^{invisible} < 17 \text{ MeV} \tag{7.8}$$

at 95% confidence level, and infer the value of the *cs* element of the Cabibbo-Kobayashi-Maskawa matrix

$$|V_{cs}| = 1.033 \pm 0.033(stat.) \pm 0.018(syst.). \tag{7.9}$$

The measurements of the $e^+e^- \rightarrow W^+W^-$ cross sections were not feasible before LEP 2 while the determination of the branching ratios is significantly more precise than previous measurements.

I interpreted the measured value of the $e^+e^- \rightarrow W^+W^-$ cross section at the production threshold $\sqrt{s} = 161.3$ GeV to obtain an estimate of the mass of the W boson

$$\mathrm{M_W} = 80.94^{+0.50}_{-0.48}(stat.) \pm 0.10(syst.) \text{ GeV}. \tag{7.10}$$

I performed also a measurement of the mass and width of the W relying on the direct reconstruction of the invariant masses of dijet systems produced in W boson decays. Distributions of dijet invariant masses were reconstructed for the data collected at energies above the threshold, using kinematic fit and jet combination methods developed for the cross section measurement. A maximum likelihood fit of the distribution, based on Monte Carlo reweighting technique, was used to determine the W mass and width

$$\mathrm{M_W} = 80.60 \pm 0.11(stat.) \pm 0.09(syst.) \text{ GeV} \tag{7.11}$$

$$\Gamma_{\mathrm{W}} = 2.15 \pm 0.28(stat.) \pm 0.14(syst.) \text{ GeV}. \tag{7.12}$$

I combined my threshold and direct reconstruction measurements of $\mathrm{M_W}$ and Γ_{W} with ones performed with semileptonic W^+W^- events recorded by L3, to arrive at

my best estimates of the W mass and width

$$M_W = 80.44 \pm 0.08(stat.) \pm 0.06(syst.) \text{ GeV} \quad (7.13)$$

$$\Gamma_W = 2.18 \pm 0.20(stat.) \pm 0.11(syst.) \text{ GeV}. \quad (7.14)$$

There is agreement between the direct reconstruction and threshold measurements of M_W, and the found values of M_W and Γ_W are consistent with SM predictions. The measurements are competitive with the ones previously obtained by CDF and DØ experiments.

I analyzed the distribution of the flight direction of the W bosons, reconstructed using jet charge estimators, as well as their production cross section, to probe the trilinear couplings of the W boson with the photon and Z^0. I investigated the reduced set of anomalous W boson couplings Δg_1^Z, $\Delta\kappa_\gamma$, and λ_γ, parametrizing possible deviations of the form of the $W^+W^-\gamma/Z^0$ vertex from the one given by the Standard Model. The Monte Carlo reweighting method was applied to the fit of the reconstructed differential cross section. The anomalous gauge couplings of the W boson were found to be

$$\Delta g_1^Z = 0.16^{+0.13}_{-0.20}(stat.) \pm 0.11(syst.) \quad (7.15)$$

$$\Delta\kappa_\gamma = 0.26^{+0.24}_{-0.33}(stat.) \pm 0.16(syst.) \quad (7.16)$$

$$\lambda_\gamma = 0.18^{+0.13}_{-0.20}(stat.) \pm 0.11(syst.). \quad (7.17)$$

Both the measured W^+W^- cross sections and the reconstructed W boson angular distributions are consistent with the Standard Model couplings of the W boson.

The limits on anomalous W couplings are stricter than previously available ones. As my measurements of the couplings are based on data at a constant momentum transfer scale, they don't require any assumptions about the energy dependence of possible anomalies.

The results and analysis methods developed in this thesis were used for six L3 publications [95, 96, 97, 121, 122, 123].

Errors of all the measurements described in this thesis were dominated by the statistical fluctuations due to finite number of the data samples used. Nevertheless the systematic uncertainties of modeling of hadronization of the four-quark system are important, and more work will be necessary to reduce them to the level adequate for the final analysis of the full LEP 2 data samples.

7.2 Combination with Other Results

A large amount of data was collected at LEP since 1998, at collision center-of-mass energies from 192 to 208 GeV. Approximately 350 pb^{-1} of luminosity were delivered to each of the LEP experiments in 1999–2000. Analysis of the data will allow the LEP collaborations to make significant improvements in measurements similar to the ones described in this thesis.

Preliminary studies using these data indicate that $e^+e^- \rightarrow W^+W^-$ cross section is in agreement with the Standard Model predictions up to energies of 208 GeV [124]. Also in agreement with SM expectations are the determined values of the W branching ratios, measured with a 0.1% precision, combining measurements of all LEP experiments. Triple gauge couplings were found to be zero within 0.03-0.07, depending on the coupling.

The preliminary measurements of the W boson mass and width, from the combined LEP 2 data, are

$$M_W = 80.427 \pm 0.046 \text{ GeV} \quad (7.18)$$

$$\Gamma_W = 2.12 \pm 0.11 \text{ GeV}. \quad (7.19)$$

With the increased precision, no difference is observed between the values of M_W measured with hadronic and semileptonic W^+W^- events,

$$M_W^{q\bar{q}q\bar{q}} - M_W^{q\bar{q}\ell\nu} = 5 \pm 51 \text{ MeV}, \quad (7.20)$$

which indicates that hadronization effects probably lead to small biases of measured M_W.

Progress is also being made on the theoretical side [125]. A new generation of MC models has been developed, that will lead to a more precise theoretical description of W^+W^- production. Accuracy of the calculated $e^+e^- \rightarrow W^+W^-$ cross section better than 0.5% seems within their reach.

Comparison of the measurement of the W mass with indirect predictions based on other precision electroweak data allows one to check the consistency of the Standard Model, and estimate the mass of the Higgs boson assuming the validity of the Standard Model. The relatively high value of the W mass I measured indicates a light Higgs boson, with a mass close to the lower limit allowed by direct searches at LEP (currently 113 GeV [126]). This conclusion holds with the analysis of all the data collected at LEP so far.

Figures 7.1 and 7.2 show the results of the fits done by the LEP Electroweak Working Group of a number of electroweak measurements including the L3 measurements of M_W. The directly measured values of the W boson and top quark masses were found to be in agreement with the ones predicted by the Standard Model given other electroweak measurements. Joint analysis of all electroweak data currently available produces an estimate of the Higgs boson mass

$$M_H \; < \; 170 \text{ GeV} \;\; \text{at } 95\% \text{ C.L.}, \tag{7.21}$$

that is especially promising from the point of view of the Large Hadron Collider program which will undertake extensive searches for the Higgs boson. Such a small mass of the Higgs boson would mean that the next generation of experiments at the LHC is destined either to find it or discredit it as the mechanism of spontaneous $SU(2)\times U(1)$ symmetry breaking, and possibly to discover an alternative mechanism.

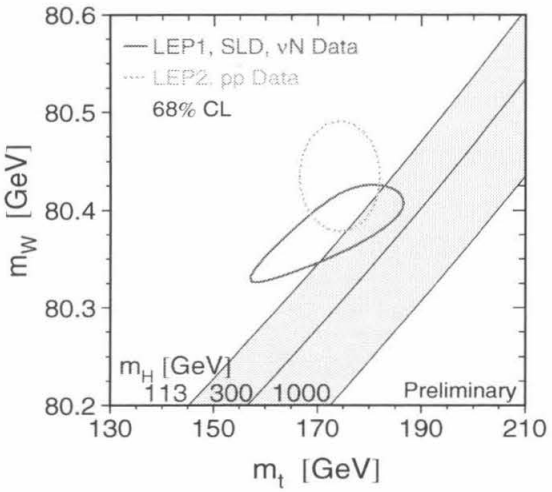

Figure 7.1: The comparison of the direct measurements of M_W, M_t with the values inferred from other precision electroweak measurements. The band shows the Standard Model prediction of the M_W (M_t) dependence for various values of the Higgs boson mass.

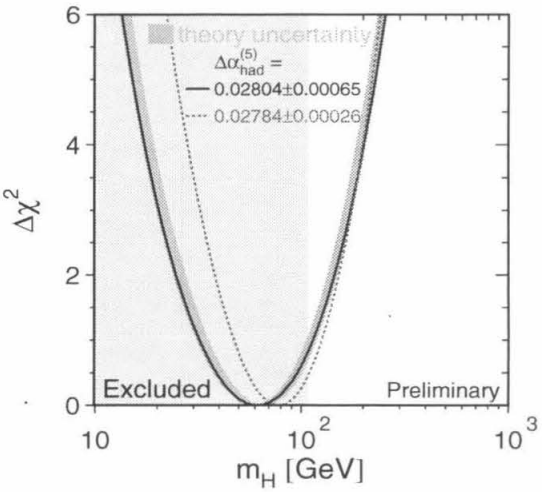

Figure 7.2: The χ^2 of the LEP Electroweak Working Group fit as a function of the Higgs boson mass. Also shown are the lower bound on M_H given by direct searches and some systematic uncertainties of the indirect determination of M_H.

7.3 Conclusions

Within the accuracy of my measurements, no deviations from Standard Model expectations were observed and no new physics were necessary to explain any features of the data I studied.

Yet again the Standard Model was able to pass all the tests it was confronted with. It did so in a new setting of $e^+e^- \to W^+W^-$ annihilation, and in ever more precise and direct measurements of its fundamental parameters.

While the Standard Model is perceived to be incomplete from the theoretical point of view, and is likely to be replaced with a more basic theory eventually, for now it remains a task and a challenge to physicists to perform an experiment whose outcome will *not* be predicted by the Standard Model.

Physicists should take heart in the fact that the study of the mechanism of the electroweak symmetry breaking, with all the surprises it might lead to, is likely to be

within the reach of the next generation of high energy physics experiments.

References

[1] H. Becquerel, Comptes rendus de l'Academie des Sciences **122** (1896) 420, ibid. **122** (1896) 501, ibid. **122** (1896) 689, ibid. **122** (1896) 1086.

[2] E. Rutherford, The London, Edinburgh, and Dublin Philosophical Magazine and Journal of Science **47** (1899) 109;
H. Becquerel, Comptes rendus **130** (1900) 1584, ibid. **131** (1900) 137.

[3] W. Pauli, Open Letter to Radioactive Persons, 1930.

[4] J. Chadwick, Nature **129** (1932) 312.

[5] E. Fermi, Z. Phys. **88** (1934) 161.

[6] T.D. Lee and C.N. Yang, Phys. Rev. **104** (1956) 254.

[7] C.S. Wu *et al.*, Phys. Rev. **105** (1957) 1413.

[8] S.S. Gerstein and Y.B. Zeldovich, Zh. Eksp. Teor. Fiz. **29** (1955) 698;
R.P. Feynman and M. Gell-Mann, Phys. Rev. **109** (1958) 193;
E.C.G. Sudarshan and R.E. Marshak, ibid. **109** (1958) 1860;
J.J. Sakurai, Nuovo Cim. **7** (1958) 649.

[9] H. Yukawa, Proc. Phys. Math. Soc. Jpn. **17** (1935) 48.

[10] O. Klein, in Les Nouvelles Théories de la Physique, Institut International de Coopération Intellectuelle, Paris, 1938, 6.

[11] S.L. Glashow, Nucl. Phys. **22** (1961) 579, S. Weinberg, Phys. Rev. Lett. **19** (1967) 1264, A. Salam, in Elementary particle theory, ed. N. Svartholm, Almquist and Wiksell, Stockholm, 1968, 367.

[12] C.N. Yang and R.L. Mills, Phys. Rev. **96** (1954) 191.

[13] P.W. Higgs, Phys. Lett. **12** (1964), Phys. Rev. Lett. **13** (1964) 508, Phys. Rev. **145** (1966) 1156.

[14] C. Quigg, Gauge Theories of the Strong, Weak, and Electromagnetic Interactions, The Benjamin/Cummings Publishing Company, Inc., Reading, Massachusetts, 1983.

[15] G. 't Hooft, Nucl. Phys. **B 33** (1971) 173, ibid. **B 35** (1971) 167.

[16] M. Grünewald, Physics Reports **322** (1999) 125.

[17] C. H. Llewellyn Smith and J.A. Wheater, Phys. Lett. **B 105** (1981) 486.

[18] The UA1 Collaboration, G. Arnison *et al.*, Phys. Lett. **B 122** (1983) 103.

[19] The UA1 Collaboration, G. Arnison *et al.*, Phys. Lett. **B 126** (1983) 398.

[20] J. Ellison, W and Z Properties at the Tevatron, hep-ex/9910037, 1999.

[21] A.D. Rujula, M.B. Gavela, P. Hernandez, and E.Masso, Nucl. Phys. **B 384** (1992) 3.

[22] K. Hagiwara, K. Hikasa, R.D. Peccei, D. Zeppenfeld, Nucl. Phys. **B 282** (1987) 253.

[23] Particle Data Group, C. Caso *et al.*, European Phys. Jour. **C 3** (1998) 1.

[24] T. Muta, R. Najima, and S. Wakaizumi, Mod. Phys. Lett **A 1** (1986) 203.

[25] D. Bardin, A. Olshevskii, M. Bilenkii, and T. Riemann, Phys. Lett. **B 308** (1993) 403, ibid. **B 357** (1995) 725.

[26] V.S. Fadin, V.A. Khoze, and A.D. Martin, Phys. Lett. **B 311** (1993) 311.

[27] D.Yu. Bardin, W. Beenakker, and A. Denner, Phys. Lett. **B 317** (1993) 213.

[28] F.A. Berends, R. Kleiss, and R. Pittau, Nucl. Phys. **B 424** (1994) 308.

[29] W. Beenakker *et al.*, WW Cross-Sections and Distributions, in Proceedings of Workshop on Physics at LEP2, vol. 1, eds. G. Altarelli, T. Sjöstrand, and F. Zwirner, CERN-96-01 (1996) 79, CERN, Geneva.

[30] N. Cabibbo and R. Gatto, Phys. Rev. **124** (1961) 1577.

[31] Y.S. Tsai and A.C. Hearn, Phys. Rev. **140** (1965) B721.

[32] O.P. Sushkov, V.V. Flambaum, and I.B. Khriplovich, Yad. Fiz. **20** (1974) 1016.

[33] W. Alles, C. Boyer, and A.J. Buras, Nucl. Phys. **B 119** (1977) 125.

[34] C. H. Llewellyn Smith, Phys. Lett. **B 46** (1973) 233.

[35] T. van Ritbergen and R.G. Stuart, On the Precise Determination of the Fermi Coupling Constant from the Muon Lifetime, hep-ph/9904240.

[36] M. Bohm, H. Spiesberger, and W. Hollik, Fortschr. Phys. **34** (1986) 687; W.F.L. Hollik, ibid. **38** (1990) 165.

[37] P. Chankowski *et al.*, Nucl. Phys. **B 405** (1994) 101.

[38] A. Arhrib, J.L. Kneur, and G. Moultaka, Phys. Rev. **B 334** (1994) 378.

[39] T. Inami, C.S. Lim, B. Takeuchi, and M. Tanabashi, Phys. Lett. **B 381** (1996) 458.

[40] J.-M. Frère, M. Tytgat, J.M. Moreno, J. Orloff, Nucl. Phys. **B 429** (1994) 3.

[41] E. Witten, Nucl. Phys. **B 188** (1981) 513.

[42] N. Arkani-Hamed, S. Dimopoulos, and G. Dvali, Phys. Lett. **B 429** (1998) 263.

[43] C. Balázs *et al.*, Phys. Rev. Lett. **83** (1999) 2112.

[44] J. Kalinowski, Supersymmetric W Boson Decays as a Means to Search for Charginos and Neutralinos, hep-ph/9703431, 1997.

[45] J. Kalinkowski and P. Zerwas, Decays of W Bosons to Charginos and Neutralinos, hep-ph/9702386.

[46] LEP Design Report, Vol.I, The LEP Injector Chain, Preprint CERN–LEP/TH/83–29, CERN, 1983.

[47] LEP Design Report, Vol.II, The LEP Main Ring, Preprint CERN–LEP/TH/84–01, CERN, 1984.

[48] L3 Collaboration, O. Adriani *et al.*, Phys. Rep. **236** (1993) 1.

[49] L. Arnaudon *et al.*, Phys. Lett. **B 284** (1992) 431.

[50] A.A. Sokolov and I.M. Ternov, Dokl. Akad. Nauk. SSSR **153** (1963) 1052.

[51] The LEP Energy Working Group, R. Assmann *et al.*, Eur. Phys. J. **C 6** (1999) 187.

[52] The LEP Energy Working Group, A. Blondel *et al.*, Eur. Phys. J. **C 11** (1999) 573.

[53] B. Dehning, The LEP Spectrometer, in Proceedings of 9th LEP-SPS Performance Workshop, Chamonix, France, ed. J. Poole, CERN-SL-99-007-DI (1999) 241.

[54] The L3 Collaboration, B. Adeva *et al.*, Nucl. Inst. Meth. **A 289** (1990) 35.

[55] B. Alpat *et al.*, Nucl. Inst. Meth. **A 315** (1992) 197.

[56] J. Wenninger, Mesure de paramètres électro-faibles du Z avec la réaction $e^+e^- \rightarrow e^+e^-(\gamma)$, Ph.D. thesis, University of Geneva, 1992.

[57] D. Kirkby, A Study of Final State Radiation in Hadronic Z Decays, Ph.D. thesis, California Institute of Technology, 1995.

[58] O. Adriani *et al.*, Nucl. Inst. Meth. **A 302** (1991) 53.

[59] I. C. Brock *et al.*, Nucl. Inst. Meth. **A 381** (1996) 236.

[60] The L3 detector simulation is based on GEANT Version 3.15. R. Brun *et al.*, GEANT 3, CERN-DD/EE/84-1 (Revised), 1987.

[61] A. Kunin *et al.*, G-Factors, Preprint L3 Note 1840, L3, 1995.

[62] T. Sjöstrand, Comp. Phys. Comm. **82** (1994) 74.

[63] The L3 Collaboration, M. Acciarri *et al.*, Z. Phys. **C 55** (1992) 39.

[64] S. Banerjee and S. Banerjee, Tuning of QCD model parameters using LEP data of hadronic Z decays, L3 Note 1978, July 1996.

[65] D. Bardin *et al.*, Comp. Phys. Comm. **104** (1997) 161.

[66] The L3 Collaboration, M. Acciarri *et al.*, Phys. Lett. **B 465** (1999) 363.

[67] R. Engel, Z. Phys. **C 66** (1995) 203; R. Engel and J. Ranft, Phys. Rev. **D 54** (1996) 4244.

[68] A. Capella *et al.*, Phys. Rev. **236** (1994) 227.

[69] M. Skrzypek, S. Jadach, W. Placzek, and Z. Wąs, Comp. Phys. Comm. **94** (1996) 216; M. Skrzypek, S. Jadach, M. Martinez, W. Placzek, and Z. Wąs, Phys. Lett. **B 372** (1996) 289.

[70] D. Bardin *et al.*, Event Generators for WW Physics, in Proceedings of Workshop on Physics at LEP2, vol. 2, eds. G. Altarelli, T. Sjöstrand, and F. Zwirner, CERN-96-01 (1996) 3, CERN, Geneva.

[71] D.R. Yennie, S. Frautschi, and H. Suura, Ann. Phys. NY **13** (1961) 379.

[72] V. Fadin, V. Khoze, A. Martin, and W. Stirling, Phys. Lett. **B 363** (1995) 112.

[73] L. Lönnblad and T. Sjöstrand, Eur. Phys. J. **C 2** (1998) 165.

[74] F.A. Berends, R. Kleiss, and R. Pittau, Nucl. Phys. **B 424** (1994) 308; Nucl. Phys. **B 426** (1994) 344; Nucl. Phys. (Proc. Suppl.) **B 37** (1994) 163;

R. Kleiss and R. Pittau, Comp. Phys. Comm. **83** (1994) 141;
R. Pittau, Phys. Lett. **B 335** (1994) 490.

[75] S. Catani *et al.*, Phys. Lett. **B 269** (1991) 432;
S. Bethke *et al.*, Nucl. Phys. **B 370** (1992) 310.

[76] T. Sjöstrand, Comp. Phys. Comm. **28** (1983) 227.

[77] Yu. Dokshitzer, G. Leder, S. Moretti, and B. Webber, JHEP **8** (1997) 1.

[78] M. Grünewald, Selection of Hadronic W-Pair Events with L3 and Determination of the W-Boson Mass, L3 Note 1908, January 1996.

[79] F. James, CERN Program Library Long Writeup D506 MINUIT, CERN, 1993.

[80] C. Peterson *et al.*, Comp. Phys. Comm. **81** (1994) 185.

[81] R. Barlow and C. Beeston, Comp. Phys. Comm. **77** (1993) 219.

[82] F. Le Diberder, Mark II/SLC Note 245, SLAC, 1989.

[83] Ljubiša Drndarski, Minimal Spanning Tree Based Approach to W^+W^- Events Selection, Master's thesis, University of Nijmegen, The Netherlands, 1999.

[84] The L3 Collaboration, M. Acciarri *et al.*, Z. Phys. **C 62** (1994) 551.

[85] G. Marchesini *et al.*, Comp. Phys. Comm. **67** (1992) 465.

[86] G. Goldhaber *et al.*, Phys. Rev. **120** (1960) 300.

[87] S. Haywood, Where Are We Going With Bose-Einstein - a Mini-Review, RAL Note 94-074, July 1994.

[88] R.Hanbury Brown and R.Q. Twiss, Philos. Mag. Ser. 7 **45** (1954) 663.

[89] G. Gustafson, U. Pettersson, and P. Zerwas, Phys. Lett. **B 209** (1988) 90.

[90] T. Sjöstrand and V. Khoze, Z. Phys. **C 62** (1994) 281.

[91] T. Sjöstrand and V. Khoze, Eur. Phys. J. **C 6** (1999) 271.

[92] G. Gustafson and J. Häkkinen, Z. Phys. **C 64** (1994) 659.

[93] D. Duchesneau, Energy and Particle Flow Studies in $e^+e^- \to W^+W^- \to q\bar{q}q\bar{q}$ to Search for Colour Reconnection Effects, L3 Note 2486, December 1999.

[94] L. Lönnblad, Comp. Phys. Comm. **71** (1992) 15.

[95] The L3 Collaboration, M. Acciarri *et al.*, Phys. Lett. **B 398** (1997) 223.

[96] The L3 Collaboration, M. Acciarri *et al.*, Phys. Lett. **B 407** (1997) 419.

[97] The L3 Collaboration, M. Acciarri *et al.*, Phys. Lett. **B 436** (1998) 437.

[98] The W-Physics Analysis Group of the L3 Collaboration, Preliminary Results on the Measurement of W-Pair Cross Sections in e^+e^- Interactions at $\sqrt{s}$ = 189 GeV and W-Decay Branching Fractions, L3 Note 2376, March 1999.

[99] D. Bardin, S. Riemann, and T. Riemann, Z. Phys. **C 32** (1986) 121.

[100] The L3 Collaboration, M. Acciarri *et al.*, Phys. Lett. **B 403** (1997) 168; A. Kunin, G. Sultanov, and S. Schmidt-Kaerst, Preliminary Results on Single W Boson Production at $\sqrt{s}$ = 189 GeV, L3 Note 2367, March 1999.

[101] Z. Kunszt *et al.*, Determination of the Mass of the W Boson, in Proceedings of Workshop on Physics at LEP2, vol. 1, eds. G. Altarelli, T. Sjöstrand, and F. Zwirner, CERN-96-01 (1996) 141, CERN, Geneva.

[102] N.V. Batalova and A.V. Shvorob, Measurement of W Boson Mass with Lepton Energy Spectra in $W \to l\nu$ Decays, L3 Note 2482, November 1999.

[103] ALEPH Collaboration, R. Barate *et al.*, Phys. Lett. **B 422** (1998) 384.

[104] D.M. Schmidt, R.J. Morrison, and M.S. Witherell, Nucl. Instr. and Meth. **A 328** (1993) 547.

[105] The W-Physics Analysis Group of the L3 Collaboration,
Preliminary Results on the Measurement of Mass and Width of the W Boson at LEP, L3 Note 2377, March 1999.

[106] The ALEPH Collaboration, R. Barate *et al.*, Phys. Lett. **B 453** (1999) 121.

[107] The DELPHI Collaboration, P. Abreu *et al.*, Phys. Lett. **B 462** (1999) 410.

[108] The OPAL Collaboration, G. Abbiendi *et al.*, Phys. Lett. **B 453** (1999) 138.

[109] The CDF Collaboration, F. Abe *et al.*, Phys. Rev. Lett. **75** (1995) 11.

[110] The DØ Collaboration, B. Abbott *et al.*, Phys. Rev. Lett. **84** (2000) 222.

[111] The DØ Collaboration, B. Abbott *et al.*, Phys. Rev. Lett. **80** (1998) 3008.

[112] LEP Electroweak Working Group, A Combination of Preliminary Electroweak Measurements and Constraints on the Standard Model, Preprint CERN-EP-2000-016, CERN, 2000.

[113] K. Gaemers and G. Gounaris, Z. Phys. **C 1** (1979) 259.

[114] J. Maalampi, D. Schildknecht, and K.H. Schwarzer, Phys. Lett. **B 166** (1986) 361.

[115] K. Hagiwara, S. Ishihara, R. Szlapski, and D. Zeppenfeld, Phys. Lett. **B 283** (1992) 353.

[116] R.D. Field and R.P. Feynman, Nucl. Phys. **B 136** (1978) 1.

[117] Silke Duensing, Measurement of Gauge Boson Couplings in Hadronic W Pair Events at LEP II, Master's thesis, Humboldt-Universität zu Berlin, Germany, 1998.

[118] Peter Molnár, A Measurement of the Self-Couplings of Electroweak Bosons, Ph.D. thesis, Humboldt-Universität zu Berlin, Germany, 1999.

[119] Stefano Villa, Measurement of the Triple Gauge Boson Couplings of the W Boson at LEP2, Ph.D. thesis, Northeastern University, Boston, 2000.

[120] The W-Physics Analysis Group of the L3 Collaboration,
Preliminary Results on the Measurement of Triple-Gauge-Boson Couplings of the W Boson at LEP, L3 Note 2378, March 1999.

[121] The L3 Collaboration, M. Acciarri *et al.*, Phys. Lett. **B 413** (1997) 176.

[122] The L3 Collaboration, M. Acciarri *et al.*, Phys. Lett. **B 454** (1999) 386.

[123] The L3 Collaboration, M. Acciarri *et al.*, Phys. Lett. **B 467** (1999) 171.

[124] A. Gurtu, Precision Tests of the Electroweak Gauge Theory, ICHEP 2000, Osaka (2000).

[125] G. Passarino, Recent Theoretical Developments in LEP 2 Physics, ICHEP 2000, Osaka (2000).

[126] P. Igo-Kemenes, Search for New Particles and New Phenomena: Results from e^+e^- Colliders, ICHEP 2000, Osaka (2000).